THERMALLY DRIVEN ENERGY CONVERSION AND STORAGE BASED ON ORGANIC NANOCOMPOSITES

A Dissertation

by

SUK LAE KIM

Submitted to the Office of Graduate and Professional Studies of
Texas A&M University
in partial fulfillment of the requirements for the degree of

DOCTOR OF PHILOSOPHY

Chair of Committee,	Choongho Yu
Committee Members,	Ying Li
	Jonathan Felts
	Shiren Wang
Head of Department,	Andreas A. Polycarpou

May 2017

Major Subject: Mechanical Engineering

ABSTRACT

Thermoelectric (TE) energy conversion is very effective in capturing low-grade waste heat to supply electricity particularly to small devices such as sensors, wireless communication units, and wearable electronics. Conventional inorganic thermoelectric materials, however, are often inadequately brittle, expensive, toxic, and heavy. I have developed both p- and n-type fabric-like flexible light-weight materials by functionalizing the carbon nanotube (CNT) mats. The poor thermopower and only p-type characteristics of typical CNTs have been converted into both p- and n-type with high thermopower. With the optimized device design to maximally utilize temperature gradients, an electrochromic glucose sensor was successfully operated without batteries or external power supplies, demonstrating self-powering capability.

In addition to the development of high performance organic thermoelectric devices, I studied a novel method of simultaneously generating a large voltage from a temperature gradient and storing electrical energy by utilizing thermally-driven ion diffusion (Soret effect) mechanism. I have observed extremely high output voltage (8 mV/K) in an ionic conducting film, polystyrene sulfonic acid (PSSH), which was utilized as a driving force of electrochemical reactions in electrodes, resulting in a charging behavior without an external power supply. With a small temperature difference (5 K) possibly created over wearable energy harvesting devices, the thermally chargeable supercapacitor (TCSC) produced 38 mV with a large areal capacitance (1200 F/m^2).

DEDICATION

This dissertation is dedicated to my beloved and supportive wife, Ji Youn Jeong, and my adorable son, Danny, for their endless encouragement, unconditional trust, and true love.

ACKNOWLEDGEMENTS

First, I would like to sincerely thank my supervisor, Dr. Choongho Yu, for his patient guidance, support, advice and inspiration to my research throughout my Ph.D. course. Dr. Yu's enthusiasm and commitment to the research is what I need to carry on in my future career. I also truly appreciate the help and suggestions from my committee members, Dr. Jonathan Felts, Dr. Ying Li, and Dr. Shiren Wang.

Also, I appreciate the members of Nano Energy Lab for their friendship and support.

I would like to present my deep gratitude to my family, for their numerous supports and sacrifices. Finally, I sincerely thank my wife, Ji Youn, and my son, Danny, who always stand by me in joy and sorrow. Words cannot express how grateful I am for the love and trust they have shown me.

CONTRIBUTORS AND FUNDING SOURCES

Contributors

This work was supervised by a dissertation committee consisting of Professor Choongho Yu, Professor Ying Li, and Professor Jonathan Felts of the Department of Mechanical Engineering and Professor Shiren Wang of the Department of Industrial & Systems Engineering.

The characterizations depicted in Chapter 3 were conducted in part by Kyungwho Choi and Abdullah Tazebay of the Department of Mechanical Engineering and were published in 2014. The material synthesis in Chapter 4 was conducted in part by Henry Lin of the Department of Materials Science & Engineering and was published in 2016.

All other work conducted for the dissertation was completed by the student, under the advisement of Professor Choongho Yu of the Department of Mechanical Engineering.

Funding Sources

This work was made possible by the financial support from the U.S. Air Force Office of Scientific Research (Grant No. FA9550-13-1-0085) under the auspices of Dr. Charles Lee, the Pioneer Research Center Program through the National Research Foundation of Korea (Grant No. 2011-0001645) funded by the Ministry of Education,

Science and Technology, and the U.S. National Science Foundation (Grant No. CMMI 1030958).

TABLE OF CONTENTS

LIST OF FIGURES

LIST OF TABLES

CHAPTER I

INTRODUCTION

1.1 Background

In recent years, exploring renewable and sustainable energy sources is becoming very important in our society to solve the environmental problems caused by traditional fossil-based fuels. Among various energy sources, thermal energy would be one of the strongest candidates as a new clean energy source due to its abundance. It would be easy to find heat energy, especially waste heat, from everywhere. For example, there are 85% of heat is dissipated from compressed air system. Also, solar panel for photovoltaic energy generation system dissipated heat in various forms. Even humans are always dissipating heat from their bodies. If we efficiently capture the wasted heat and convert heat energy into useful energy, it will be greatly helpful for solving energy and environmental problems.

Therefore, developing an efficient energy harvesting system capturing low-grade waste heat is projected to be one of the most sustainable, clean, and promising energy technologies. Especially, rapid development of wearable and flexible electronics prompted researchers to be interested in energy harvesting and conversion of dissipated heat from human body or other electronic devices. Typically, thermal energy harvesting system directly converts temperature gradient (heat energy) into electric voltage by utilizing (1) Seebeck effect, (2) temperature dependence of electrochemical redox potentials, and (3) Soret effect.

Conventional thermoelectric materials utilize the Seebeck effect to convert thermal energy into electricity. When there is a temperature gradient along the materials, electrons in n-type and holes in p-type material diffuse from hot side to the cold side. And this diffusion establishes a thermoelectric voltage. For many years, researchers have been putting intense efforts into improving the performance of thermoelectric material due to the great advantages in simplicity, stability and durability, because this device is solid state and operating without any moving parts.

In the past decades, there has been great improvement of thermoelectric performance [1-12]. However, most of commercial thermoelectric device is based on inorganic materials including Bi-Te alloy, which is expensive, toxic, heavy and not easy to fabricate. Therefore, organic thermoelectric materials are attracting great attention due to its advantages such as solution processable, flexible, light, low cost and non-toxic [13-17].

Even though organic thermoelectric device can be an excellent candidate as thermal energy harvestor, there are some limitations for practical applications due to its intrinsically low thermopower (~ 0.3 mV/K). Therefore, recently different mechanisms of thermal energy harvesting such as thermoelectrochemical cell and Soret effect have gained strong interest from research communities owing to their relatively large voltage generation.

Thermoelectrochemical cell utilizes thermally-induced voltage originating from the temperature dependent electrochemical redox potential of electrodes to directly convert heat energy into electricity. Thermoelectrochemical cell is also promising energy

harvesting system because of its advantages of substantially high thermal-to-voltage conversion (~1.4 mV/K), simple structure, and potentially low cost[18-19]. However, most of thermoelectrochemical cells need robust encapsulation to prevent leakage of liquid electrolytes and other package components making them bulky, which are not favorable to wearable and portable applications.

In addition to these effects, the Soret effect establishes a difference in ion concentrations within an electrolyte as a result of ion migration driven by a temperature gradient, creating extremely large thermally induced voltage (~ 10 mV/K) [20-23]. Recently, it has been reported that the Soret effect can be utilized in solid-state electrolyte, which makes it possible to maintain the temperature gradient easily [21-23].

1.2 Objectives and dissertation outline

In this dissertation, I utilized two different thermal energy harvesting mechanisms, Seebeck effect and Soret effect, to develop efficient thermal energy harvesting systems based on carbon-based organic materials such as carbon nanotubes (CNT) and polymers.

In the Seebeck effect part, the main objective is to develop high performance n-type organic thermoelectric materials and also fabricate flexible and lightweight organic thermoelectric devices generating enough power to operate an actual working device.

For the Soret effect, the objective of this work is to efficiently harvest thermal energy with solid-state polymer electrolyte and store this energy electrochemically in electrodes like a supercapacitor. To realize this objective, I have developed a new

concept of energy device which is named as “Thermally chargeable supercapacitor (TCSC)”.

Chapter II provides a brief literature review of organic thermoelectric materials and devices based on the Seebeck effect. The fundamental mechanisms of the Seebeck effect in electronic conductors are first presented, followed by the performance of CNT-based thermoelectric materials that have been dramatically improved over several years. Moreover, research outcomes of n-type characteristics of organic materials are introduced, which has been one of the major limitations to develop organic thermoelectric device which consist of p- and n-type components. The second part of this review covers the basics of the Soret effect in solid-state ionic conductors, with emphasis on the advantages of polymer electrolytes showing extremely high thermally induced voltage.

Chapter III explores the development of both p- and n-type fabric-like flexible light-weight materials by functionalizing the large surfaces and junctions in CNT films. The poor thermopower and only p-type characteristics of typical CNTs have been converted into both p- and n-type with high thermopower by using the novel functionalization methods. The changes in the electronic band diagrams of the CNTs were experimentally investigated by diverse characterization methods, elucidating the carrier type and relatively large thermopower values. Moreover, with the optimized thermoelectric device design to maximally utilize temperature gradients, a bio sensor was successfully operated without batteries or external power supplies, demonstrating self-powering capability.

In Chapter IV, a novel method of simultaneously generating a large voltage from a temperature gradient and storing electrical energy without losing the benefit of solid-state no-moving part devices like conventional thermoelectrics are reported. In this work, we utilized thermally-driven ion diffusion (Soret effect) to greatly increase the output voltage with solid-state polyelectrolyte film, polystyrene sulfonic acid (PSSH). Polyaniline (PANI) coated electrodes containing graphene and carbon nanotube (G/CNT) sandwiched the PSSH film where thermally induced voltage enabled electrochemical reactions, resulting in a charging behavior without an external power supply.

Chapter V investigates a fundamental mechanism of high thermally induced voltage in solid-state polyelectrolyte films. It is hypothesized that solid-state polyelectrolyte will show the higher thermopower than typical binary electrolyte due to the presence of polymer backbone. To confirm the hypothesis, I have conducted the comparative study as a fundamental research, comparing the thermally induced voltage in polyelectrolyte and polyvinyl alcohol (PVA)-based binary electrolytes. Through the fundamental studies, it is shown that the polymer electrolytes have the advantages over the binary electrolytes, confirming the benefit of polymer chains creating the charged pathways which presumably enhance the Soret coefficient of mobile ions.

Chapter VI provides summary of this dissertation and direction for future research. This dissertation develops efficient n-type conversion method of CNT and successfully demonstrated that organic CNT-based thermoelectric device can produce sufficient power output to operate actual working device including glucose sensor.

Second, this work shows extremely large voltage generation under a temperature gradient in solid-state polyelectrolytes. Also, it is confirmed the importance of polymer chain by showing the higher thermopower of polyelectrolyte than that of salt-electrolyte sample. Finally, it is successfully developed novel thermally chargeable solid-state supercapacitor that can be charged by heat energy without external power sources.

CHAPTER II

LITERATURE REVIEW

Low-grade heat is one of the most sustainable, clean, and promising energy source for standalone self-powered systems including wearable/portable electronics and remote systems inaccessible to power grids. Among various thermal energy conversion mechanisms, solid-state thermoelectric energy conversion using the Seebeck effect [1-12] is most popular in the utilization of typically wasted low-grade heat. In addition to conventional inorganic thermoelectrics, recent efforts have also shown promising results in organic thermoelectrics for energy harvesting that could power up flexible and wearable electronics [13-17, 24-27]. One of their notable drawbacks, however, is small voltage due to intrinsically small Seebeck coefficients (typically 10~100 μV/K), compared to 3~5V required for typical small electronics.

Therefore, recently different mechanisms of thermal energy harvesting, especially Soret effect, have gained strong interest from research communities owing to their relatively large voltage generation. Therefore, in this work, I have been interested in the Soret effect which can be utilized in solid-state ionic conductors to generate large voltage by using thermodiffusion of ions. If we efficiently utilize this high thermopower of the Soret effect, it would be relatively easy to satisfy the minimum voltage with smaller number of components and simple design.

In this dissertation, fundamental mechanisms of two different thermal energy conversion concepts, Seebeck effect and Soret effect, will be introduced. Also, recently

reported state-of-the-art thermal energy harvesting systems based on carbon-based organic materials will be discussed to develop an efficient thermal energy harvesting systems in this work.

2.1 Seebeck effect

When the two ends of electronic conductors including metal and semiconductors have different temperatures, there is the creation of electrical potential in the electronic conductors. This phenomenon was firstly discovered by German physicist Thomas Johann Seebeck in 1821.

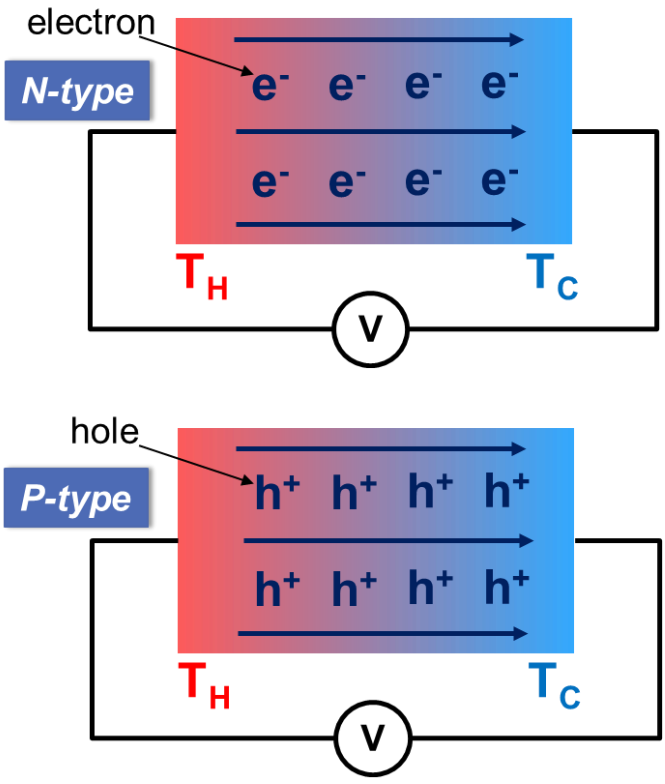

Figure 1. Seebeck effect in (a) n-type and (b) p-type semiconductors.

Figure 1 shows the mechanisms of the Seebeck effect in n- and p-type semiconductors under a temperature gradient. When there is a temperature gradient along the material, electrons (or holes) at hot side become higher energy state, resulting in higher moving speed. In contrast, electrons (or holes) at cold side will move at lower speed. As a result of this energy imbalance between hot and cold side, charge carriers (electrons or holes) tend to move from hot side to cold side in order to reach equilibrium. Thus, more negative charges (electrons) accumulate in n-type and more positive charges (holes) accumulate in the p-type at cold side, inducing a thermoelectric voltage in the materials. Among various applications, the Seebeck effect has been utilized to convert heat directly into electricity, which is called as thermoelectric energy conversion.

Over the past several decades, there has been great improvement of thermoelectric performance. For example, recent great enhancement in the thermoelectric efficiency of inorganic alloy materials based on Bi-Te-Sb-Pb [28-30] makes thermoelectrics more attractive for a variety of applications such as power generation as well as heating/cooling devices. However, despite its better performance, inorganic thermoelectric materials have some limitations in high cost, toxicity, heavy weight and complicated fabrication process. Therefore, this dissertation will focus on developing organic thermoelectric materials that have great advantages such as flexibility, light-weight, low cost, and easy to fabricate.

2.1.1 CNT-based thermoelectric materials

CNT has been intensely studied as a good thermoelectric material owing to its high electrical conductivity, light-weight, and low cost. Also, it has been reported that electronic band diagram of CNT is relatively easy to manipulate by making CNT-polymer nanocomposites as well as changing the doping level. Kunadian *et al.* reported that the carrier concentration of CNT was altered by doping with boron and nitrogen [31]. The thermal conductivity of doped CNT was decreased up to 75% due to the defects in the CNT. Also, the Seebeck coefficient was enhanced by increasing the carrier concentration via oxygen doping process.

Yu *et al.* reported that CNT and poly(vinyl acetate) (PVAc) latex composites showed the decoupling behavior between electrical conductivity and Seebeck coefficient, resulting in higher power factor values [14]. This behavior can be explained by an energy barrier for electronic transport at the junctions between CNT and polymer, making the Seebeck coefficient insensitive to the change of electrical conductivity. Recently, CNT were used as fillers in polymer composites and their electrical conductivities were extremely larger than other polymer composites with conductive fillers, resulting in dramatically enhanced power factor [16-17].

The thermoelectric properties can be controlled by decorating metal nanoparticles onto the CNT surface with galvanic displacement method. Choi *et al.* reported the p-doping method with gold nanoparticles to dramatically improve the electrical conductivity of CNT films [32]. With the p-type doping, the electrical conductivity of the CNT films was dramatically enhanced to ~6×10^5 S/m by decorating

15-vol% of gold nanoparticles onto the CNT films. Yu *et al.* also showed that the decoration of copper nanoparticles onto the CNT decreased the carrier concentration of CNT by injecting electrons into the p-type semiconducting CNT films [33].

2.1.2 N-type conversion of CNT and thermoelectric device

Even though organic thermoelectric materials have great advantages in flexibility, light-weight, and low cost, it is not easy to prepare n-type characteristics of organic materials due to the oxidation process in ambient air and this is one of the major limitations to develop organic thermoelectric device which consist of p- and n-type components. Over the past several decades, researchers have been putting a lot of effort into developing efficient n-type conversion methods.

There have been several methods to produce air stable n-type CNT, including wrapping a protective film around the CNT preventing oxygen doping and low work function metal particle depositions onto the CNT [34-35]. Recently, amine group containing polymer including polyethylene imine (PEI) has been reported to be good n-type conversion agent with its electron rich characteristics. Shim *et al.* and Ryu *et al.* demonstrated that the physical adsorption of PEI onto CNT results in a conversion of p-type into n-type CNT [36-38].

To produce sufficient power as well as voltage at a given temperature gradient, thermoelectric device needs to have p- and n-type components connected electrically in series and thermally in parallel. Yu *et al.* fabricated flexible thermoelectric device that consists of CNT-based p- and n-type films [15]. Also, they demonstrated that generating

power from thermoelectric device is proportional to the number of p-n junctions. Hewitt *et al.* reported simple stacking method to fabricate flexible thermoelectric device containing 72 p- and n-type CNT-based components [39]. At a 50 K of temperature gradient, the flexible thermoelectric device can produce 26 mV of open circuit voltage and 137 nW of output power.

2.2 Soret effect

In redox-free ionic conductors or electrolytes, the physical origin of the thermally induced voltage is the characteristic response of the different ions to a temperature gradient. Thermo-diffusion of ions along the temperature gradient creates an ionic-charge gradient, resulting in thermally induced voltage, which can also be called "thermoelectric voltage". This phenomenon is called the Soret effect [40-44], in comparison to the Seebeck effect used for the traditional thermoelectric devices. To explain this phenomenon, the current flux (J_i) of i_{th} mobile ion species can be expressed as [45-50]:

$$J_i = -D_i\left(\nabla n_i + 2n_i\alpha_i\frac{\nabla T}{T} - n_i\frac{q_i E}{k_B T}\right) \tag{2.1}$$

which comprises normal diffusion with the Einstein coefficient D_i, thermo-diffusion with the reduced Soret coefficient α_i, and electrophoresis for monovalent ions, where q_i is the charge of ions, n_i is the ion densities, k_B is the Boltzmann constant, T is the temperature, and E is the electric field. In a macroscopic binary electrolyte with

monovalent ions, Eq. (2.1) can be rewritten as follows for a steady-state ($\sum J_i=0$) and no net charge density ($\sum q_i \nabla n_i=0$) condition:

$$E = \frac{dV}{dx} = -\left(\alpha_{cation} - \alpha_{anion}\right)\left(k_B/e\right)\frac{dT}{dx} \tag{2.2}$$

where e is the elementary charge ($q=+e$ for cation and $q=-e$ for anion). One of ion species diffuses more rigorously or in the opposite direction, resulting in a thermally induced voltage between hot and cold sides. The magnitude of the voltage is proportional to the temperature gradient and the difference of the reduced Soret coefficients the ions.

2.2.1 Relative magnitude of thermally induced voltage

As shown in Eq. (2.2), thermally-induced voltage is proportional to the difference of the reduced Soret coefficients for cation and anion. For instance, when both cations and anions move to the same direction (Figure 2(a)), the difference ($\alpha_{cation} - \alpha_{anion}$) in the Soret coefficients becomes small, resulting in a small voltage. As illustrated in Figure 2(a), the ratio of cation to anion on the hot side is similar to that on the cold sides, so the voltage generated becomes small. On other hand, as illustrated in Figure 2(b), when cations move to the right and anions stationary, the difference of the Soret coefficients are large, resulting in a large voltage.

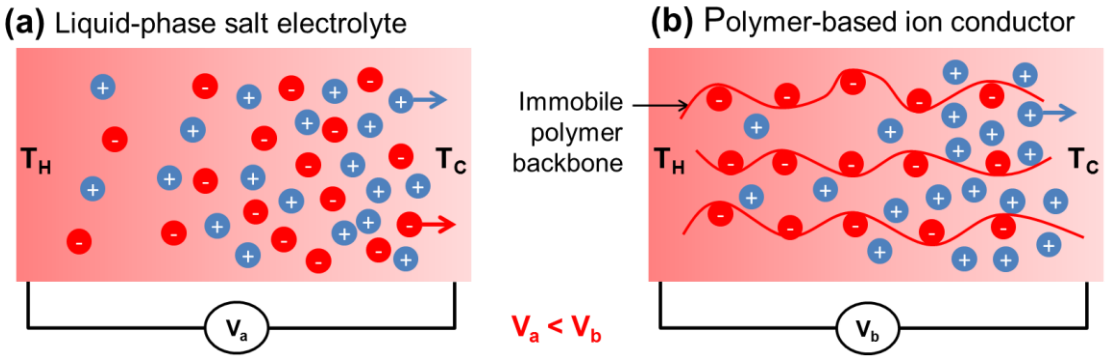

Figure 2. Schematic illustrations of thermo-diffusion of ions under a temperature gradient in (a) liquid-phase salt-based electrolytes and (b) polymer-based ionic conductors.

2.2.2 Small thermally-induced voltage from liquid-phase salt-based ionic conductors

In comparison to the Seebeck effect, the Soret effect has not been rigorously studied, and previous studies have been focused on "liquid"-phase salt-based ionic conductors. For typical salt-based liquid phase ionic conductors, cations and anions tend to move in the same direction like Figure 2(a), generating relatively low voltages. According to a recent paper from Wurger *et al.* [49, 51], thermally induced voltage for a sodium chloride (NaCl) solution is +0.05 mV/K and a sodium hydroxide (NaOH) solution produced a negative value, -0.22 mV/K. First of all, the magnitude of the voltage generated is relatively small. The sign is determined by the relative responsiveness of cation and anion to a temperature gradient. The stronger tendency of OH^- ions to diffuse toward the cold side than that of Na^+ ions generates a negative voltage. Na^+ ions are slightly more mobile compared to Cl^- ions, so a small positive voltage was observed from the NaCl solution. Sokolov *et al.* [52] reported that a hydrochloric acid solution gave +0.21 mV/K, and Sehnem *et al.* [47] showed that a nitric

acid solution produced +1.5 mV/K. Thermopower values from these conductors are typically smaller than ~1 mV/K.

2.2.3 Large thermally-induced voltage from polymer-based ionic conductors

Differing from liquid-phase salt solutions, solid-state polymer-based ionic conductors have a great advantage in increasing the thermally induced voltage. Lighter cations (or anions) are tethered to heavier polymer backbones with anions (or cations). Then the concentration of cation (or anions) can be much higher on one side than that of the other side like Figure 2(b), resulting in high thermopower values. This can be confirmed using Eq. (2.2). The generated voltage for a given temperature gradient gets higher when one of the reduced Soret coefficients (α_{anion}) is close to zero.

2.2.3.1 Liquid-phase polymer-based ionic conductors

A high thermoelectric voltage of 11 mV/K was observed by Zhao *et al.* [23] from a liquid-state polymeric electrolyte. It also has been reported that an addition of a polyelectrolyte to a salt solution can increase the Soret coefficient of ions by two orders of magnitude [53]. This confirms that less-mobile charged polymer backbones significantly contribute to the selective transport of mobile counter ions.

Although these liquid-phase polymer-based ionic conductors produced very large thermally induced voltage, their electrical conductivities were reported to be undesirably very low (10^{-3}~10^{-2} S/m) [20, 23]. The low electrical conductivity can significantly limit current, which implies that the application areas could be quite narrow or performance

could be considerably degraded. Moreover, it is hard to maintain temperature gradients in liquid-phase conductors because of heat convection (mixing of hot and cold liquid). For wearable and portable device applications, it requires bulky packaging to prevent leakage.

2.2.3.2 Solid-state polymer-based ionic conductors

Solid-state ionic conductors have also produced large thermoelectric voltages. Compared to the liquid-state devices, solid-state ionic conductors have great advantages in maintaining the temperature gradient (no convection) and eliminating bulky leak-proof packaging for device applications.

Recently, Chang *et al.* [21] reported that the solid-state thermogalvanic system based on polymer electrolytes, silver polystyrene-sulfonate (PSSAg) can produce high thermo-induced voltage (5 mV/K) by utilizing the thermo-diffusion of ions at 100% relative humidity. In addition, Ali *et al.* [54] showed that poly(sodium-4-styrene sulfonate) (PSSNa) film generated 5~10 mV/K at 80% relative humidity.

Chang *et al.* also reported a simultaneous enhancement of thermopower and electrical conductivity when the relative humidity in the environment increases [21]. This favorable behavior is very different from traditional thermoelectric materials as well as liquid-based ionic conductors, which typically shows inverse relations between thermopower and electrical conductivity [20]. Nevertheless, due to the lack of study in this area, the thermal diffusion mechanisms in this type of materials and the thermally-induced high thermopower are barely understood.

CHAPTER III

FLEXIBLE POWER FABRICS MADE OF CARBON NANOTUBES FOR HARVESTING THERMOELECTRICITY[*]

3.1 Introduction

Thermoelectric (TE) devices directly convert heat energy into electrical energy and vice-versa without moving parts and complicated components/structures. They are simply made by alternatively connecting solid-state p-type and n-type semiconductors in series. These unique characteristics make TE devices very attractive for compact power generation and cooling. It is also feasible to harvest low-grade heat (low exergy) to generate electricity. For instance, a TE device may provide enough power to a sensor for sensing and wireless communication without external power supplies. Exemplary applications include self-powered health monitoring for humans and buildings as well as gas/chemical detection without wiring. Current commercial TE devices typically consist of expensive, toxic, and heavy inorganic materials, hindering a full utilization of their unique benefits. Recently, there have been efforts to alleviate the problems by adopting p-type polymeric materials such as poly(3,4-ethylenedioxythiophene) and polyaniline due to their intrinsically low thermal conductivity [13-14, 16-17, 32, 38, 55-56]. N-type organic materials with decent thermopower values have rarely been reported [15, 37-38].

[*] Reprinted with permission from S. L. Kim, K. Choi, A. Tazebay, C. Yu, Flexible power fabrics made of carbon nanotubes for harvesting thermoelectricity, ACS Nano, 8, 2377-2386, Copyright 2014 by American Chemical Society.

Therefore, there has been no flexible and light-weight organic thermoelectric devices generating enough power to operate an actual working device.

Here we successfully demonstrated that carbon nanotubes (CNTs) can be made into both p- and n-type materials with relatively high thermopower and thereby a CNT-based thermoelectric device can generate enough power to operate an electrochromic glucose sensor. In fact, CNTs have been excluded from thermoelectric materials due to the high thermal conductivity (~10^3 W/m-K at room temperature [57]) of individual CNTs, which is disadvantageous for creating a large temperature gradients necessary to obtain a large thermoelectric voltage. Moreover, individual CNTs exposed to air show only p-type behaviors with small thermopower values [57]. This work presents that these drawbacks of CNTs for thermoelectrics have been overcome by properly designing the junctions between CNTs and the surface of CNTs as well as making many junctions in their films (or mats) through rigorous de-bundling processes. When CNT surfaces are functionalized by molecules or chemical agents, electronic transport across CNT-molecule-CNT junctions can be optimized to increase thermopower by creating a small energy barrier. The presence of the junctions can also play a significant role in deterring phonon transport due to dissimilar vibrational characteristics between CNTs and molecules.

We present not only synthesis and characterization of both p- and n-type, flexible, and CNT-based thermoelectric materials, but also design and fabrication of TE modules to maximize electricity generation. More importantly, the TE device has been tested for operating a glucose sensor, demonstrating the feasibility of using the device

for practical applications. For p-type materials, oxygen-doped CNTs were functionalized with sodium dodecylbenzenesulfonate (SDBS) to control thermopower as well as separate CNT bundles. Multiple dopants, polyethylenimine (PEI), diethylenetriamine (DETA), and $NaBH_4$ were utilized for maximizing n-type characteristics. It has been shown that PEI is effective to make n-type CNTs [15, 37-38], but the large molecules are electrically insulating, resulting in a reduction of electrical conductivity. Here, we used shorter DETA molecules composed of amine groups containing lone pairs of electrons so as not to considerably sacrifice electrical conductivity.

The n-type conversion mechanism and the role of the molecules coated on CNTs by the functionalization were thoroughly explained with a complete picture of electronic band diagrams in conjunction with electronic transport properties, which are of great importance in understanding the behaviors but have been barely studied in the past. The highest occupied molecular orbital (HOMO) and lowest unoccupied molecular orbital (LUMO) energy levels were found by performing cyclic voltammetry (CV) and ultraviolet-visible-infrared (UV-vis-IR) spectroscopy. The Fermi level was determined by using a Kelvin probe method, and the Hall measurement was carried out to obtain the type of carrier (electron or hole) as well as free carrier mobility. The following describe material synthesis, characterization, device design, and sensor operation.

3.2 Experimental

3.2.1 Material synthesis

CNTs purchased from CheapTubes, Inc. were used for all experimental work. According to manufacturer's specifications, CNTs were synthesized by a chemical vapor deposition method and contain approximately 50/50 wt% single/double-wall tubes with 99 wt% purity. The outer and inner diameters of the CNTs are 1-2 nm and 0.8-1.6 nm, respectively, and their lengths are 3-30 μm. Five-mg CNTs were dispersed in 20-ml deionized (DI) water with 15-mg SDBS (88 %, Acros Organics) to prepare CNT solutions. Sonication was conducted in two modes, bath type sonicator (Branson 1510) for 6 hours followed by a probe sonicator (Misonix Micron XL2000 Ultrasonic Homogenizer) for 2 hours.

In order to synthesize p-type CNT films, the as-prepared CNT solution was vacuum-filtered onto a PTFE membrane (pore diameter: 0.45 μm, thickness: 45 μm, Tisch Scientific) with additional DI water, and subsequently the film was dried in air at 50 °C. For n-type CNT films, mixtures (1 g) of PEI (branched, molecular weight: 600, 99 %, Alfar Aesar) and DETA (99 %, Alfar Aesar) with PEI:DETA ratios of 100:0, 67:33, 50:50, and 33:67 were dissolved in 9-ml DI water. This aqueous solution (10 g) was added to the CNT solutions (20.02 g). This mixture solution was stirred for 48 hours at 50 °C, and then the solution was vacuum-filtered onto a PTFE membrane with additional DI water. Subsequently, the film was dried in air at 50 °C. For additional doping with sodium borohydride ($NaBH_4$, purity: 98 %, Fisher Scientific), the dried film was immersed in an aqueous 1-M $NaBH_4$ solution for 24 h, and then dried in air at 50

°C. The thickness of the CNT layer in the film was measured to be 8 μm under a scanning electron microscope by inspecting cold-fractured cross-sections of the CNT films.

3.2.2 Thermoelectric device fabrication

As-prepared CNT films on a PTFE membrane were cut into rectangular shapes 4 mm in width and 25 mm in length. Typical thickness of the CNT films was 8 μm. The thermoelectric modules were made by alternatively connecting p- and n-type CNT films electrically in series with aluminum foils using a silver adhesive (silver adhesive 503, electron microscopy sciences), and thermally in parallel by stacking 9 p-type and 9 n-type films. In order to avoid electrically connecting films in the stacking direction, PTFE tapes (75 μm thickness, McMaster Carr) were inserted between p- and n-type films. In order to maximize the voltage and power output, total eight modules (stacks) were connected electrically in series.

3.2.3 Glucose sensor fabrication

Transparent electrodes were prepared by spraying a mixture of 2-mg CNTs and 10-g PEDOT:PSS (Clevios PH1000, H.C. Starck) on glass slides (25 mm × 10 mm) at ~80 °C with a spray gun (0.2 mm nozzle diameter, GP-S1, Fuso Seiki Co.). The CNTs in the mixture were dispersed by the probe sonicator for 2 hours prior to the spraying process. The sheet resistance of the transparent electrode was measured to be 1~1.5 kΩ/sq. For electro-depositing Prussian blue (PB) on the transparent electrode, a plating

solution (100 ml) containing 2.6 mM HCl (36.5~38%, EMD millipore), 10 mM $K_3Fe(CN)_6$ (98.5%, Acros Organics), and 10 mM $FeCl_3$ (98%, Alfar Asear) was freshly prepared. The electrode was covered by a PTFE tape with a 1-mm diameter hole, and subsequently immersed in the solution. PB was galvanostatically deposited by 0.4 $\mu A/mm^2$ for 30 s with Ag/AgCl as a reference electrode and Pt as a counter electrode. The glucose sensing paper was prepared by drop-casting 40 μL of a 0.01 M phosphate buffered saline (pH 7.4, ultra high purity grade, Amresco) containing 125 mM $K_3Fe(CN)_6$ and 500 unit (106 U/mg at 37 °C) of glucose oxidase (GO_x, Amresco) onto a chromatographic paper (10 mm × 10 mm, Whatman). After being dried at ambient air, the paper was sandwiched between the PB deposited electrode and a bare CNT electrode. A Nafion membrane (N-115, Dupont) was used for separating the sensing paper from the PB deposited electrode. The glucose solution contained 0.5-mM anhydrous D-(+)-Glucose (99 %, Alfa Aesar).

3.2.4 Electrical property measurements

Electrical properties of CNT films, including electrical conductivity and thermopower, were measured at room temperature along the in-plane direction. A four-probe method was employed to obtain electrical conductivity from linear current-voltage relations by multiplying geometrical factors. For thermopower measurements, thermoelectric voltage across the sample was measured at 10 different temperature gradients between -10 and +10 K and then thermopower was obtained from the slope of temperature gradient-voltage data.

3.2.5 Sample characterization

The surface and cross-section of the carbon nanotube films was inspected by using a field-emission SEM (FEI Quanta 600). FTIR (Nicolet 380, Thermo Fisher Scientific) was performed in conjunction with attenuated total reflectance accessory (AVATAR OMNI Sampler, Germanium crystal) under an ambient condition. Electrochemical measurements were carried out with a CHI 600 electrochemical analyzer with a three-electrode system at a scanning rate of 20 mV/s in an anhydrous acetonitrile solution (98 %, Sigma-Aldrich) containing 0.1-M Bu_4NPF_6 (98 %, Sigma-Aldrich) and 0.01-M $AgNO_3$ (99.9 %, Alfa Aesar). 70-sccm Ar was purged into the solution for 1 hr to remove oxygen from the solution. A glassy carbon was used as a working electrode; a platinum-wire was used as the counter electrode; and an Ag/Ag^+ electrode was used as the reference electrode. When ferrocene was used as an external standard (−4.8 eV vs. vacuum), the half wave potential $E_{1/2}(Fc/Fc^+)$ was measured to be -0.04 V vs. Ag/Ag^+. For the electrochemical and UV-vis-IR measurements, samples were prepared by spraying the CNT-containing solutions on the glassy carbon or polished quartz substrates for 180 sec (similar to the method for preparing the transparent electrodes). Transmittance was measured by using a UV-vis-NIR spectrophotometer (Hitachi U-4100). For Kelvin probe measurements, the local surface potential of the samples was measured with a Dimension Icon AFM (Bruker) using a Pt-coated cantilever with 30 nm lift height with a 75 kHz tapping mode. Sheet resistance and the Hall measurements with the Van der Pauw geometry (15 mm×15 mm) were performed with a homemade setup following the ASTM F76-08 method.

3.3 Results and discussion

3.3.1 Optimization of p- and n-type performance of CNT films

The p-type modules were made of as-purchased CNTs by filtering aqueous solutions containing CNTs dispersed by SDBS. When CNTs are exposed to air, they become p-type due to oxygen doping without any additional chemical treatments [14-17, 33, 37, 58-59]. In this study, we used CNTs synthesized by a chemical vapor deposition (CVD) method in order to obtain a relatively high thermopower. According to our previous study [59], it was found that single-wall CNTs grown by a CVD method exhibit relatively high thermopower than those grown by an arc discharge method and a high pressure carbon monoxide method.

While thermoelectric properties of individual CNTs are strongly affected by chirality and the number of walls, a bulk form of CNTs, typically called a CNT mat (or film) has electrical properties dissimilar to those of individual CNTs. Thermoelectric properties of a CNT mat are strongly affected by the degree of dispersion and the type of dispersants as well as junctions between CNTs. While it is feasible to increase the electrical conductivity of CNT mats up to ~7×10^4 S/m with SDBS [59], the focus of this study is to increase thermopower for high output voltage. We thickened the SDBS junction between CNTs using a 3:1 weight ratio of SDBS to CNT, so as to raise thermopower up to 97 μV/K (with 1.1×10^4 S/m), which is higher than our previous experimental result, 44 μV/K with a 2:1 weight ratio of SDBS to CNT.

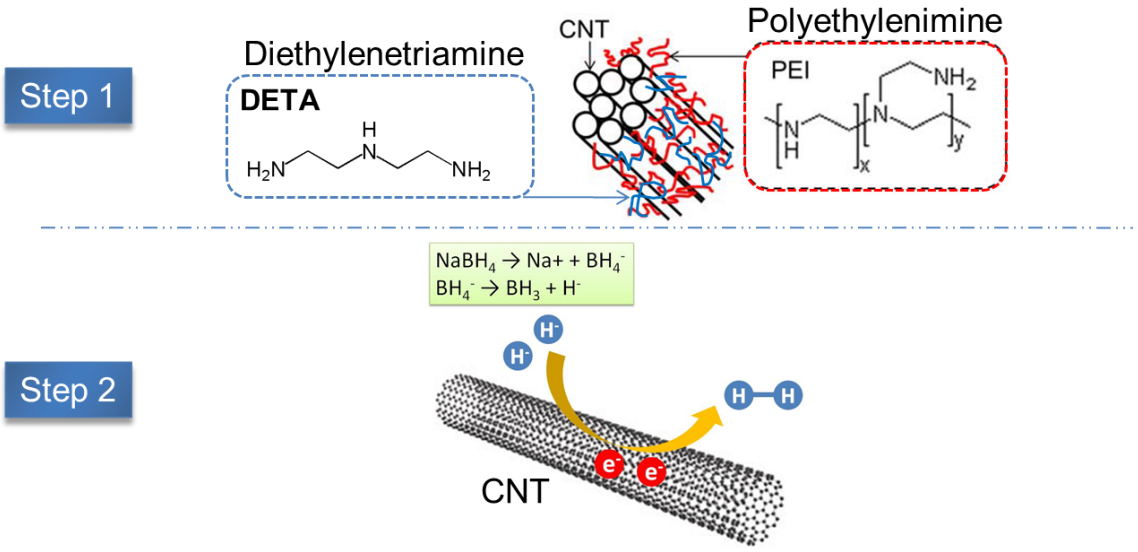

Figure 3. Two step n-type conversion processes. (Step 1) PEI and DETA treatment (Step 2) Reduce the CNT surface by using $NaBH_4$ to additionally inject electrons into the CNT. $NaBH_4$ is well-known material as a strong reducing agent.

Air-exposed CNTs were reduced by using PEI and DETA with subsequent $NaBH_4$ treatment in order to make n-type modules (Figure 3). When PEI coats CNTs, p-type CNTs were effectively converted to n-type [15, 37-38]. However, PEI is electrically insulating and thereby deters electronic transport at the junction between CNTs. This is related to a large molecular weight (i.e., long chain) of PEI, increasing the thickness of electrically insulating coating layers. In order to alleviate this problem, DETA, a short molecule with similar to the structure of PEI, was introduced. The nitrogen in DETA can play a role in n-type doping like PEI [60].

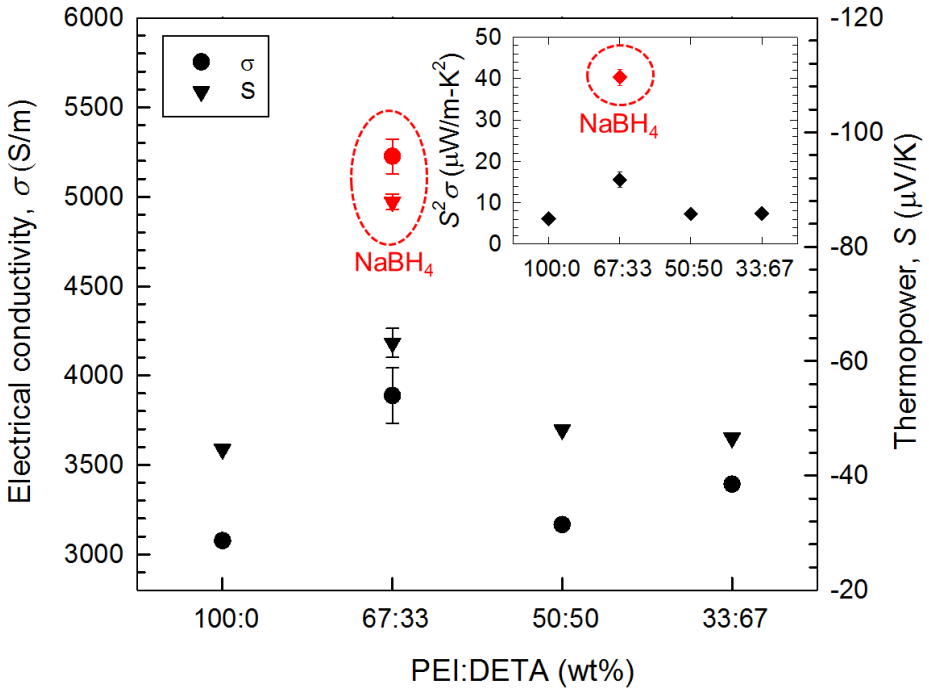

Figure 4. Electrical conductivity (circle) and thermopower (triangle) of the n-type CNT films with different PEI to DETA weight ratios. The inset shows the thermoelectric power factors ($S^2\sigma$). The samples with the PEI:DETA of 67:33 were further reduced by $NaBH_4$. The average measurement values and error bars for the samples with the PEI:DETA of 67:33 were obtained from three different samples (reprinted from [61]).

The weight ratio of PEI to DETA was varied in order to find a ratio maximizing the power factor ($S^2\sigma$, where S and σ stand for thermopower and electrical conductivity, respectively). When 33 wt% PEI was replaced by DETA, the electrical conductivity was improved to 3,900 S/m from 3,100 S/m of a 100-wt% PEI sample, as depicted in Figure 4. At the same time, thermopower was also improved to -63 μV/K, presumably due to small molecules additionally attached to CNT surfaces that are inaccessible by large PEI molecules. Nevertheless, with larger amounts (50 and 67 wt%) of DETA, the absolute value of thermopower was decreased with electrical conductivity reductions. We believe

this is caused by weak doping from DETA. With only DETA as a doping agent, the typical thermopower value of CNT mats (~40 μV/K) [59] were diminished to 8.4 μV/K, but thermopower values were still positive, suggesting the presence of mixed free carriers (holes and electrons). We believe that the mixed carriers decreased the electrical conductivity with the DETA ratios higher than 33%. The sample doped by 67/33-wt% PEI/DETA was additionally reduced by $NaBH_4$, and the electrical conductivity and thermopower were further improved to 5,200 S/m and -86 μV/K, respectively. This resulted in an increase of the power factor to 38 μW/m-K^2, compared to that of the sample doped by only PEI, as shown in the inset of Figure 4.

Thermopower contains two contributions from holes and electrons with opposite signs. When two different types of carriers are present, thermopower can be described as:

$$S = (S_e\sigma_e + S_h\sigma_h)/\sigma \tag{3.1}$$

where S_e and S_h stand for thermopower due to electrons and holes, respectively; σ_e and σ_h stand for electrical conductivity due to electrons and holes, respectively; σ is the electrical conductivity due to both electron and hole carriers. When the contribution from electrons becomes dominant, the first term in Eq. (1) plays a major role, resulting in negative thermopower values. On the other hand, when the contributions from electrons and holes are comparable, thermopower becomes small due to the negative S_e and positive S_h. The increase of both electrical conductivity and thermopower is likely to be caused by the van Hove singularity in CNTs. When the Fermi level is raised towards

the band edge, thermopower becomes larger due to the asymmetry in the differential electrical conductivity of CNTs [33].

3.3.2 Morphology of p- and n-type CNT films

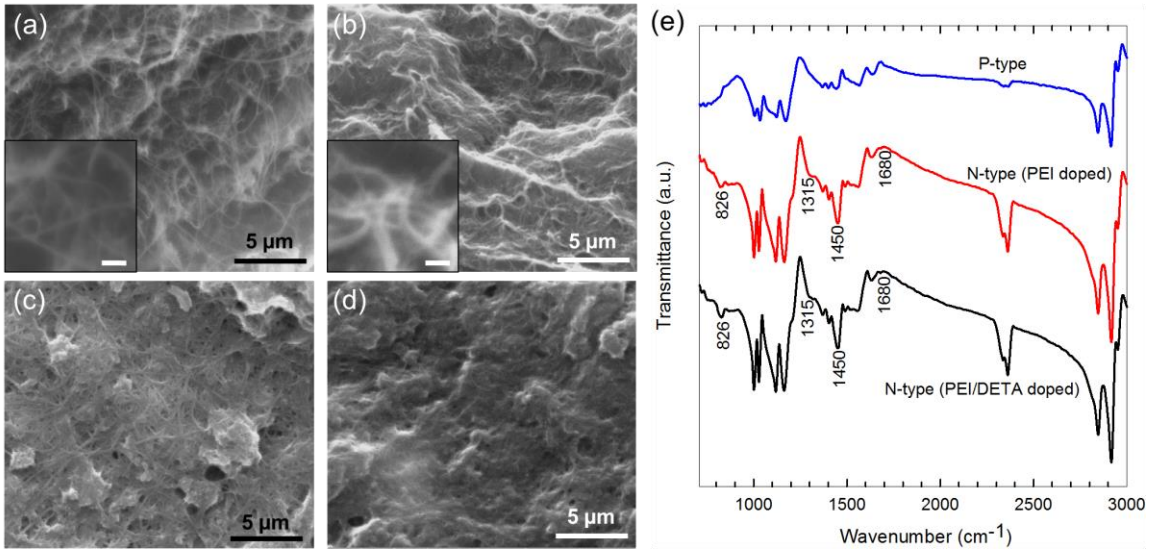

Figure 5. Cold-fractured cross sections of a p-type (a) and an n-type (b) CNT film. The film surface of a p-type film (c) and an n-type film (d). FTIR spectra of a p-type CNT, PEI-doped CNT, and PEI/DETA-doped CNT films (e). The scale bars in the insets indicate 100 nm (reprinted from [61]).

The presence of PEI in the samples was confirmed by scanning electron micrographs (SEMs) and Fourier transform infrared (FTIR) spectra. Figure 5(a) and (b) respectively show a cold-fractured cross section of p- and n-type CNT films. The tubular structures with relatively small diameters in the p-type CNT sample were clearly observed as opposed to the n-type CNTs whose diameters are relative large due to PEI

and DETA coating layers. The n-type CNTs are well embedded in the film, which indicate PEI/DETA coated most of exposed CNT surfaces with relatively thick coating layers. If the coating is not uniform, some of CNTs would have been pulled out from the surface like Figure 5(a). The insets also show the diameter change after the doping process. Similar features were also observed in the micrographs of the film surfaces, as shown in Figure 5(c) (p-type CNTs) and Figure 5(d) (n-type CNTs).

Figure 5(e) shows FTIR spectra of p-type CNT, PEI-doped CNT, and PEI/DETA-doped CNT films. When FTIR spectra from p-type CNTs are compared with those of PEI-doped and PEI/DETA-doped CNTs, distinct absorption peaks coming from PEI and DETA (nitrogen-containing groups) were observed. The absorption peaks at 826 cm^{-1} and 1680 cm^{-1} respectively suggests an out-of-plane bending (or NH_2 wag) and an in-plane NH_2 bending mode [62-64]. The absorption peak at 1315 cm^{-1} corresponds to secondary C-N stretch. An increase of the absorption peak at 1450 cm^{-1} with PEI and DETA compared to neighboring peaks may be due to primary C-N stretch [64-66]. Since PEI and DETA have similar chemical structures, their peaks are indistinguishable.

3.3.3 Electronic band diagram characterizations of CNT films

To have a better understanding of n-type conversion mechanism of CNT films, I tried to analyze the electronic band diagrams of CNTs film before and after polymer doping. In this work, diverse characterization methods were conducted to obtain the electronic band diagram. The electronic band diagrams of CNTs after doping with

PEI/DETA or/and $NaBH_4$ were investigated by using CV, UV-vis-IR, and Kelvin probe measurement data so as to understand n-type conversion mechanism.

First of all, the HOMO and LUMO energy levels found from CVs are shown in Figure 6, based on the onset potentials of oxidation and reduction using ferrocene as an external standard [67-68]. CNT films were prepared on a glassy carbon electrode and Ag/Ag^+ electrode was used as a reference electrode. The CV measurement was conducted in acetonitrile solution with 0.1 M hexafluorophosphate (Bu_4NPF_6) as supporting electrolyte at a scan speed of 20 mVs^{-1}. The onset potentials of oxidation and reduction are indicated by circles (p-type) and squares (n-type).

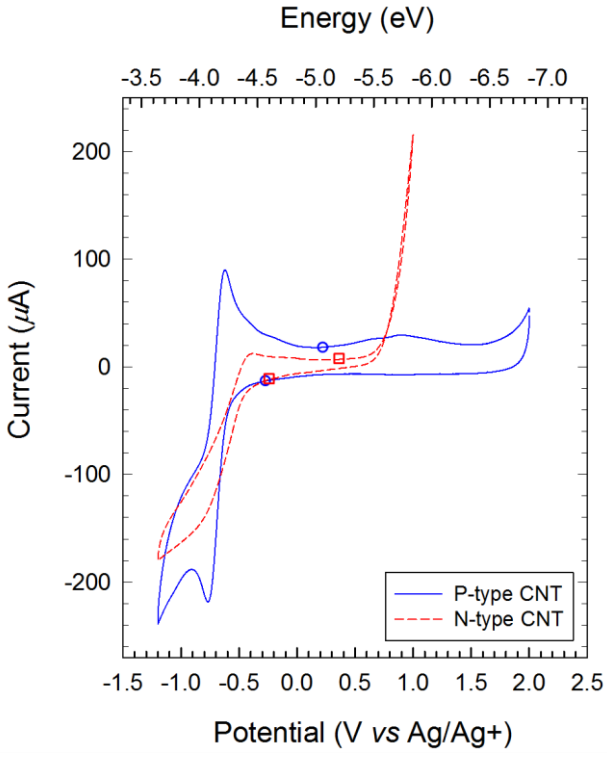

Figure 6. Representative cyclic voltammograms of p- and n-type CNT films (reprinted from [61]).

As shown in Figure 7, the CV curve of p- and n-type CNT films were calibrated by using Fc/Fc^+ redox couple. A glassy carbon electrode was used as a working electrode, a Pt wire was used as a counter electrode, and an Ag/Ag^+ electrode was used as a reference electrode in 0.01-M $AgNO_3$ in acetonitrile. The half-wave potential of Fc/Fc^+ redox couple ($E_{1/2}(Fc/Fc^+)$) was estimated from $(E_{ox} + E_{red})/2$, where E_{ox} and E_{red} are the oxidation and reduction peak potentials, respectively [67-68]. $E_{1/2}(Fc/Fc^+)$ was found to be -0.04 V [(-0.211 + 0.126)/2 = -0.04 V] relative to the Ag/Ag^+ reference electrode.

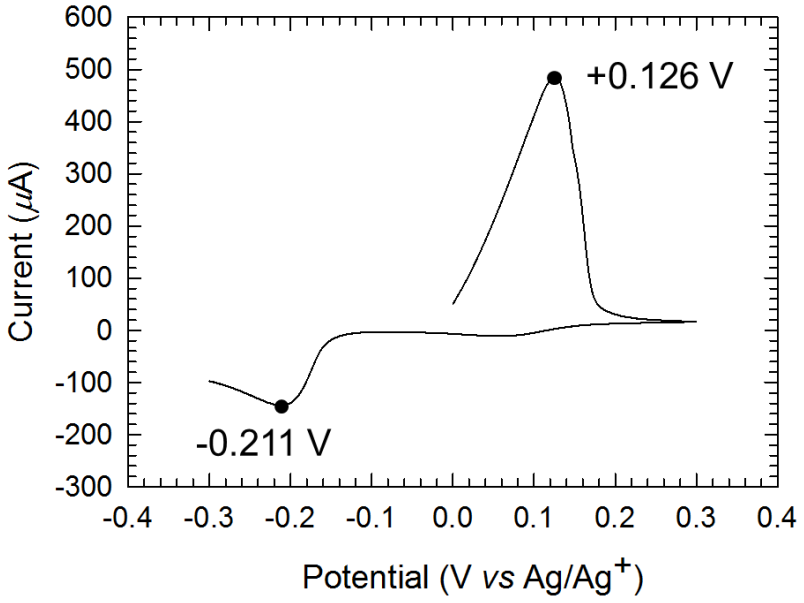

Figure 7. Ferrocene/ferrocenium (Fc/Fc^+) redox couple (a) as an external standard for calibrating cyclic voltammetry (CV) curve of p- and n-type CNT films (reprinted from [61]).

For p-type CNTs, HOMO and LUMO were estimated to be -5.05 eV and -4.59 eV from the vacuum level (0 eV), as shown in Figure 10. The HOMO and LUMO of n-type CNTs were almost constant with a small change in the HOMO level to -5.12 eV, resulting in a larger band gap (0.53 eV) compared to 0.46 eV from the p-type CNTs.

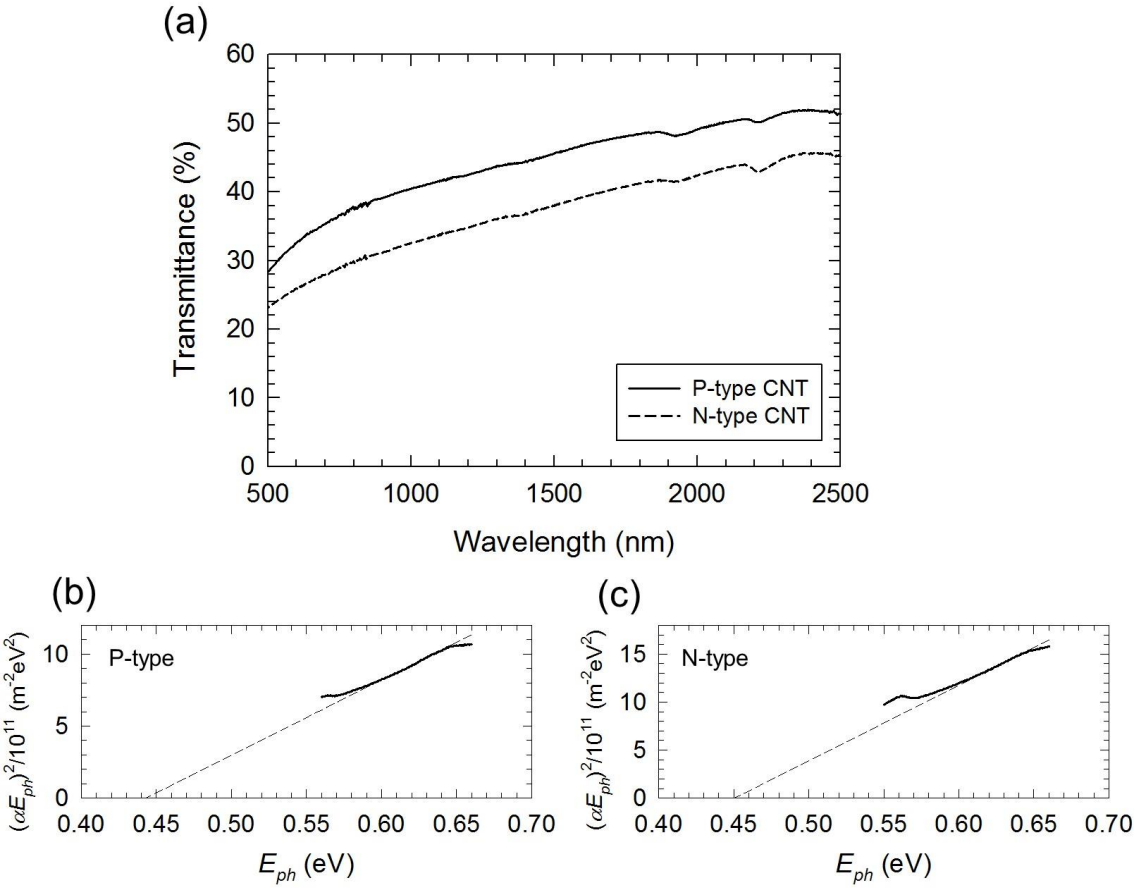

Figure 8. (a) UV-vis-IR transmission spectra of p- and n-type CNT films as a function of wavelength. Tauc and Davis–Mott plots: $(\alpha E_{ph})^2$ as a function of E_{ph} calculated from UV-vis-IR transmission spectra (solid lines) of (b) p- and (c) n-type CNT films (reprinted from [61]).

To confirm the reliability of the band gap information from the CV measurement, UV-vis-IR spectroscopy measurement was conducted, as shown in Figure 8. In Figure 8(a), the prominent peaks at 1900 nm originates from the E_{11} van Hove singularity transitions in semiconducting CNTs [69-70]. In this work, Tauc and Davis-Mott model, $(\alpha E_{ph})^n = B(E_{ph} - E_g)$ was used for determining the band gaps of CNT samples [69] (Figure 8(b) and (c)). E_{ph}, E_g, α, n, and B indicate photon energy, optical band gap, absorption coefficient, index representing the type of optical transition (typically n = 2 for direct band gaps) [69], and a constant, respectively.

Optical band gaps were found using UV-vis-IR spectra from the crossover points of the slopes with the x-axis [71], as shown in Figure 8. The p-type CNTs show 0.44 eV, which is very similar to the band gap measured by CV. On the other hand, the n-type optical band gap (0.45 eV) was found to be smaller by 0.08 eV, compared to that from the CV results. In the optical method, visible and infrared light energy is absorbed by both CNTs and PEI/DETA as the light passes through the samples. On the other hand, the electrochemical method relies on the charge interaction between an electrolyte and sample surfaces, and the presence of electrically insulating PEI/DETA coating layers on CNTs may have affected the measurement results. This difference in the two techniques could be the reason for the small discrepancy of the band gap measurement results. Considering the optical band gap, the HOMO of n-type CNTs could be located at -5.04 eV since LUMO is not likely to be raised towards the vacuum level by the donation of electrons from PEI/DETA.

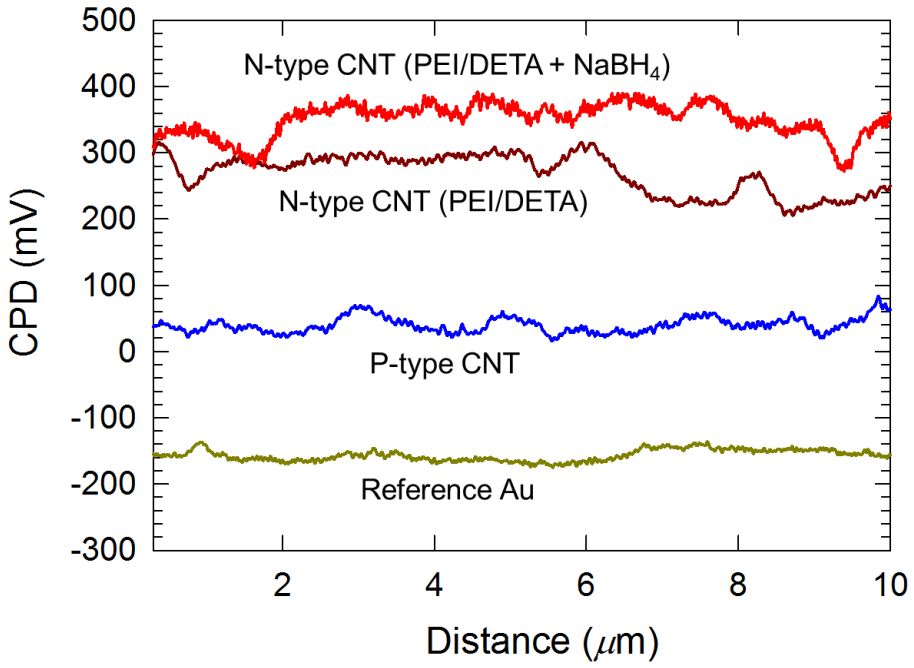

Figure 9. Kelvin probe method was used for measuring the contact potential difference (CPD) between a Pt-coated tip and a sample in ambient environment to examine the local work function difference between the tip and sample. (CPD = $WF_{tip} - WF_{sample}$). The work function of the Pt-coated tip was calibrated by a gold foil (99.95 %, 0.05 mm thickness, Alfar Aesar). Note that the CPD curves are representative data of each sample (reprinted from [61]).

Based on the band gap information, the location of the Fermi energy determines the type (p or n) of CNTs. In our study, a contact potential difference (CPD), which is the work function (WF) difference between a probe and a sample, was measured by using the Kelvin probe method in air environment (Figure 9). Since the WF of a probe tip may be affected by moisture and other contaminants in air, the CPD of a gold foil was measured for calibration, which was found to be -150 mV. If we assume that the Fermi level of the gold foil is located at -5.10 eV [72-74], the Fermi levels of p- and n-

type CNTs are estimated to be -4.91 eV and -4.69 eV, respectively, as shown in Figure 10. The Fermi levels of p- and n-type CNTs are respectively close to the HOMO and LUMO, which explains the n-type conversion (negative thermopower values) of air exposed p-type CNTs. It was also found that the $NaBH_4$ treatments further shifted the Fermi level (-4.61 eV) towards LUMO, indicating stronger n-type conversion upon reduction by $NaBH_4$. The physical properties of the p- and n-type CNTs are summarized in Table 1.

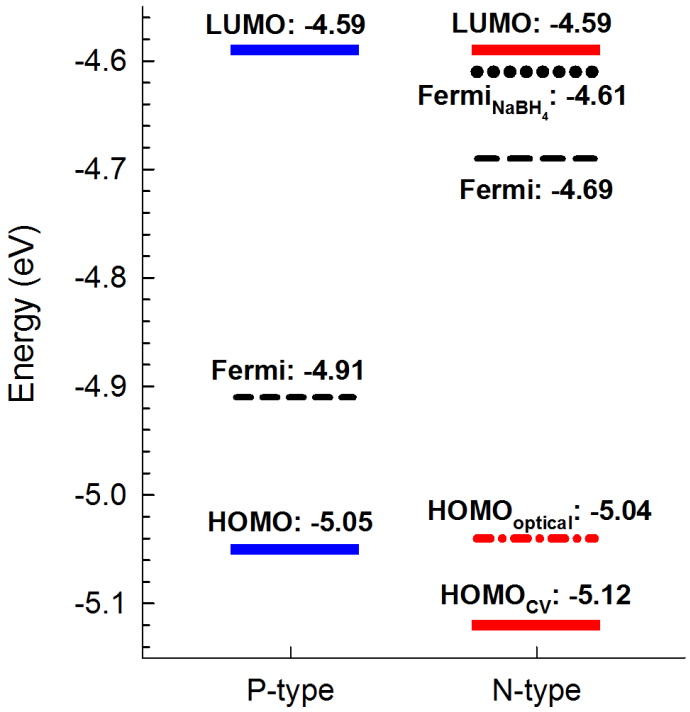

Figure 10. Electronic band diagrams of p- and n-type CNT films. HOMO, LUMO, and the Fermi level of p- and n-type CNT films. Two HOMO locations obtained by CV and UV-vis-IR results are indicated. The Fermi level from PEI/DETA doping (long dash) was moved up toward vacuum level after additional $NaBH_4$ doping (dotted) was performed (reprinted from [61]).

Table 1. Physical properties of p- and n-type CNT films (reprinted from [61]).

Sample	Oxidation onset / V	Reduction onset / V	HOMO / eV	LUMO / eV	CPD / V	Fermi level / V
P-type	0.21	-0.25	-5.05	-4.59	0.04	-4.91
N-type	0.28	-0.25	-5.12	-4.59	0.26 (0.34*)	-4.69 (-4.61*)

* PEI/DETA-doped CNT samples were further reduced by $NaBH_4$.

In order to have a complete picture of electronic behaviors upon doping, it is necessary to obtain free carrier mobility and concentrations. Therefore, we have performed both sheet resistance and hall measurements with the van der Pauw technique [75-76]. As summarized in Table 2, the hall voltages of p- and n-type CNTs were measured to be +8.50 μV and -12.6 μV with 20 mA, indicating that the majority carriers for p- and n-type are respectively holes and electrons. The carrier concentrations of p- and n-type CNTs were determined to be 1.86×10^{21} cm^{-3} and 1.25×10^{21} cm^{-3}, respectively. The relatively high carrier concentration suggests that electron donations to CNTs due to the lone-pair of electrons from the repeating nitrogen in PEI and DETA are very effective. The n-type (0.206 cm^2/V-s) mobility is smaller than that of p-type (0.365 cm^2/V-s), presumably due to the PEI/DETA coating layers that impede carrier transport across the junctions between CNTs. This mobility is much smaller than those of individual CNTs [77], presumably due to the junctions between tubes. This result

implies it may be possible to further improve the electrical conductivity by using shorter (or smaller molecular weight) and/or electrically conducting molecules as dopants.

Table 2. Hall measurement results of p- and n-type CNT films (reprinted from [61]).

Sample	Sheet resistance / Ω	Hall voltage* / μV	Carrier concentration / cm^{-3}	Mobility / $cm^2V^{-1}s^{-1}$	Majority Carrier
P-type	11.5	+8.5	1.86×10^{21}	0.365	Hole
N-type	30.3	-12.6	1.25×10^{21}	0.206	Electron

* Hall voltage was measured with 20 mA under 10120 G.

3.3.4 Fabrication of flexible thermoelectric device

The p- and n-type films were cut into 25 mm×4.0 mm (called legs), and they were alternatively connected electrically in series and thermally in parallel with electrically insulating polytetrafluoroethylene (PTFE) films between the legs, as schematically depicted in Figure 11(a). An as-assembled stack of legs (called a module) is shown in Figure 11(b) and (c). Each module was connected in series by copper foils as schematically shown in Figure 11(d). A picture of thermoelectric device is shown in Figure 11(e).

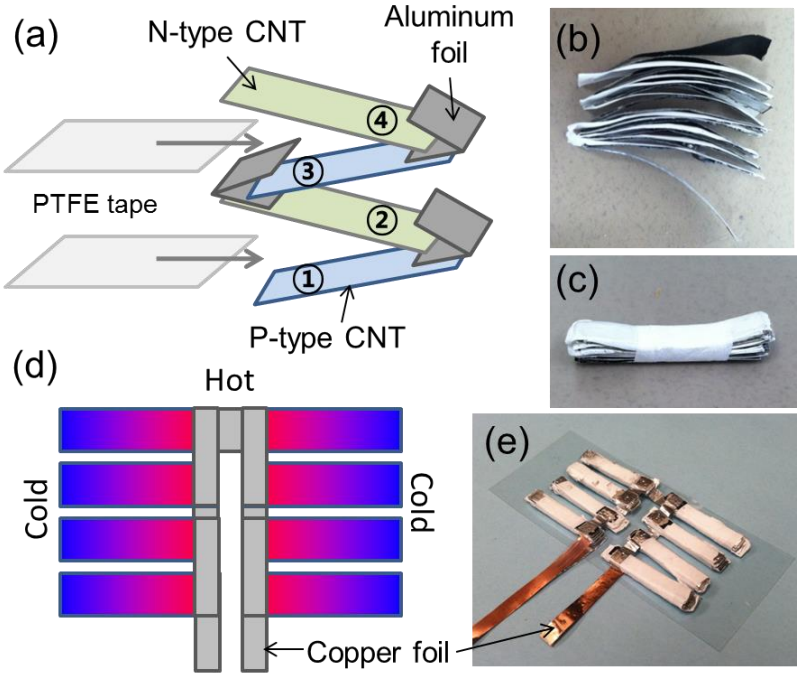

Figure 11. (a) Assembly process of p- and n-type carbon nanotube films. (b) One module (stack) consists of 9 p-type and 9 n-type films. (c) The module was bound by a PTFE tape. (d) A device design that maximize thermoelectric voltage generation for a given temperature gradient, and (e) Completed thermoelectric device consists of 144 films (72 p-type and 72 n-type) (reprinted from [61]).

This device architecture is to maximize thermoelectric voltage determined by thermopower ($S_{p\ or\ n}$) and temperature gradient between hot and cold sides ($\Delta T_{i\ or\ j}$) as well as the number of legs. The total thermoelectric voltage (V_{TE}) generated from the device can be described as:

$$\left|V_{TE}\right| = N_m \left[\sum_{i=1,3,5,\cdots}^{N_l-1} \left|S_p \Delta T_i\right| + \sum_{j=2,4,6,\cdots}^{N_l} \left|S_n \Delta T_j\right| \right] \tag{3.2}$$

where N_m and N_l respectively indicate the numbers of modules and legs in each module; the subscripts, p and n indicate p- and n-type; ΔT_i and ΔT_j stand for the

temperature gradient along the long edge of a leg indexed from the bottom to the top as shown in Figure 11(a).

3.3.5 Performance test of flexible thermoelectric device

To estimate the power generating performance of the thermoelectric device, I established the measurement set up which consists of 1 heating block in center and 2 heat sinks on both sides, as shown in Figure 12. The center part of the device was mounted on a heating block, where top and bottom aluminum blocks were heated to create temperature gradients.

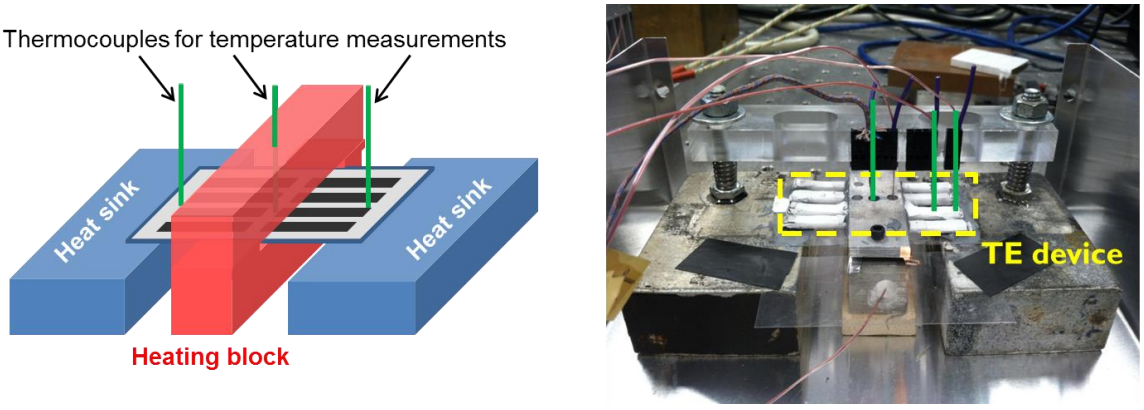

Figure 12. The TE device was tested by sandwiching it between two blocks heated by a cartridge heater (150 W, Omega) and a temperature controller. The two blocks were thermally connected by metal spacers so as to maintain uniform temperature. Both ends of the TE device were mounted on heat sinks (aluminum blocks) to maintain room temperature. Open circuit voltage was measured at various temperature gradients. The power testing was performed by connecting various load resistors to the TE module in series. Current and voltage were measured for a given temperature gradient (reprinted from [61]).

The output thermoelectric (open-circuit) voltage was measured to be ~9.3 mV per K, leading to 465 mV at ΔT=49 K, as indicated by circles in Figure 13(a). Load resistances were varied to record current as a function of the output voltage, and then the output power was plotted in Figure 13(b). The advantage of the stacking method is to increase the voltage generated by each leg, but temperature drop (ΔT_{drop}) was created on the hot side due the thermal resistance. Note that the modules were clamped with a moderate pressure (approximately 700 N/m^2) in order to simulate normal operation in practice.

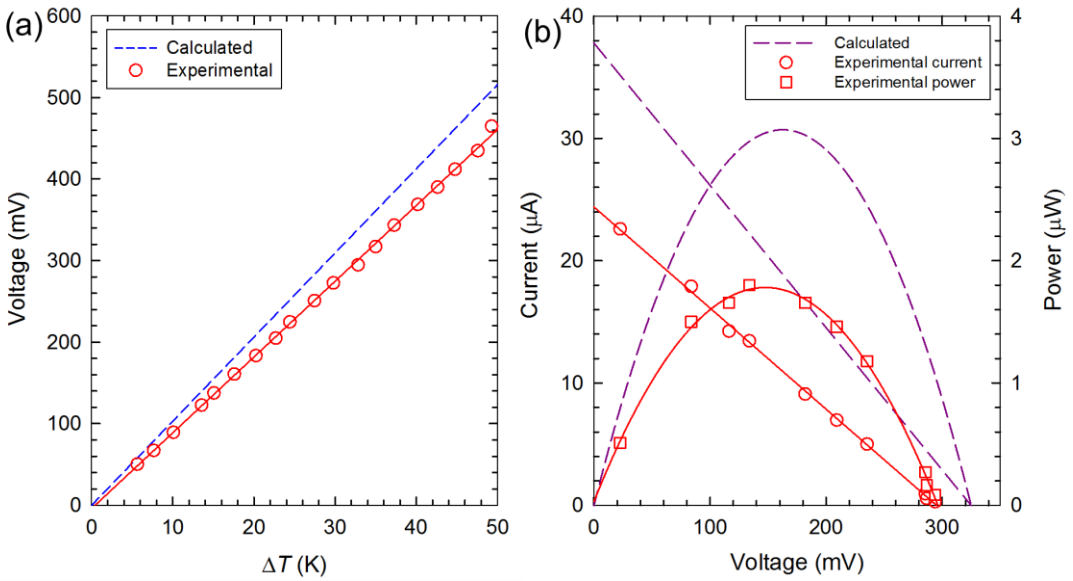

Figure 13. (a) Thermoelectric voltage generated by thermoelectric device as a function of temperature gradient. The discrepancy between the experimental values (circle) and the calculated voltage (short dash) would be due to misalignment during module assembly that created temperature drops in the hot side of the module. (b) Current-voltage and power output with varying load conditions at a ΔT= 32 K for operating an electrochromic glucose sensor. The calculated values (long dash) were obtained by assuming electrical contact resistance is negligible, suggesting further improvement in power output with an optimized assembly process (reprinted from [61]).

In order to estimate the temperature drop across each leg, the temperature of the top surface of a module was measured while the bottom part of the module was heated to 35, 45, and 55 °C. Assuming that there is a linear temperature drop along the thickness direction of the module at the heating side, the temperature at the middle of the stack in the heating side were estimated to be 31.6, 38.5, and 45.8 °C, respectively. Figure 14 shows the temperature distributions along the thickness direction of the module. From the measurement data, ΔT_{drop} by each layer was estimated to be 4% of total temperature drop. The actual temperature ($T_{i,hot}$) on the hot side of i^{th} leg from the bottom of each module can be calculated as $T_{1,hot}–0.04\times i\times\Delta T$. By considering the temperature drop in the modules, theoretical V_{TE} as a function of ΔT was obtained as shown in the blue short-dash line of Fig. 5a. The small discrepancy may come from the misalignment of stacked legs in the modules during assembly.

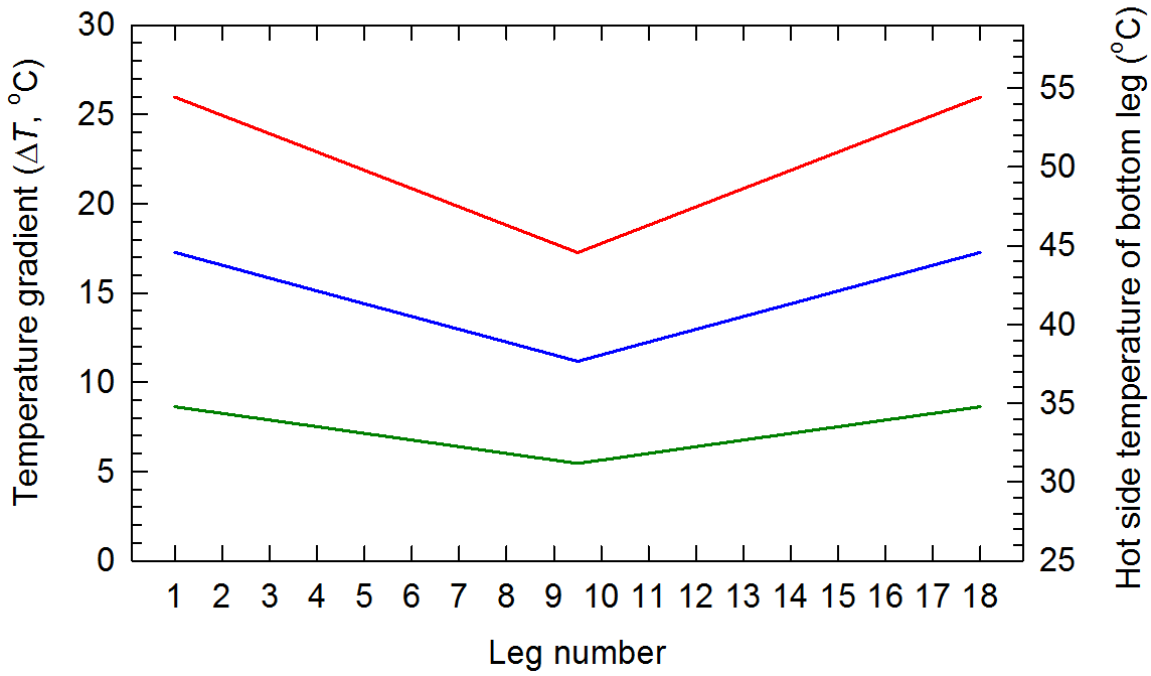

Figure 14. Heat transfer experimental results of a thermoelectric module at three heat conditions: the hot side temperature of the bottom leg was set to 35, 45, and 55 °C. The temperature at the top of the 18 film (module) was measured. The leg number was assigned from the bottom to the top, as shown in Fig. 4a of the main manuscript. Since there is no internal heating source in the leg, a linear temperature gradient is expected. Therefore, a half of the total temperature drop across 18 films is expected to occur at the mid plane of the stack. The temperature drops by each leg (film) at 35, 45, and 55 °C bottom temperatures are estimated to be 0.37, 0.72, and 1.02 °C, respectively (reprinted from [61]).

The temperature drop comes from the thermal resistance ($R_{thermal}$) of the module along the thickness direction, which can be estimated by using a series resistor model.

$$R_{thermal} = \sum_{i=1}^{N_l} \frac{1}{A}\left(\frac{t_{PTFE}}{k_{PTFE}} + \frac{t_{Al}}{k_{Al}} + \frac{t_{CNT}}{k_{CNT}} + R_{contact} \right)_i \tag{3.3}$$

where *A*, *t*, and *k* indicate the thickness, thermal conductivity, area of the indexed materials, respectively; $R_{contact}$ is thermal contact resistance between the films. In the bracket of Eq. (3), the thermal contact resistance mainly due to air trapped between the layers. Among the first three terms, thermal resistance from PTFE is dominant due to relatively thick layer (~220 μm), compared to Al (~20 μm) and CNT (8 μm). Assuming thermal conductivity of PTFE is ~0.25 W/m-K [78], the first term in the bracket of Eq. (3) is estimated to be ~9×10^{-4} m^2K/W, which is comparable to typical thermal contact resistances between metallic interfaces under vacuum (i.e., poor thermal contact) [79]. This suggests that further optimized devices may yield a higher output voltage.

The output voltage of 150 mV from the thermoelectric device was selected for operating a glucose sensor based on the testing results of the sensor unit with a power supply. It was found that the electrochromic sensor worked properly with an input voltage of ~100 mV or higher. Therefore, we set our operation voltage slightly higher than 100 mV. In order to maximize power output at an output voltage of 150 mV, an open circuit voltage (OCV) of 300 mV was chosen since the maximum power is obtained at a half of OCV. According to Figure 13(a), it is necessary to have a temperature gradient of 32 K. The output current and power with a temperature gradient of 32 K were measured, showing 1.8 μW at the matching 150 mV in Figure 13(b). This power output is orders of magnitude larger than those of other organic thermoelectrics [13, 39], which could be utilized for operating wireless communication devices. For instance, a TE powered sensor can send ~103 bits (125 bytes ~ 125 text characters) of

information per every 10 sec wirelessly by accumulating 1 μW energy to a capacitor [80].

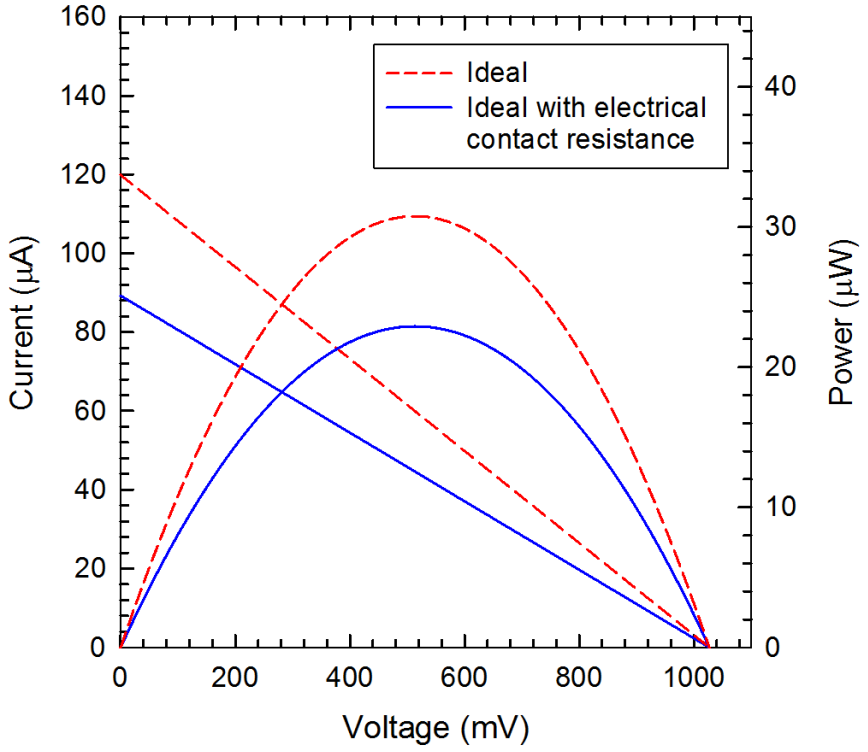

Figure 15. Assuming that ΔT=100 K, thermoelectric voltage (open-circuit) can be reached to 1 volt. When a device is free of electrical contact resistance, no defects in the legs, and perfect assembly (internal resistance is 8.6 kΩ), a large power output up to 31 μW can be obtained, as indicated by the dash lines (called "ideal" in the legend). On the other hand, the power output was calculated to be 23 μW at ΔT=100 K when the actual internal resistance was used (the same as measured value: 11.5 kΩ) (reprinted from [61]).

We also estimated the maximum power output can be 3.1 μW when the device is free of electrical contact resistance, misalignment, and defects with a temperature

gradient of 32 K, as shown in the purple log-dash line of Figure 13(b). The ideal device resistance from 72 p-n pairs was calculated to be 8.6 kΩ in comparison to 11.5 kΩ from our actual device for testing as the resistances of an individual p- and n-type leg were measured to be 38 Ω and 81 Ω, respectively. If we assume the temperature gradient is higher (100 K) with the ideal device, the maximum output power could be as high as 31 μW (Figure 15).

3.3.6 Demonstration of flexible thermoelectric device

The thermoelectric device was tested for operating a glucose sensor so as to demonstrate that the power generation from our device is practically viable. The internal impedance of the sensor was designed to be close to the matching load resistance for an operation at the maximum power output. The glucose sensor consists of transparent electrodes, a Nafion membrane, and a paper, as shown in Figure 16(a). The transparent electrodes were made of carbon nanotubes stabilized by poly(3,4-ethylenedioxythiophene):poly(styrenesulfonate) (PEDOT:PSS). On the electrode, we deposited electrochromic Prussian blue (PB), which reversibly changes color upon reaction only with a supply of current. Figure 16(b) illustrates the operation of the glucose sensor and Figure 16(c) shows a prototype by integrating the thermoelectric device. When a drop (~50 μL) of glucose solution containing 0.20 mM glucose is soaked by the paper, where $K_3Fe(CN)_6$ is loaded, due to a capillary action, $K_4Fe(CN)_6$ is produced without changing color before (Figure 16(d)) and after (Figure 16(e)) the glucose injection. Upon applying an electrical potential, potassium ions and electrons

coming from oxidation of $K_4[Fe(CN)_6]_3$ turns $Fe(III)_4[Fe(II)(CN)_6]_3$(PB) into Prussian white (PW), $K_4Fe(II)_4[Fe(II)(CN)_6]_3$ [81], as shown in Figure 16(f). After disconnecting the thermoelectric power source, PW returned to PB as shown in Figure 16(g).

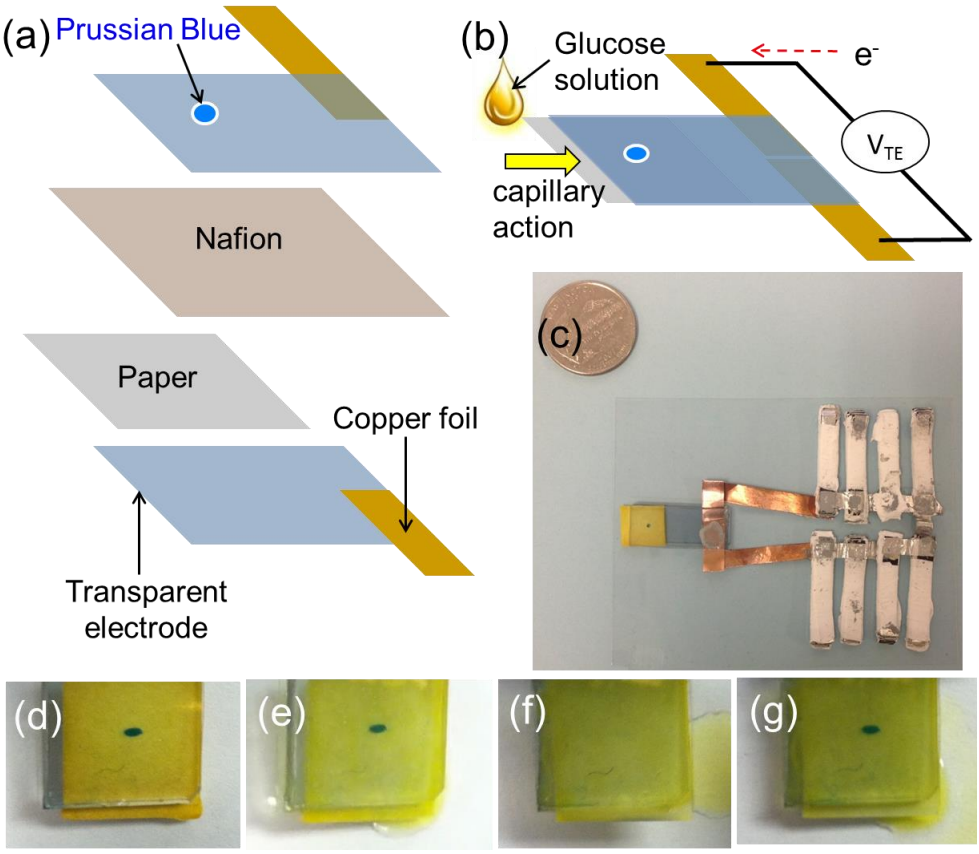

Figure 16. (a) Exploded view schematic of a glucose sensor with Prussian blue display. (b) Operation schematic of the glucose sensor with a thermoelectric device. (c) Prototype of glucose detection sensor integrated with a thermoelectric device. PB display of glucose sensor before (d) and after (e) injection of 50 μL of solution containing 0.2 mM glucose without supplying power. When power (150 mV) was supplied by the thermoelectric device, the PB disappeared after 180s due to the change into PW (f). The PW changed back to blue after stop supplying power (g) (reprinted from [61]).

3.4 Conclusions

CNTs were functionalized to p- or n-type materials, and a TE device made of CNT films was designed and fabricated to operate a glucose sensor. The electronic transport properties were controlled by adjusting the amount of coating on CNTs for p-type films as well as reducing CNTs with multiple agents, PEI, DETA, and $NaBH_4$ for n-type. By optimizing the mixing ratio of PEI to DETA (67:33 wt%), n-type thermopower values as large as -86 μV/K at 5,200 S/m were obtained due to synergistic effects from both large and small dopant molecules. According to Kelvin probe measurement results, the Fermi level of the p-type samples (-4.91 eV) were changed to -4.69 eV after PEI/DETA reduction and -4.61 eV after additional $NaBH_4$ reduction, clearly indicating n-type conversion after the doping processes. CV and UV-vis-IR measurement results suggest that the HOMO and LUMO energy levels are respectively located at -5.05 and -4.59 eV. Compared to free hole carrier mobility (0.365 cm^2/V-s), the n-type CNT films showed a lower electron mobility (0.206 cm^2/V-s) presumably due to the electrically insulating PEI/DETA that deter the carrier transport across the junctions between CNTs. The high free carrier concentrations (1.86×10^{21} cm^{-3} for p-type and 1.25×10^{21} cm^{-3} for n-type) suggest that it is necessary to further increase the carrier mobility to obtain higher electrical conductivity.

The thermoelectric device was made of 72 p-type and 72 n-type CNT films electrically connected in series and thermally in parallel so as to maximally utilize temperature gradients. This device produced 465 mV at a temperature gradient of 49 K, which is much larger than those of other polymer based composites. The TE device was

integrated with a glucose sensor and the self-powered sensor system was operated at a matching voltage of ~150 mV by a temperature gradient of 32 K. The power output was measured to be as high as 1.8 μW, which is practically viable for operating sensor units equipped with wireless communication and power management circuits. Further work may result in self-powered sensor systems for a wide range of applications including wearable electronics operated by body heat.

CHAPTER IV

THERMALLY CHARGEABLE SOLID-STATE SUPERCAPACITOR*

4.1 Introduction

Low-grade waste heat is projected to be one of the most sustainable, clean, and promising energy sources [15]. In particular, rapid development of wearable and flexible electronics prompted researchers to be interested in harvesting dissipated heat from the human body or power consuming devices. The well-known thermal-to-electrical energy conversion utilizes the Seebeck effect [13-14, 16-17], but this can be also achieved using thermally-driven ion diffusion [20, 23, 44, 82] or temperature-dependent electrochemical redox potential [18, 22, 83].

While conventional thermoelectric devices based on electron diffusion by temperature gradient (Seebeck effect) is attractive because of their unique advantages such as simple solid-state structures without moving parts, low output voltage originating from intrinsically small Seebeck coefficients (typically on the order of 1~100 μV/K) has limited their usage in practice. Higher output voltage (~1.4 mV/K) can be obtained using the temperature dependent electrochemical redox potential [18, 22], but liquid electrolytes in thermogalvanic cells necessitate bulky packaging to prevent leakage as well as make it difficult to sustain temperature gradients, which are not favorable to wearable and portable applications.

---

* Reprinted with permission from S. L. Kim, H. T. Lin, C. Yu, Thermally chargeable solid-state supercapacitor, Advanced Energy Materials, 6, 1600546, Copyright 2016 by John Wiley & Sons, Inc.

Differing from these effects, the Soret effect establishes a difference in molecule/ion concentrations within a mixture as a result of molecule/ion migration driven by a temperature gradient, and thus research related to transport behaviors has been mostly focused on gas and liquid phases [44, 82]. Nevertheless, convection of fluid makes it hard to maintain the temperature gradient, which have typically resulted in a negligibly small output voltage in practice [18, 22]. Here our novel approach employed a solid-state ionic conductor to easily maintain the temperature gradient so as to fully utilize the Soret effect for wearable and portable applications. Furthermore, the output voltage produced by the Soret effect was further electrochemically stored in integrated redox electrodes like a supercapacitor. Energy storing unit is important since small electrical power/energy from this type of energy harvesting devices need to be accumulated for practical use. Here our integrated energy storing harvester can be used as a stand-alone device that can be charged simply imposing temperature gradients.

4.2 Experimental

4.2.1 Material synthesis

CNTs (P2-SWNT) were purchased from Carbon solutions, Inc. and porous graphene powders were synthesized by CO_2 conversion method [84]. To obtain the graphene powders, Mg powder (1.5 g) mixed with Zn powder (6 g) was reacted under 70 cm^3/min of CO2 at 680 °C for 60 min in a tube furnace (22-mm inner diameter tube). Then, the reacted powders were stirred in 2-M HCl for 24 hr to remove MgO and ZnO, and subsequently vigorously washed with Di-water and then dried at room temperature

overnight. CNT (5 mg) and GP (10 mg) were dispersed in deionized (DI) water (20 mL) with SDBS (60 mg) (88%, Acros Organics) to prepare a G/CNT solution by sonication with a probe sonicator (100 W, XL2000, Misonix Micron) for 2 hr. The G/CNT electrode was fabricated by vacuum-filtrating the G/CNT solution onto a polytetrafluoroethylene (PTFE) membrane (0.45-μm pore diameter, Tisch Scientific) with additional DI water, and subsequently the film was dried in air at 50 °C. The CNT-only film was prepared using the procedure for synthesizing the G/CNT electrode with only 15-mg CNT (no graphene). PANI was deposited by oxidation of aniline (0.1 M in 1-M HCl) with a constant-current method (2 mA/cm^2) in a conventional three-electrode system [85].

The solid PSSH film was prepared by drop-casting a PSSH solution (18 wt%, Sigma-Aldrich) on the PTFE plate and then drying at room temperature for 24 hr. The film thickness was controlled by adjusting the PSSH concentration in the solution. To fabricate solid-state supercapacitor, two P-G/CNT electrodes were immersed in the PSSH solution for 10 min, and then assembled with the PSSH film. The as-synthesized device was left at room temperature for 12 hr prior to operation.

4.2.2 Electrical property measurements

For the electrical property measurements along the in-plane direction, a PSSH solution (4 wt%) was drop-casted on glass slides (7~8 mm in width and 25 mm in length) whose two ends were coated by CNT or gold films (electrodes for the measurements) prior to the deposition of the PSSH. The deposited PSSH solution was

dried at room temperature for 24 hr. Typical sample thickness was measured to be 17~21 μm. The samples were suspended (along the long edge direction) between two thermoelectric devices that were serially connected to a DC power supply (Figure 17(a)). One thermoelectric device was cooled while the other was heated, and vice versa. Temperature sweeping between +2.5 K and -2.5 K for each thermoelectric device was carried out to create various temperature differences between -5 and +5 K as well as ensure no hysteresis (Figure 18). For temperature and voltage measurements, T-type thermocouples consisting of copper and constantan wires were mounted on the CNT or gold electrodes. Thermally induced voltage was measured using the copper wire, and temperature was measured with the copper-constantan wire couple (T-type thermocouple). This configuration is to ensure the locations for the temperature and voltage measurements identical. Two additional electrical contacts at both ends of the samples were also made to measure 4-probe electrical resistance.

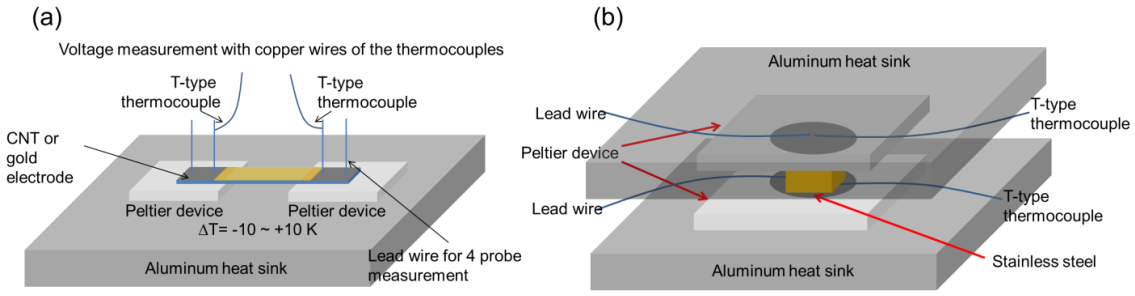

Figure 17. Schematic of the setups for measuring electrical conductivity and thermopower along (a) the in-plane direction and (b) out-of-plane direction (reprinted from [86]).

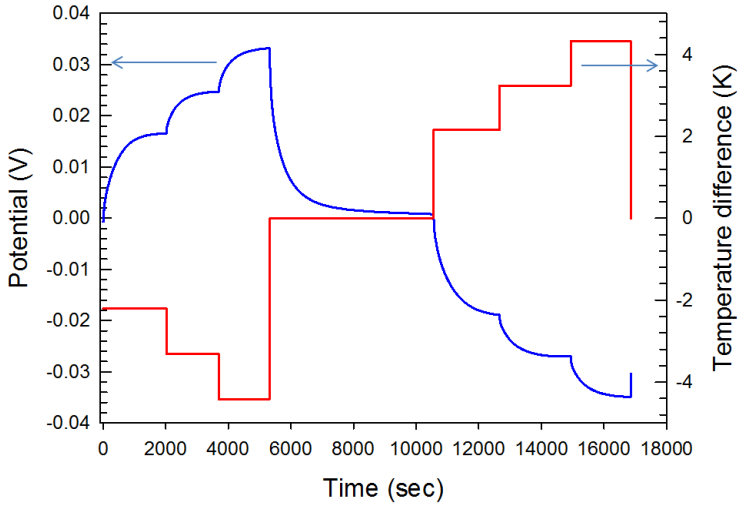

Figure 18. Real-time thermopower measurement results of PSSH at RH 70%. Thermo-induced voltage and temperature difference data were taken at steady-state condition (reprinted from [86]).

Prior to making temperature gradients, linear current-voltage relations were obtained from the 4-probe measurements, confirming Ohmic contacts. Upon creating 6-8 different temperature gradients across the sample, thermally induced voltage values were recorded and then linear slopes were found to obtain thermopower.

For out-of-plane electrical property measurements, PSSH films were prepared by drop-casting a PSSH solution (typically 4~18 wt%). Then CNT-only films were assembled with the PSSH films. All samples had the same active area (0.7 cm ×0.7 cm). For thermopower measurements, we used thick PSSH (~2 mm) to have larger temperature difference considering the physical interference by the thermocouples. The Peltier devices were placed on the top and bottom of the sample (Figure 17(b)) to create temperature gradients along the vertical direction.

The out-of-plane electrical conductivity of the PSSH film was obtained using electrochemical impedance spectroscopy (EIS) shown in Figure 19(a) (Nyquist plot). The intercept of the Nyquist curve on the real axis represents mainly the internal/contact impedance associated with the electrodes and the Ohmic impedance of the electrolyte. To extract the electrolyte impedance, we plotted all impedance values with respect to the thickness of the PSSH films (Figure 19(b)). By eliminating the internal/contact impedance, out-of-plane electrical conductivity (σ_{PSSH}) of the PSSH film was obtained using the following relation:

$$\sigma_{PSSH} = \frac{t}{R_{PSSH} A} \tag{4.1}$$

where R_{PSSH} is the Ohmic impedance of the PSSH film; A is the contact area between the PSSH film and the CNT electrodes; and t is the film thickness.

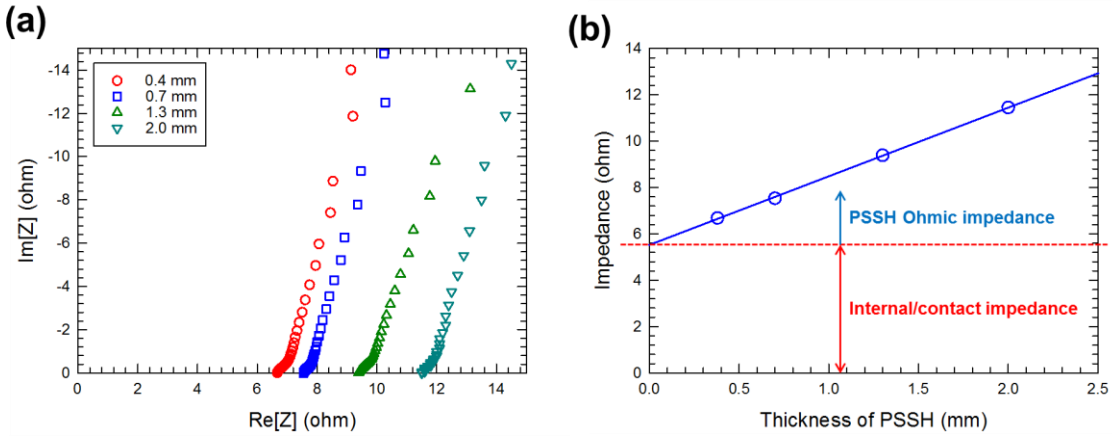

Figure 19. Electrochemical measurement of PSSH films whose thicknesses are 0.4, 0.7, 1.3, and 2.0 mm. (a) EIS measurements (Nyquist plots). (b) Impedance of the PSSH films as a function of PSSH thickness (reprinted from [86]).

4.2.3 Controlled environment chamber

The electrical transport property measurements were carried out as a function of RH at 22 °C in a custom-built humidity chamber [87]. We used a custom-built chamber schematically shown in Figure 20 to readily change the environment condition. The RH of the chamber was controlled using a humidifier containing glycerol and de-ionized water [87-88]. RH was controlled by changing the ratio of de-ionized water volume to glycerol volume in the mixture solution based on the following equation [87-88]:

$$\frac{V_{water}}{V_{glycerol}} = 1.26\left[\frac{1}{3.83\left(\left(19.9-0.189RH\right)^{0.0806}-1\right)}-1\right] \tag{4.2}$$

where V_{water} and $V_{glycerol}$ are the volume of de-ionized water and glycerol; and RH is the targeted RH.

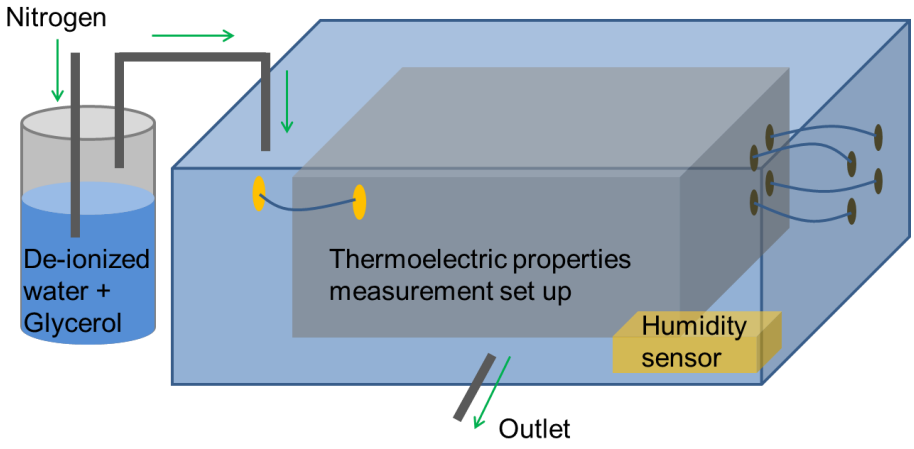

Figure 20. Schematic diagram of the relative humidity controlled-environment chamber (reprinted from [86]).

All measurements were conducted 2 hours after the chamber reached targeted RH values to ensure steady-state conditions prior to testing. All thermopower and electrical conductivity measurements were conducted in inert environment by flowing nitrogen gas. We also used oxygen gas instead of nitrogen to confirm our measurement results, and noticeable differences were not observed.

4.2.4 Thermal conductivity measurement

Out-of-plane thermal conductivity was measured by following the ASTM D5470 steady-state method at room temperature (RH 65~70%), as depicted in Figure 21(a). To eliminate thermal contact resistance between the sample and the rod, multiple samples with different thicknesses will be prepared. Thermal contact resistance will be obtained from the y-intercept point, as illustrated in Figure 21(b).

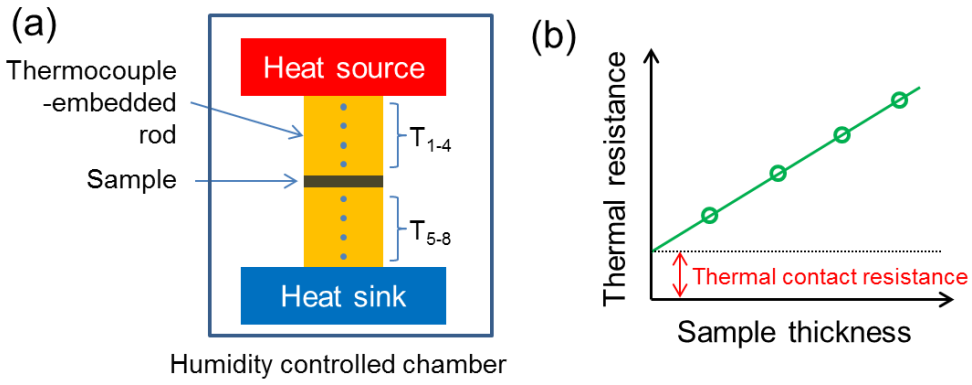

Figure 21. (a) Schematic of a steady-state thermal conductivity measurement setup in a humidity controlled chamber. (b) To extract thermal contact resistance from the data obtained from ASTM D5470-06 measurements, thermal resistance as a function of thickness of the sample will be obtained from the y-intercept.

4.2.5 Characterization

The surface and cross section of the electrodes were inspected by using a field-emission scanning electron microscope (FEI Quanta 600). The electrochemical measurements were all performed at room temperature using a CHI 604D electrochemical analyzer and Arbin BT2000. The electrochemical performance of P-G/CNT electrodes (0.7 cm × 1.4 cm) in a 1-M H_2SO_4 aqueous solution was obtained using a 3-electrode setup with a configuration of P-G/CNT as a working electrode, Ag/AgCl as a reference electrode, and a Pt foil as a counter electrode. TCSC with an active area of ~0.49 cm^2 was tested under RH 70% at 22 °C.

4.3 Results and discussion

4.3.1 Working principle of thermally chargeable supercapacitor (TCSC)

Our TCSC employed PSSH as both solid electrolyte and voltage generator and two PANI-deposited G/CNT (P-G/CNT) films to sandwich the PSSH as positive and negative electrodes (Figure 22(a)). At the beginning, TCSC has uniformly distributed ions at a discharged state (Figure 22(a)). When heat (thermal energy) is applied to one of the electrodes, the temperature gradient between two electrodes causes more mobile H^+ to diffuse to the cold side (Soret effect), leaving less mobile PSS^- behind (Figure 1b). As a consequence, H^+ concentration near the cold electrode increases while H^+ concentration near the hot electrode decreases. This concentration difference creates potential difference between two electrodes, which can be described using the Nernst equation [89]:

$$E_{cell} = E^{\circ}_{cell} - \frac{RT}{F} \ln \frac{[H^{+}_{hot}]}{[H^{+}_{cold}]} \tag{4.3}$$

where E_{cell} is the potential difference between cold and hot electrode; $E°_{cell}$ is the standard cell potential from the two electrodes; $[H^{+}_{hot}]$ and $[H^{+}_{cold}]$ are the molar concentration near the hot and cold electrode, respectively; R is the universal gas constant; T is the temperature; and F is the Faraday constant.

The change of H^{+} concentration electrochemically causes the potential of the cold electrode to be higher than that of the hot electrode. When the electrodes are externally connected, electron flow due to the potential difference leads to oxidation (emeraldine salt) and reduction (leucoemeraldine base) of PANI at the hot and cold electrodes, respectively (Figure 22(c) and 22(f)) [90]. It is also possible that emeraldine salt is reduced to leucoemeraldine salt by accepting additional protons [91]. In this case, consumed H^{+} at the cold electrode will be replenished by H^{+} released from oxidation reactions at the hot electrode so that thermally-driven H^{+} concentration differences is maintained. This process represents “charging” of TCSC, and the charging continues until the transferred electrons balances H^{+} at the cold side. Depending on the load resistance, this charging stage can be directly used for useful work or the charging speed can be controlled. After removing the temperature gradient, H^{+} at the cold side moves back to a randomly distributed state (Figure 22(d)), but the electrochemical energy remains in a form of different redox potentials at the electrodes, which is a “charged” state of TCSC (Figure 22(e)).

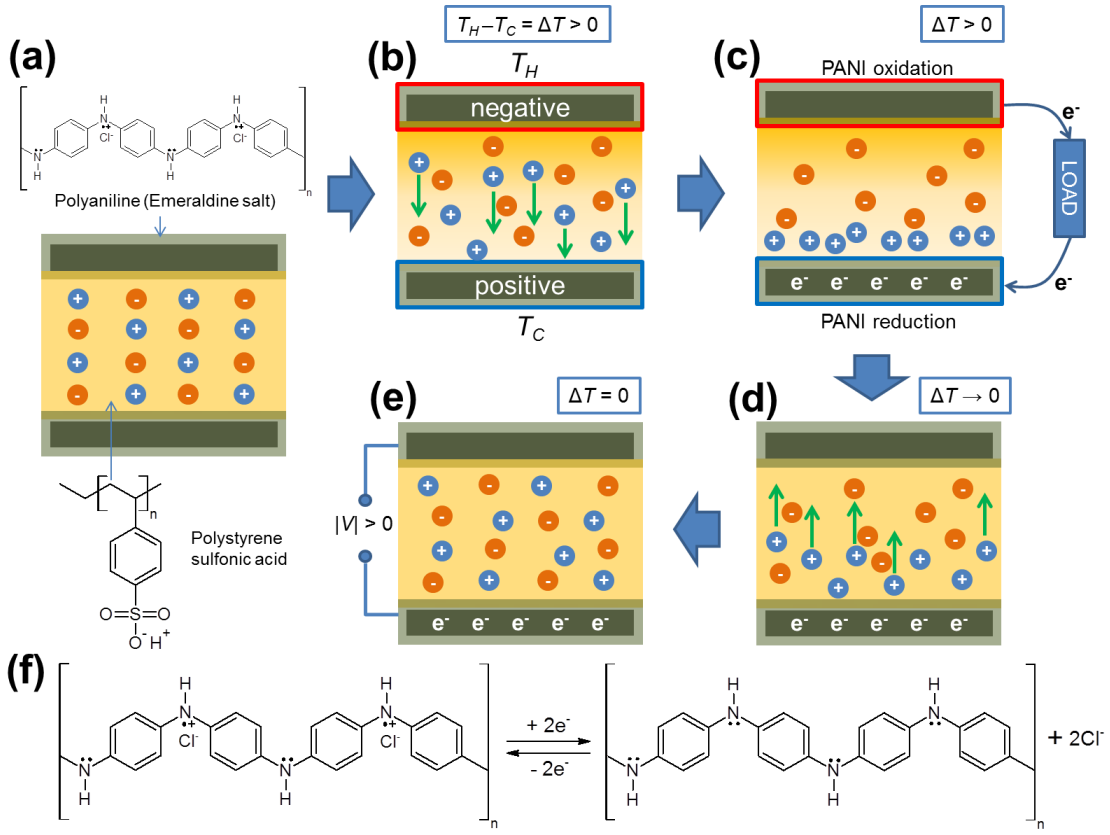

Figure 22. Working mechanism of thermally chargeable supercapacitor. (a) Schematic of TCSC in discharged (or initial) state with PSSH as an electrolyte and P-G/CNT as electrodes. (b) When a temperature gradient is made between two electrodes, the protons at the hot electrode will migrate to the cold electrode by the Soret effect. (c) Thermodiffusion of protons leads to electrochemical reactions at the two electrodes when electrons are transferred from the hot side to the cold side by connecting the two electrodes with a load resistor. (d) When the temperature gradient is removed and the load resistor is disengaged, the protons are randomly distributed. (e) Despite the ion movement, the charges on the bottom electrode remain, completing a charged state of the supercapacitor without a temperature difference. (f) Redox reactions of PANI during the charging and discharging processes. PANI switches between emeraldine salt and leucoemeraldine base by accepting and releasing electrons during the reduction and oxidation process, respectively (reprinted from [86]).

4.3.2 Thermoelectric properties of PSSH

To evaluate the thermally charging and energy storage performance of TCSC, electrical transport properties of PSSH and electrochemical performance of the electrodes were characterized. First, thermopower and electrical conductivity of PSSH were measured over a wide relative humidity (RH) range from 30% to 70% due to the hygroscopic nature of PSSH (Figure 23(a)). At 70% RH condition, the thermopower of PSSH film was measured to be ~7.9 mV/K, which is much higher than the reported Seebeck coefficient from conventional thermoelectric materials and thermo-electrochemical cells. In lower humidity levels, the thermopower of PSSH decreased to ~6.3 mV/K (50% RH) and ~5.1 mV/K (30% RH). The exceptionally high thermopower of PSSH can be attributed to mobile proton and immobile (or less mobile) anion due to the large difference in their molecular weights, which prevents the potential produced by thermos-diffusion of mobile ions from being suppressed by movement of counter ions.

The electrical conductivity of PSSH at 70% RH was around 9 S/m, which is within the range of PSSH-based membrane [92] and higher than other solid electrolytes such as polyvinyl alcohol gel [93-94]. The large reduction of the electrical conductivity at lower RH levels is likely to come from a lower concentration and mobility of protons since water promotes dissociation of proton from the sulfonic group and higher RH may allow water to form more percolated pathways for protons. It should be noted that thermopower and electrical conductivity were measured along both in-plane and out-of-plane directions. These values matched, confirming the isotropic characteristics of our PSSH film.

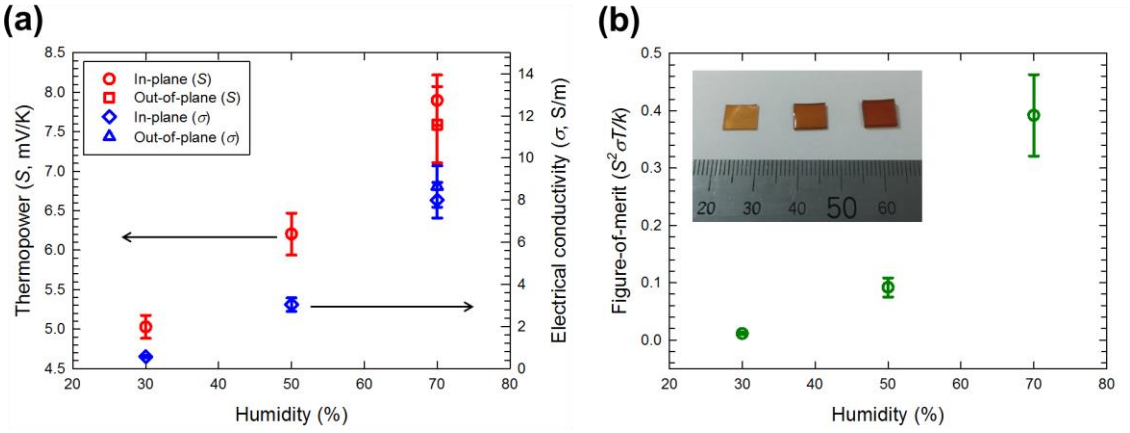

Figure 23. Electrical transport properties and figure-of-merit of PSSH. (a) Thermopower and electrical conductivity of PSSH films along the in-plane and out-of-plane directions. (b) Figure-of-merit of PSSH films along the out-of-plane direction. The inset shows three PSSH films with different thicknesses (reprinted from [86]).

The thermal conductivity of PSSH film was measured to be 0.38 ± 0.05 W/m-K along the out-of-plane direction at room temperature and 65~70% RH. It should be noted that our thermal conductivity measurement technique was verified by characterizing a commercial Nafion membrane (Figure 24). To verify our thermal conductivity measurement results for polystyrene sulfonic acid (PSSH) at relative humidity (RH) 65~70%, we measured thermal conductivity of Nafion film at the same humidity level, which has been well-studied previously [95-96]. In our measurement, the thermal conductivity of Nafion was measured to be 0.23 ± 0.03 W/m-K at RH 65~70%, which were plotted together with literature values measured using the ASTM D5470 method, as shown in Figure 24. Our measured values fall between RH 50% and RH 80% results, confirming that our thermal conductivity measurement at RH 65~70% condition is reliable.

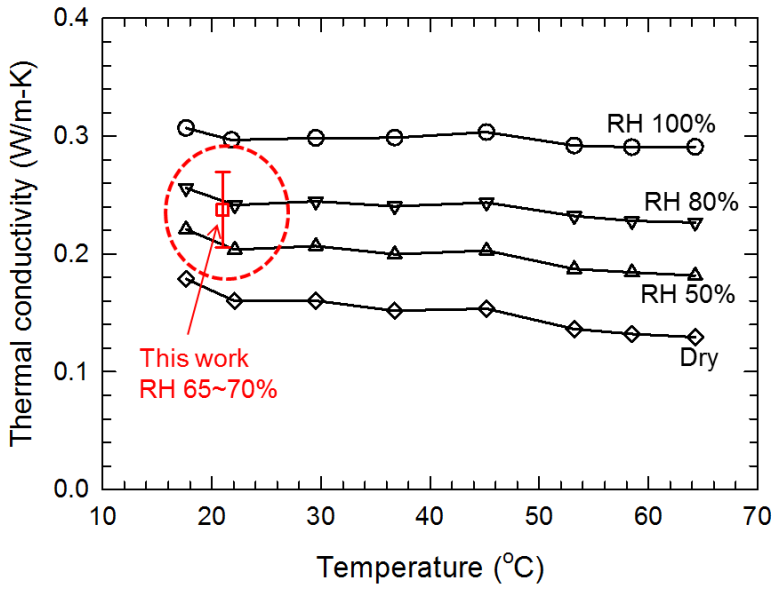

Figure 24. Comparison of the thermal conductivity of Nafion film at different humidity levels. Diamond (◊), circle (○), upward triangle (Δ), and downward triangle (∇) represent the measured values in literature. Square (□) represents our measurement values (reprinted from [86]).

We further calculated a figure-of-merit ($S^2\sigma T/k$) in the same way that conventional thermoelectric materials are evaluated, where S, σ, T, and k are thermopower, electrical conductivity, absolute temperature, and thermal conductivity, respectively. The maximum figure-of-merit at room temperature was found to be remarkably high up to ~0.4 at 70% RH (Figure 23(b)).

4.3.3 Fabrication and electrochemical test of redox electrodes

The electrode was fabricated by depositing PANI into the G/CNT film, so we intentionally made the film highly porous using flower-shape porous graphene structures entangled by tubular CNTs. This binder-free electrode (Figure 25(b) and (c)) was much

more porous than a CNT-only film (Figure 25(a)) prepared for comparison. The specific capacitance of the porous G/CNT showed almost 3 times higher (150 F/g) than the CNT-only (52 F/g) at 0.5 A/g (Figure 25(g)), presumably owing to the larger accessible surface area in G/CNT.

To further increase the capacitance with redox reactions, PANI was electro-deposited on G/CNT for 10 min (Figure 25(d)), 20 min (Figure 25(e)), and 30 min (Figure 25(f)). As shown in Figure 25(g), the specific capacitance for 10, 20, and 30-min PANI deposition was remarkably increased to 370, 430, and 410 F/g at a current density of 0.5 A/g, respectively. The lower specific capacitance from the 30-min PANI deposition compared to that of the 20-min could be attributed to the reduction of porosity (compare Figure 25(e) and 25(f)). The semi-symmetric galvanostatic charge–discharge (GCD) curves at charging/discharging and semi-linear voltage-time relation for CNT-only, G/CNT, and P-G/CNT at 1 A/g in a potential window of 0~0.8 V (Figure 25(h)) suggest excellent Coulombic efficiency and stable capacitance.

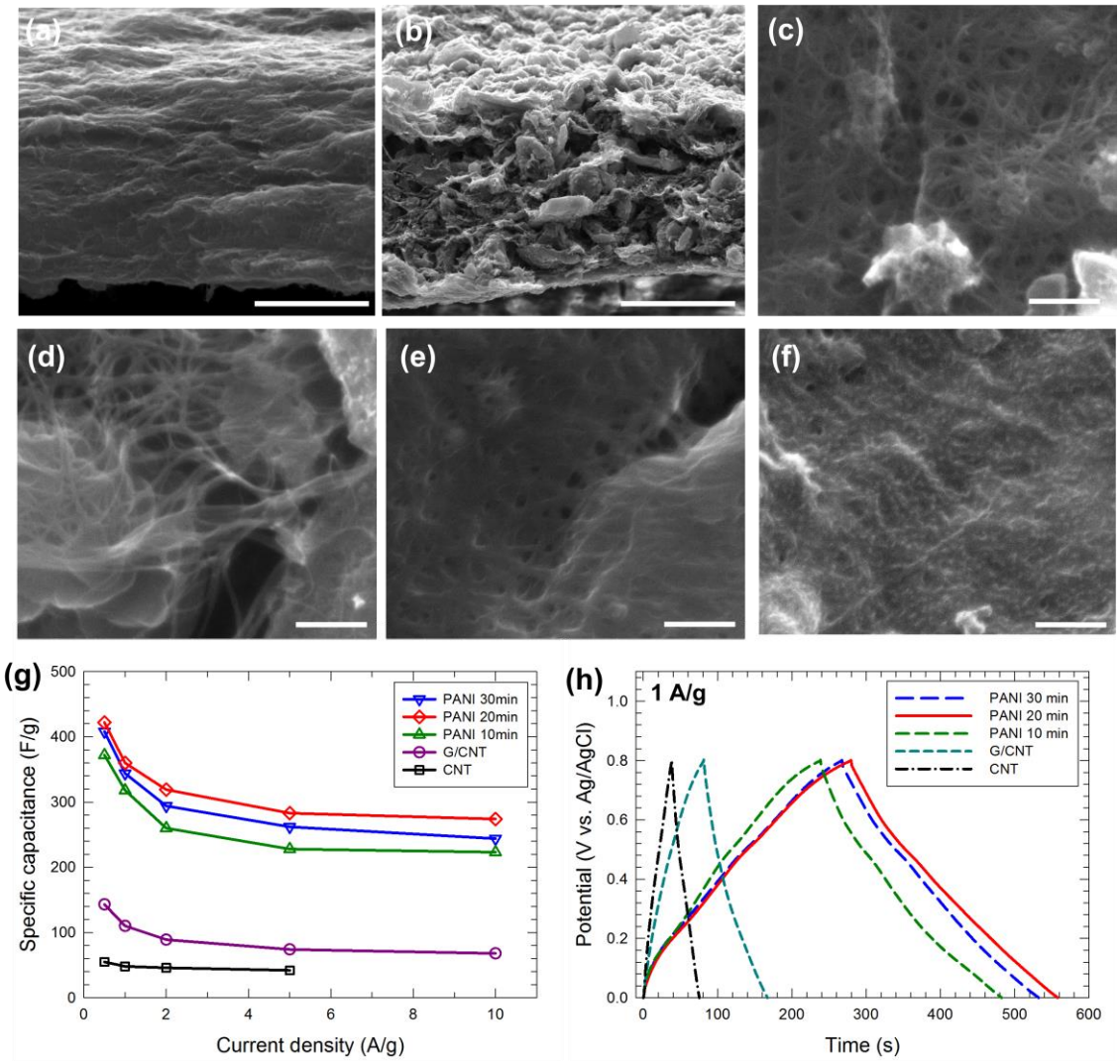

Figure 25. Morphologies and electrochemical performances of G/CNT electrodes with different PANI deposition time periods. (a)-(b) Cold-fractured cross sections of a CNT film (scale bar: 4 μm) and a G/CNT film (scale bar: 20 μm). (c)-(f) The surface of a G/CNT film with 0-, 10-, 20-, and 30-min PANI deposition respectively for (c), (d), (e), and (f). All scale bars indicate 500 nm. (g) Specific capacitance of the electrodes versus discharge current density. (h) Galvanostatic charge–discharge curves as a function of time at 1 A per gram of the active materials in the electrodes (reprinted from [86]).

4.3.4 Fabrication and electrochemical test of TCSC device

Based on the electrodes performance test, 20 min PANI electrode was chosen as the best P-G/CNT electrodes for solid-state TCSC device. Figure 26 shows the fabrication process of solid-state TCSC. After assembly, the thin film type TCSC device showed good flexibility and light-weight.

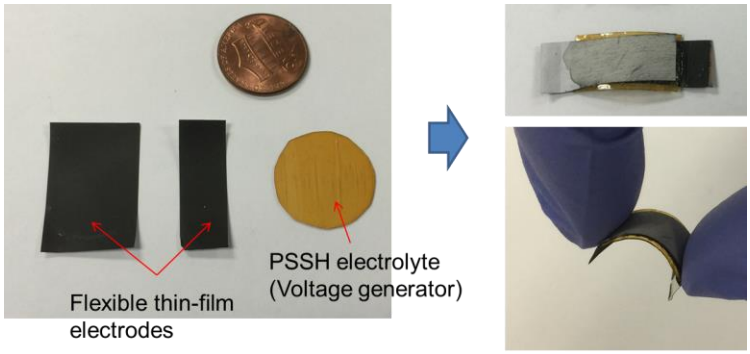

Figure 26. Fabrication process of solid-state TCSC

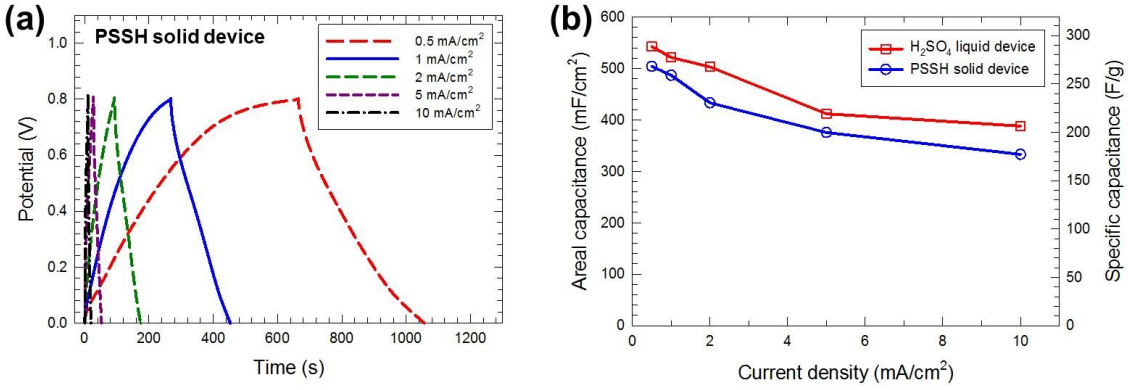

Figure 27. Electrochemical performance of TCSC when electrically charged and discharged. (a) Galvanostatic charge-discharge curves. (b) Areal capacitances of a P-G/CNT (20 min) electrode with a PSSH solid electrolyte (thickness: 380 µm, RH 70% at 22 °C) and 1-M H_2SO_4 aqueous electrolyte (reprinted from [86]).

After the assembly, charging/discharging characteristics of solid-state supercapacitor were evaluated using a galvanostat (not thermally charged here). The semi-symmetric semi-linear GCD profiles indicate excellent capacitive characteristics (Figure 27(a)), and rectangular-shape cyclic voltammetry (CV) scan results also show an ideal capacitive behavior (Figure 28(b)). At a current density of 0.5 mA/cm^2, the supercapacitor exhibited the highest areal capacitance of ~500 mF/cm^2 (Figure 27(b)), which is very high among reported literature values [97-101]. It is worth noting that areal capacitance rather than mass-based specific capacitance is more important to consider in wearable applications for light and thin fully-organic devices.

It is also striking that the completely solid-state supercapacitor shows an electrochemical performance (e.g., 487 mF/cm^2 at 1.0 mA/cm^2) comparable to 512 mF/cm^2 of liquid-type supercapacitor assembled with a 1-M H_2SO_4 aqueous solution. Typical solid-state supercapacitors suffer from large inaccessible surface areas in porous electrodes unlike conventional supercapacitors with liquid electrolytes, but our electrode was soaked in liquid-phase PSSH during the integration process to fully coat the tortuous electrode surface, as indicated by the comparable internal impedance in the Nyquist plots from PSSH and aqueous H_2SO_4 based supercapacitors (Figure 28(c)).

A liquid-type supercapacitor was fabricated using a similar procedure reported in literature [102]. Firstly, two pieces of PANI deposited graphene and carbon nanotube (P-G/CNT) electrode were attached to two different glass slides. After a separator (Whatman filter paper-Grade 1) was inserted between the two electrodes, the three

pieces were secured using Parafilm and then dipped in a 1-M H_2SO_4 aqueous electrolyte. The active area overlapped by both P-G/CNT electrodes was 0.49 cm^2 (0.7 cm ×0.7 cm).

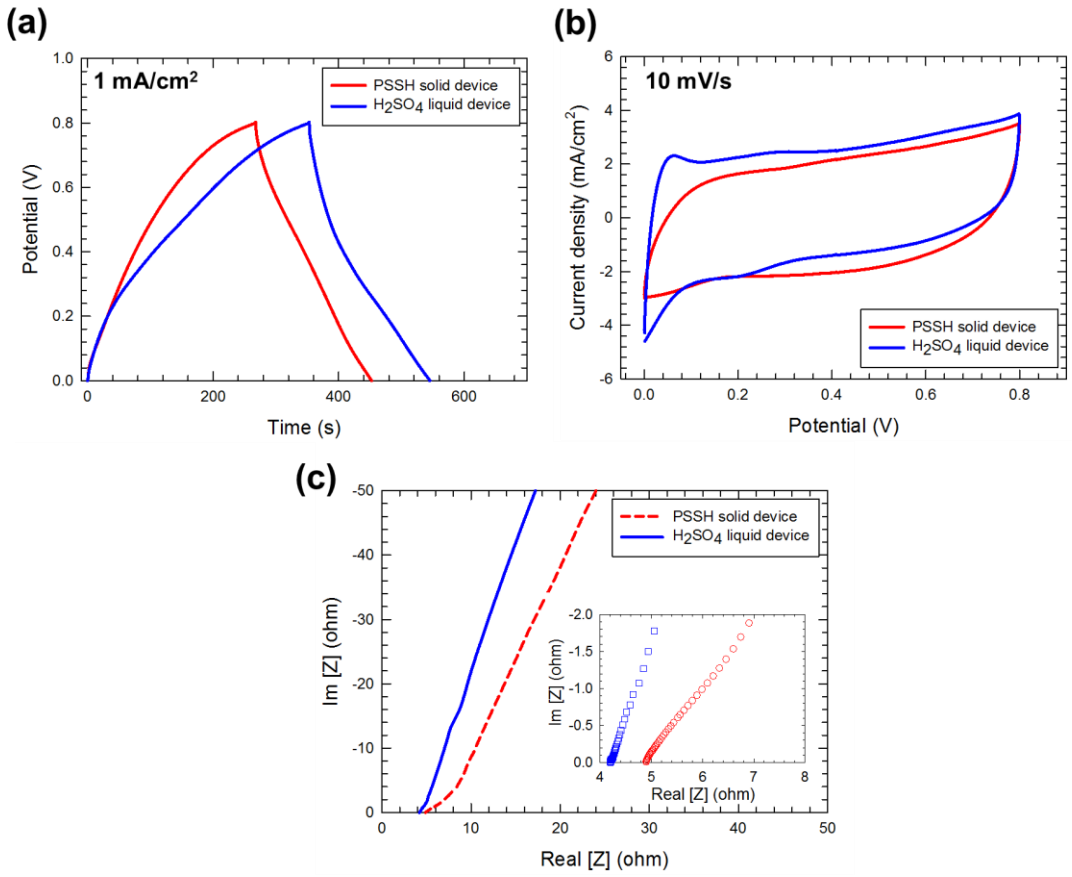

Figure 28. Comparison of electrochemical performances of the solid-state device with PSSH electrolyte and liquid-type device with 1-M H_2SO_4 aqueous electrolyte (a) GCD curves at 1 mA/cm^2. (b) CV scans comparison at a scan rate of 10 mV/s. (c) Nyquist plot for different devices. Inset shows the magnification view for high frequency range (reprinted from [86]).

As shown in galvanostatic charge-discharge (GCD) curves (Figure 28(a)), both of the solid-state device and the liquid-type device showed the semi-linear profile of charge and discharge curves, indicating the stable capacitive performances over the operating range (0~0.8 V).

Cyclic voltammetry (CV) measurements at a scan rate of 10 mV/s (Figure 28(b)) showed that our solid-state supercapacitor has almost the same CV curve and similar capacitance with the liquid-type supercapacitor. In addition, the semi-symmetrical rectangular shapes in the CV curves indicate ideal capacitive performances.

The vertical straight lines in the Nyquist plots (Figure 28(c)) also suggest an ideal capacitive behavior. The intercept of the Nyquist curve on the real axis indicates internal/contact impedance of electrode and Ohmic impedance of electrolyte. The liquid-type device showed 4.1 Ω, which is smaller than 5 Ω from the solid-state device. This difference is mainly due to the higher ionic conductivity of the 1-M H_2SO_4 aqueous electrolyte than that of the solid-state PSSH electrolyte. However, in the high frequency range of the both plots, the negligible high-frequency resistor-capacitor loop (or semi-circle) indicated very low interfacial charge transfer impedance, resulting in facile charge transfer between electrolyte and electrode.

Our supercapcitor is also stable, showing only 6% decay in specific capacitance after 1000 cycles and maintaining long-term stability even after 5000 charge-discharge cycles at 5 mA/cm^2 with ~100% Coulombic efficiency (Figure 29(a)). Our P-G/CNT electrode has superior energy density (5.7 mWh/g) and power density (2.1 W/g)

compared to those of conventional supercapacitors [103-107], as shown in the Ragone plot (Figure 29(b)).

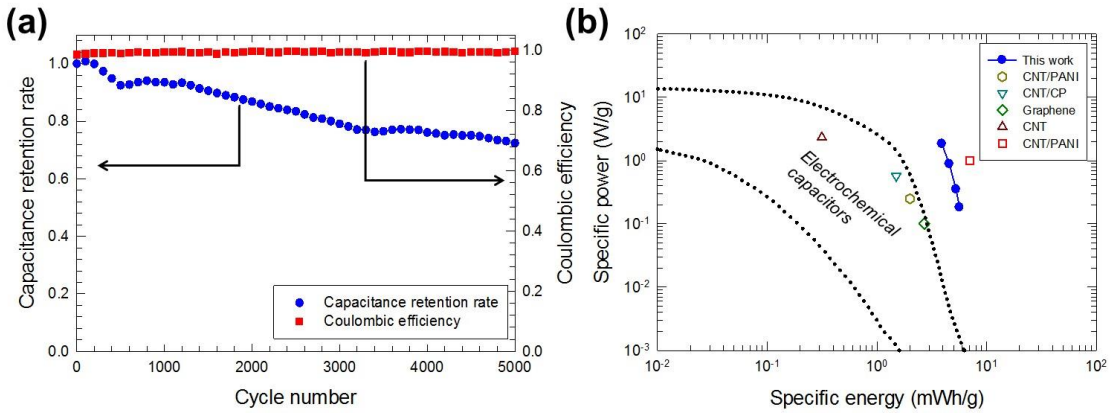

Figure 29. (a) Capacitance retention as a function cycle number at an external charge/discharge current density of 5 mA/cm^2. (b) Ragone plots for the electrode materials along with literature values. The region surrounded by the dashed lines are for typical electrochemical capacitors (reprinted from [86]).

4.3.5 Heat transfer analysis with human body heat

We carried out steady-state heat transfer analysis to see if our TCSC can be used as a power source for wearable devices as well as identify critical design factors.

The temperature gradient in thermally chargeable supercapacitor (TCSC) along the out-of-plane direction was estimated when it is attached to a human body under the assumption of steady-state heat dissipation from the human body through the TCSC device. We modeled TCSC as a square thin film, as shown in Fig. S3. Considering heat

convection, radiation, and latent heat of vaporization, conservation of energy can be expressed as:

$$Q_{Body\_heat} = Q_{cond} = Q_{conv\_top} + Q_{conv\_side} + Q_{rad\_top} + Q_{rad\_side} + Q_{latent} \quad (4.4)$$

where Q is heat rate (W). In this model, human body was assumed to be a constant temperature (37 °C) heat source. Therefore, heat flux from the human body to the TCSC device (Q_{Body_heat}) can be varied depending on the heat dissipation (cooling) conditions.

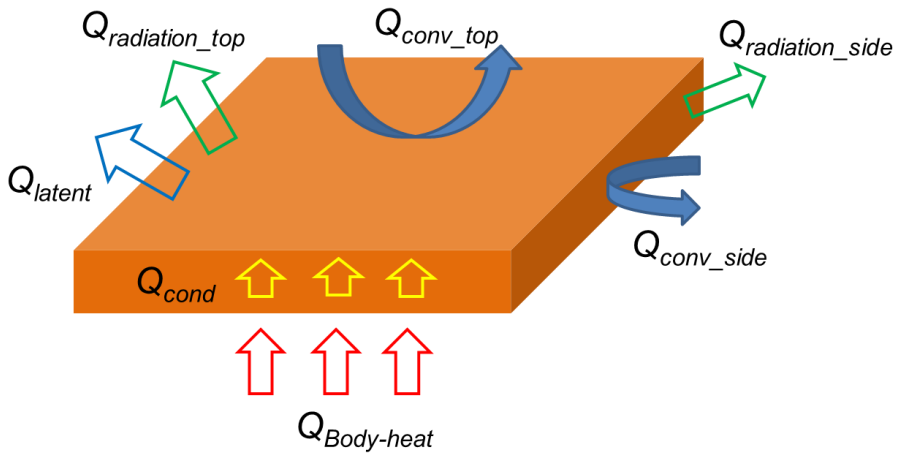

Figure 30. Heat transfer analysis in TCSC considering heat convection, radiation, and latent heat of vaporization, and human body heat (heat source) (reprinted from [86]).

Heat conduction, Q_{cond} can be written as:

$$Q_{cond} = kA_{surf}\frac{\partial T}{\partial z} \quad (4.5)$$

where k is the thermal conductivity of the PSSH film; A_{surf} is the area of top surface; and dT/dz is the temperature gradient along the thickness direction. Here we assumed that the

thermal resistance through the electrodes is small. We used experimentally obtained k = 0.38 W/m-K using the ASTM D5470 method and the surface area is 0.49 cm^2 (0.7 cm ×0.7 cm).

Heat convection, Q_{conv} can be written as:

$$Q_{cond\_top} = hA_{surf}\left(T_{surf} - T_{air}\right) \tag{4.6}$$

$$Q_{conv\_side} = \int_0^t hw\left(T_{side}(z) - T_{air}\right)dz \tag{4.7}$$

where h is the convection heat transfer coefficient; w is the width of the side surface (or the side length of the square); $T_{surface}$ is the temperature of top surface; T_{air} is the temperature of ambient air (22 °C); and t is the thickness of TCSC. Note that $T_{side}(z)$ is a function of sample thickness because of the temperature gradient along the thickness direction. Convection heat transfer coefficient (h) for a human body was calculated from the following empirical equation:

$$h = 14.8V_{air}^{\ 0.69} \tag{4.8}$$

where V_{air} is the velocity of air. Note that this equation is valid for an air velocity between 0.15 and 1.5 m/s. In our calculation, h was assumed to be 20 W/m^2-K, which corresponds to 1.5 m/s at 1 atm.

Radiative heat dissipation, Q_{rad} can be expressed as:

$$Q_{rad\_top} = \varepsilon\sigma A_{surf}\left(T_{surf}^4 - T_{air}^4\right) \tag{4.9}$$

$$Q_{rad\_side} = \int_0^t \varepsilon\sigma w\left(T_{side}(z)^4 - T_{air}^4\right)dz \tag{4.10}$$

where ε is emissivity; and σ is the Stefan–Boltzmann constant (5.67×10^{-8} W/m^2-K^4). ε was assumed to be 0.9, which is a typical value for polymers.

By utilizing the hygroscopic characteristics of PSSH materials, we assume that we can utilize latent heat loss mechanism. Q_{latent} can be written as:

$$Q_{latent} = h_{vap} g_s A_{surf} \tag{4.11}$$

where h_{vap} is the enthalpy of vaporization for water at ambient temperature (2.4×10^6 J/kg); and g_s is the amount of water evaporation per second per area (7.3×10^{-5} kg/m^2-s). Note that g_s value was estimated by the sweat evaporation rate of human body in a hard-working condition according to the ASHRAE standard. The calculated temperature difference as a function of thickness is shown in Figure 31.

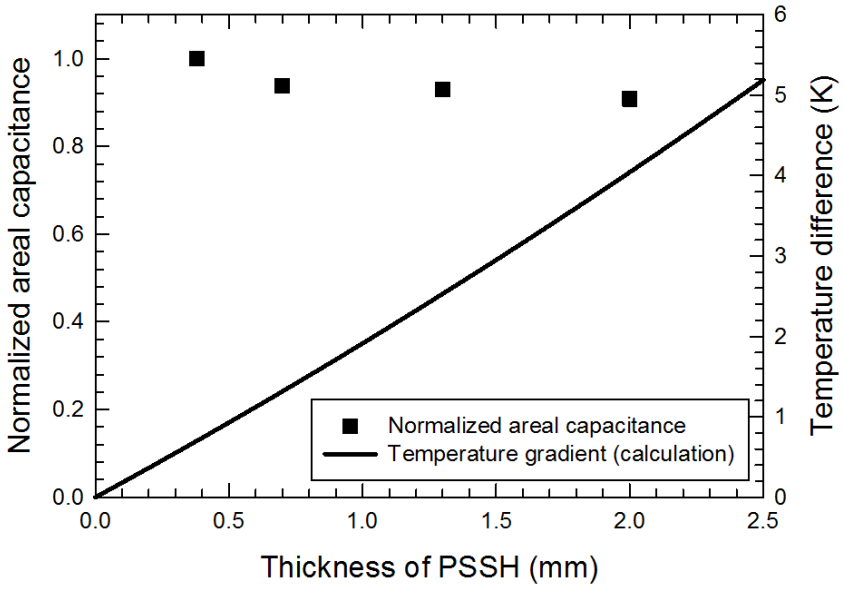

Figure 31. Normalized areal capacitances of TCSC measured by CV test and calculated ΔT between two electrodes in TCSC as a function of PSSH thickness (reprinted from [86]).

As depicted in Figure 30, the heat transferred from human body is dissipated to ambient air by heat convection and radiation and the latent heat of vaporization. As thicker PSSH increases the temperature difference (ΔT) between two electrodes and thereby the charging potential, ΔT as a function of film thickness was calculated with steady-state heat dissipation from the human body [108-109] to simulate a condition for wearable devices (Figure 31). On the other hand, a longer distance between two electrodes may adversely affect ion transport, so areal capacitance values corresponding to four different PSSH thicknesses (0.4, 0.7, 1.3, and 2 mm) were compared by CV measurements. We found that the areal capacitance slightly decreased with thicker PSSH, presumably due to the high ionic conductivity of PSSH film. Therefore, we decided to use 2-mm thick PSSH for our TCSC device to obtain higher output voltage with marginal decrease in the capacitance.

4.3.6 Demonstration of thermally charging behavior of TCSC device

We tested our TCSC with two different ΔT of 5.3 K and 3.5 K, simulating an efficient cooling environment and a relatively sluggish heat dissipation from TCSC, respectively, when our TCSC is used as a wearable energy storage device powered by body heat.

When ΔT of 5.3 K was applied to TCSC, output voltage was increased to 38 mV in 350 seconds (state 2 in Figure 32(a)). This voltage was maintained as long as ΔT of 5.3 K was maintained, and the stored energy can be directly used for powering electronic devices. In case that ΔT needs to be removed, the energy can be stored as a form of

chemical energy using the redox reactions of PANI. In our experiment, we closed the circuit with a 1-kΩ load resistor to initiate the redox reactions of PANI in both electrodes by electrons transfer from the hot electrode to the cold electrode until the voltage became zero while maintaining the temperature gradient. It should be noted that this is a charged state with different redox states (potentials) at the two electrodes but the voltage is zero (state 3 in Figure 32(a)) due to the potential created by the ΔT with the opposite polarity.

After removing ΔT and the load resistor, thermally diffused protons toward the cold electrode became randomly distributed, eliminating the electrode potential produced by protons and thereby resulting in a "charged" state with a negative voltage (state 4 in Figure 32(a)) close to the initially charged voltage (state 2) in magnitude. The charged state was maintained for longer than 24 hours (inset of Figure 32(a)), which is an outstanding retention capability. Another test with ΔT of 3.5 K resulted in a lower output voltage, indicating the thermally charging behaviors strongly depend on the temperature gradient (Figure 32(b)).

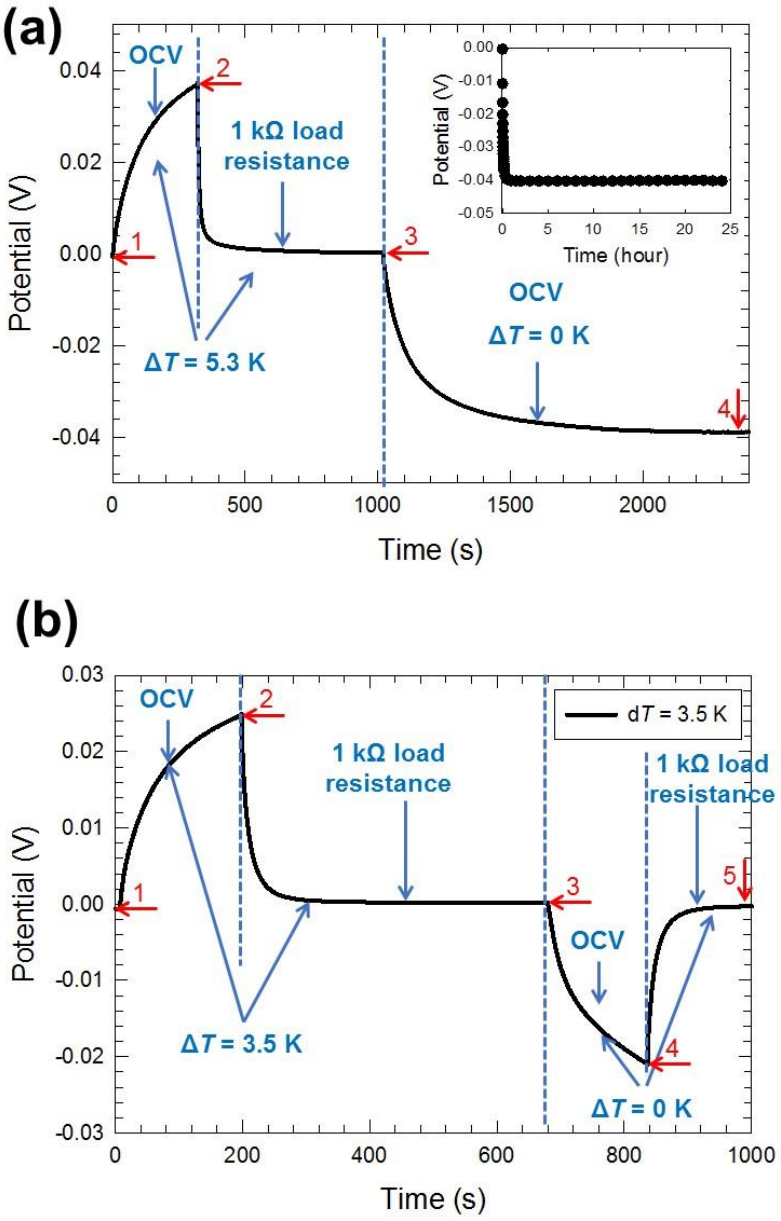

Figure 32. Thermally charging behaviors with ΔT of (a) 5.3 K and (b) 3.5 K. (1-2) After making ΔT of 5.3 K between two electrodes, open circuit voltage (OCV) started to increase and reached ~40 mV after ~300 s. (2-3) Engaging a 1-kΩ load resistor to initiate electrochemical reactions by transferring electrons for charging the supercapacitor. (3-4) Disengaging the load resistor and removing ΔT. (4) Charged state of TCSC without ΔT. OCV reached about -38 mV. The inset shows the voltage can be maintained over 24 hours, indicating stable performance without parasitic loss (reprinted from [86]).

Additionally, the contribution from the temperature-dependent redox potential to the thermally induced voltage was measured to be ~0.2 mV/K, which is negligible compared to that from the Soret effect. The temperature-dependent redox potential (typically called thermogalvanic coefficient, S_{redox}) of P-G/CNT was measured to identify its contribution to the large thermally-induced potential in our TCSC. S_{redox} was measured by following a previously reported procedure [110]. First, S_{redox} of an Ag/AgCl reference electrode (CH111, CH instruments) was measured as a standard reference in a non-isothermal cell for a calibration purpose. Then electrochemical redox reaction potentials of P-G/CNT were measured against the Ag/AgCl electrode at different temperatures in an isothermal cell.

For calibration (Figure 33(a)), one of the two Ag/AgCl electrodes was kept at temperature (T_{hot}) hotter than room temperature for 6 hr to have enough time for the electrode to reach Thot. Then the electrode was quickly immersed in a 4-M KCl electrolyte solution at room temperature and its potential was recorded. S_{redox} of P-G/CNT was measured with a three-electrode configuration (Figure 33(c)) in a cell filled with 5-wt% aqueous PSSH electrolyte. A tip-insulated T-type thermocouple was placed next to the working electrode to measure temperature. Then the cell was placed in a convection oven for measuring S_{redox} of P-G/CNT electrode. We waited for ~6 hr at each temperature to obtain a steady state. The electrochemical potentials of P-G/CNT against the Ag/AgCl electrode were measured at 4 different temperatures, and the potentials after calibration with S_{redox} of Ag/AgCl were plotted in Figure 33(d). From the slope of the linear fitting line, S_{redox} of P-G/CNT was measured to be 0.21 mV/K. Considering

the thermally induced potential of TCSC device (~8 mV/K), we concluded that the contribution of S_{redox} of P-G/CNT to the output voltage of TCSC is relatively small (~2.5 %).

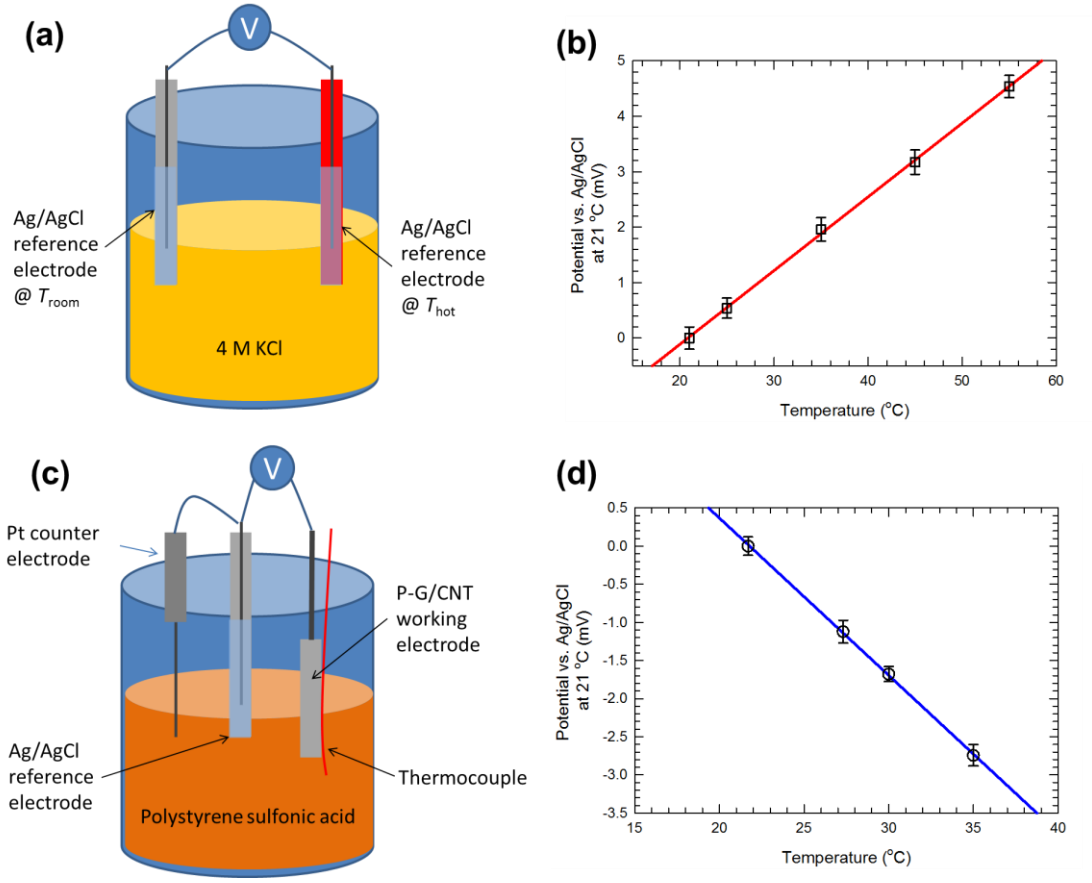

Figure 33. Measurements of temperature-dependent redox potential (S_{redox}). (a) A setup to measure S_{redox} of an Ag/AgCl reference electrode. (b) Ag/AgCl electrode potential *vs.* temperature. The slope of the fitting line was found to be 0.132 ± 0.02 mV/K. (c) A setup to measure S_{redox} of P-G/CNT. (d) The electrochemical potential of P-G/CNT electrode against an Ag/AgCl reference electrode as a function of cell temperature. Note that the potentials were calibrated with S_{redox} of Ag/AgCl. The slope of the fitting line was found to be 0.21 ± 0.01 mV/K (reprinted from [86]).

To estimate the thermally-charged areal capacitance of TCSC, the charging process was performed under ΔT of 5.3 K, and then the device was discharged at a constant current of 5 μA (0.01 mA/cm^2) (Figure 34). According to these results, the areal capacitance of the device was calculated to be 120 mF/cm^2, almost 25% of the areal capacitance of the supercapacitor charged by an external power source. Similarly, charging/discharging characteristics for ΔT of 5.3 K are also shown in Figure 34.

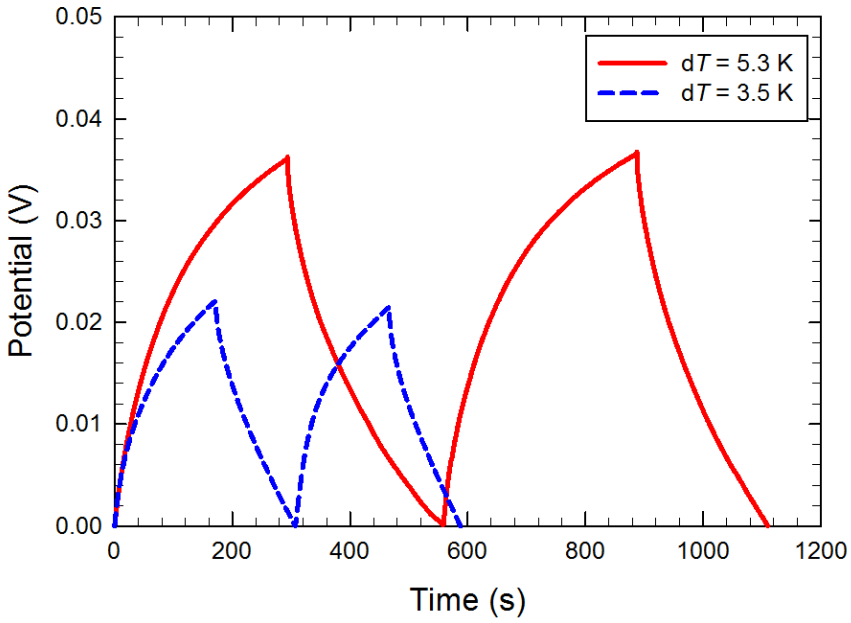

Figure 34. Thermally charging TCSC with ΔT of 5.3 K and 3.5 K, and discharging at a constant current density of 0.01 mA/cm^2 (reprinted from [86]).

4.4 Conclusions

In conclusion, we have successfully demonstrated a new concept to harvest thermal energy and store electrical energy simultaneously as well as feasibility as a wearable power harvesting/storage device. Our TCSC consists of a PSSH electrolyte acting as a thermal energy harvester and P-G/CNT electrodes for storing electrochemical energy. Thermally-driven ion movement in PSSH was utilized to charge up a solid-state supercapacitor by enabling electrochemical reactions at the electrodes without external power sources. With ΔT of 5.3 K, a charged potential of 40 mV and an areal capacitance of 120 mF/cm^2 were achieved. We believe that our new concept for converting thermal energy into electrical energy suggests a new innovative direction in thermal energy harvesting, and further studies may result in a practically viable sustainable power generation method for wearable electronics operated by body heat.

CHAPTER V

HIGH THERMO-INDUCED VOLTAGE BY IONIC MOVEMENT IN SOLID-STATE POLYMER ELECTROLYTE

5.1 Introduction

An innovative renewable energy source is one of the most significant challenges to solve dramatically increasing energy consumption. Low-grade thermal energy is a highly attractive candidate as a sustainable energy source, owing to its abundance and accessibility. For example, waste heat from human body and portable electronics can be utilized as useful power sources to operate wearable electronic devices. Therefore, the efficient conversion of heat directly into electrical energy is very important technology especially in low-grade thermal energy harvesting. In recent years, various mechanisms for the direct conversion of heat into electricity have been intensely studied to enhance the efficiency.

First, conventional thermoelectric materials utilize electron diffusion in semiconductors by a temperature gradient (Seebeck effect). Despite much progress of thermoelectric efficiency over the past decades, practical applications of thermoelectric materials are constrained by low output voltage as a result of small Seebeck coefficients, which is typically on the order of ~100 μV/K. On the other hand, the thermogalvanic cell operates based on temperature-dependent electrochemical redox potential, which can produce a relatively high voltage (~2 mV/K) [18-19]. However, liquid electrolyte-based

thermogalvanic cells require bulky packaging to prevent leakage that would eventually lead to a reduced lifetime, which is not favorable to wearable and flexible applications.

Recently, researchers have become interested in the thermo-diffusion of ions (Soret effect) in electrolytes or ion conductors for thermal energy harvesting applications because of their capabilities of producing high voltage. It has been reported that an ion concentration gradient created by a temperature gradient can produce an output voltage up to 10 mV/K in liquid electrolyte systems [20, 23]. Also, the solid-state thermogalvanic system based on polymer electrolytes can produce high thermo-induced voltage by utilizing the thermo-diffusion of ions [21]. However, the thermal-to-electrical energy conversion utilizing the Soret effect in redox-free solid-state polymer electrolytes, to the best of our knowledge, has not previously been reported. Since it has been shown in liquid electrolyte systems that the Soret effect of ions can be utilized as electrical double layer capacitors, the study of the thermo-induced voltage in solid-state polymer electrolytes is important for the development of solid-state thermal energy harvesting and storage devices.

In redox free ionic conductors or electrolytes, the physical origin of the thermo-induced voltage is the characteristic response of the different ions to the temperature gradient. Thermo-diffusion of ions along the temperature gradient creates an ionic-charge gradient, leading to a thermoelectric field. To explain this phenomenon, the equations of thermally-driven ion flux are adopted. The mobile ion current of each species can be expressed as

$$J_i = -D_i\left(\nabla n_i + 2n_i\alpha_i\frac{\nabla T}{T} - n_i\frac{q_i E}{k_B T}\right) \tag{5.1}$$

which comprises normal diffusion with the Einstein coefficients D_i, thermo-diffusion with the reduced Soret coefficient α_i, and electrophoresis for monovalent ions, where q_i is the charge of ions, n_i is the ion densities, k_B is the Boltzmann constant, and T is the temperature. Considering steady-state condition ($\sum J_i$=0) and no net charge density ($\sum q_i \nabla n_i$=0) in a macroscopic binary electrolyte sample, the thermo-induced voltage is expressed as

$$\nabla V = -\left(\alpha_{cation} - \alpha_{anion}\right)\left(k_B/e\right)\nabla T \tag{5.2}$$

Typically, one of the ion species moves more rapidly, resulting in a thermo-induced voltage between hot and cold sides, which is proportional to the temperature gradient and the Soret coefficient difference of ions.

Herein, we prepared two different types of proton-conducting solid-state polymer electrolytes and successfully demonstrated very large electric potential originating from thermally-driven ion movement along the temperature gradient. The analysis of thermopower from the ion flux equation is directly applied to this work to explain the large thermopower of polymer electrolytes. Also, the influence of the plasticizers (water molecules in this work) on thermopower and electrical conductivity of polymer electrolytes was explored by controlling the relative humidity (RH) of samples. Finally, the solid-state electrolyte samples containing both mobile cations and anions were prepared to confirm the advantages of single-ion conducting polymer electrolytes.

5.2 Experimental

5.2.1 Material synthesis

Sulfonated polyether ether ketone (S-PEEK) has been synthesized by following the procedure in the previous literatures [111]. PEEK (Sigma Aldrich) was dried in a vacuum oven at 100 °C overnight. Thereafter, it was gradually added into H_2SO_4 (95–98%, BDH) in a glass bottle. The sulfonation was carried out at 40 °C for 6 hr while being vigorously stirred. The sulfonation reaction was terminated by precipitating the polymer solution into a large excess of ice-cold water. The precipitated polymers were soaked in water overnight and then washed successively with deionized water by using a filtration set-up until the pH was neutral. The S-PEEK polymer was dried at room temperature overnight and then in a vacuum oven at 60 °C for 24 h. Dried S-PEEK was dissolved at a concentration of 10 wt% in N-Methyl-2-pyrrolidone (NMP) solvent (J.T.Baker). The polymer solution was drop-cast onto a glass substrate and then left in a fume hood to vaporize the solvent at room temperature for 24 hr. Subsequently, the sample was dried in a vacuum oven at 80 °C for 24 hrs.

Nafion 115 membrane was purchased from Fuel Cell Earth and post-treated by following the standard procedures for activation. Firstly, the membrane was refluxed in H_2O_2 (3%, Fisher chemical) for 1 hr to oxidize the inorganic impurities. And then it was soaked in deionized water at 80 °C for 1 hr. Thereafter, Nafion was refluxed in 2M H_2SO_4 at 80 °C for 6 hr to ensure complete protonation of Nafion. Finally, it was soaked in deionized water at room temperature for 2 h to remove excess acid. Before the experiments, activated Nafion was dried in the fume hood at room temperature for 24 hr.

PVA-H_3PO_4 electrolyte was simply prepared by mixing 1 g of polyvinyl alcohol (PVA) powder (99.8%, J.T.Baker) and 0.8 g of H_3PO_4 (85%, Fisher chemical) in 10 mL of deionized water. Then the mixture was heated to 90 °C under vigorous stirring until the solution became clear. PVA-NaOH electrolyte was prepared by following same procedure above with 0.5 g of NaOH (Amresco) instead of H_3PO_4. The polymer solution was drop-cast onto a glass substrate and then left in the fume hood to remove the excessive water at room temperature for 24 hr.

5.2.2 Ion exchange capacity measurement

The ion exchange capacity (IEC) of the S-PEEK was measured by using the classical titration method [111-112].1, 4 Firstly, we measured the weight of fully dried S-PEEK film. After that, the film was immersed in the saturated NaCl solution for 24 hr to exchange H^+ ions from the S-PEEK with Na^+ ions. The amount of H^+ exchanged from the S-PEEK film was determined by titrating with 0.1 M NaOH solution, using phenolphthalein (BDH Chemicals) as an indicator. The IEC of the S-PEEK was calculated by following equation [112]:

$$IEC = \frac{C_{NaOH} V_{NaOH}}{W_{dry}} \tag{5.3}$$

where C_{NaOH} is the molarity of NaOH, V_{NaOH} is the consumed volume of NaOH solution, and W_{dry} is the weight of fully dried sample. IEC of the as-prepared S-PEEK was measured to be 2.08 mmol/g.

Degree of sulfonation (DS) of S-PEEK can be calculated by using the IEC and following equation:

$$DS = \frac{IEC}{\left(1 - A \times IEC\right) / B + IEC} \tag{5.4}$$

where A and B are the molecular weight of the repeat unit of sulfonated PEEK (369.4 g/mol) and pristine PEEK (288.3 g/mol), respectively. DS value of the as-prepared S-PEEK was calculated to be 71%.

5.2.3 Electrical property measurements

For the electrical property measurements, S-PEEK, PVA-NaOH, and PVA-H_3PO_4 samples were prepared on glass slides (7~8 mm in width and 25 mm in length) whose two ends were coated by carbon paste (electrodes for the measurements) prior to the deposition of the samples. The electrodes of Nafion were prepared by applying carbon paint at the two ends of the film. Typical sample thickness was measured to be 90~120 μm. The samples were suspended (along the long edge direction) between two thermoelectric devices that were serially connected to a DC power supply (Figure 35). One thermoelectric device was cooled while the other was heated. Temperature sweeping between +2.5 K and -2.5 K for each thermoelectric device was carried out to create various temperature differences between -5 and +5 K as well as ensure no hysteresis. For temperature and voltage measurements, T-type thermocouples consisting of copper and constantan wires were mounted on the carbon electrodes. Thermo-induced voltage was measured using the copper wire, and temperature was measured with the

copper-constantan wire couple (T-type thermocouple). This configuration is to ensure the locations for the temperature and voltage measurements identical. Two additional electrical contacts at both ends of the samples were also made to measure 4-probe electrical resistance.

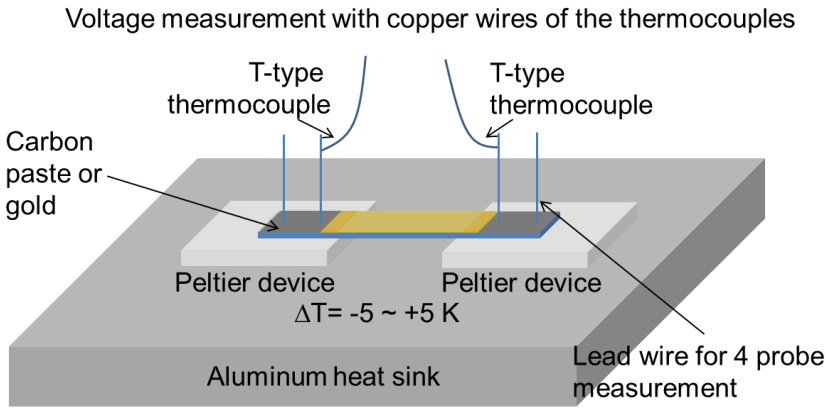

Figure 35. Schematic illustration of the set-up for measuring electrical conductivity and thermopower.

Prior to making temperature gradients, linear current-voltage relations were obtained from the 4-probe measurements, confirming Ohmic contacts. Upon creating 6-8 different temperature gradients across the sample, thermally induced voltage values were recorded and then linear slopes were found to obtain thermopower. The dc conductivity measurements were confirmed by conducting electrochemical impedance spectroscopy (EIS), as shown in Figure 36.

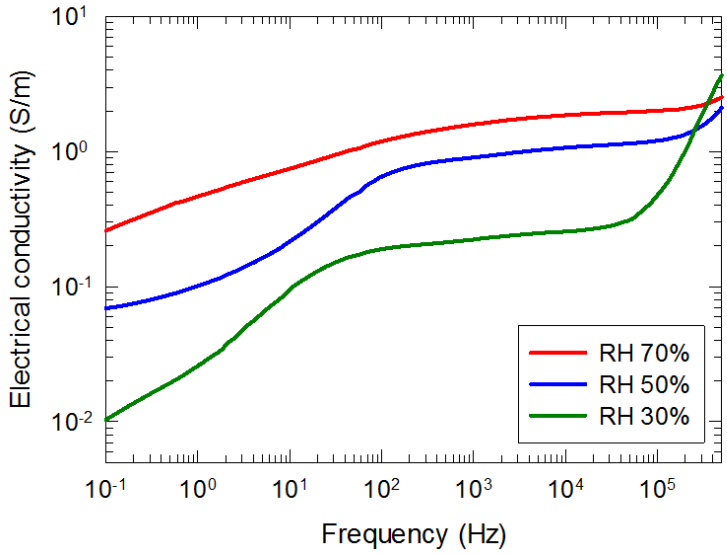

Figure 36. EIS results of Nafion in different RH conditions (30%, 50%, 70%).

5.3 Results and discussion

5.3.1 Chemical structures of S-PEEK and Nafion

Figure 37(a) shows the chemical structures of two polymer electrolytes, sulfonated polyether ether ketone (S-PEEK) and Nafion. Both of these samples consist of sulfonate anions tethered to the polymer backbone and mobile protons. Ion components in the polymer electrolyte and their response to a temperature gradient are illustrated in Figure 37(b). A temperature gradient drives an ion movement and results in voltage generation via a charge concentration gradient across the sample. It should be noted that only protons are mobile and the thermally-driven movement of anions is negligible since sulfonate ions are immobilized by high molecular weight polymer backbone. In this sense, polymer electrolytes have a great advantage in improving the

thermopower, which can be explained by equation (2). At a given temperature gradient (∇T), a voltage difference (∇V) will be higher when one of the reduced Soret coefficients (α_{anion}) is close to zero, preventing a charge cancellation between cations and anions.

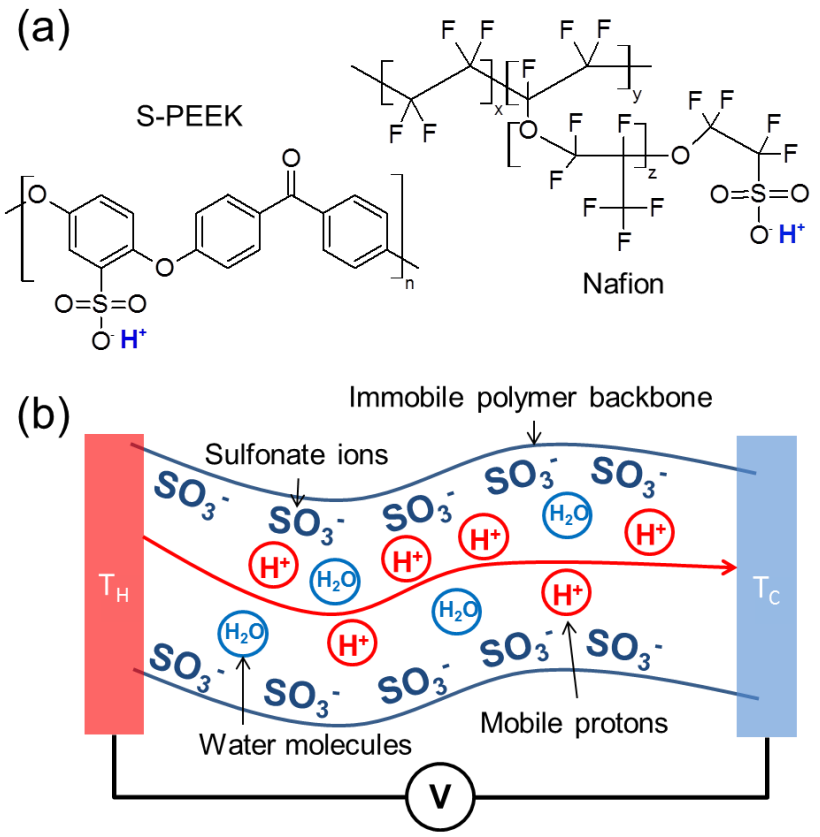

Figure 37. (a) Chemical structures of sulfonated polyether ether ketone (S-PEEK) and Nafion. (b) Schematic illustration of thermo-induced voltage generation from ionic movements in polymer electrolyte under a temperature gradient.

5.3.2 Thermoelectric properties of S-PEEK and Nafion

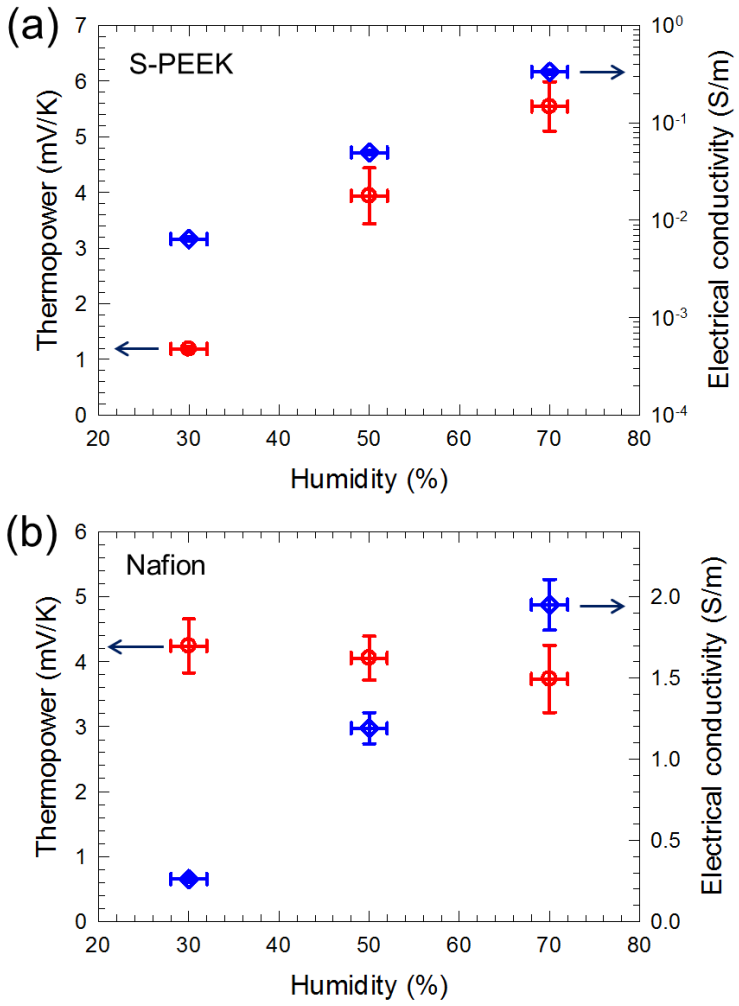

Figure 38. Thermopower and electrical conductivity of (a) S-PEEK and (b) Nafion as a function of RH condition.

Figure 38 shows the thermopower and electrical conductivity of S-PEEK and Nafion. Since ionic transport properties of polymer electrolytes are well known to be very sensitive to humidity, all thermopower and electrical conductivity measurements

were conducted over a wide RH range from 30% to 70%. A four-probe method was employed to obtain electrical conductivity from the slope of the linear current-voltage relation and the values were confirmed by conducting electrochemical impedance spectroscopy measurement. For thermopower measurements, voltage across the sample was measured at various temperature differences, and then thermopower was obtained from the linear slope. Note that all measurements were conducted in inert environment by flowing nitrogen gas.

As shown in Figure 38(a), at 70% RH condition, the thermopower of S-PEEK film was measured to be ~5.5 mV/K, which is much higher than the reported Seebeck coefficient from conventional thermoelectric materials and thermo-electrochemical cells. The thermopower rises as the RH level is increased. The electrical conductivity of S-PEEK at 70% RH was around 0.3 S/m, which is 50 times higher than that at 30% RH. This exponential increase of the electrical conductivity at higher RH levels is likely to come from a better solvation and enhanced mobility of protons since water promotes the dissociation of proton from the sulfonic group and higher RH may allow water to form more percolated pathways for protons. It is interesting to observe that the thermopower and electrical conductivity of S-PEEK increased simultaneously at higher humidity condition. These behaviors are very different from the inverse proportional relationships between thermopower and electrical conductivity in typical bulk thermoelectric materials.

On the other hand, Nafion shows a different trend of thermopower with respect to RH condition from that of S-PEEK. As shown in Figure 38(b), the thermopower of

Nafion is measured to be very high (~4.2 mV/K) like S-PEEK, but the value doesn't change much (slightly decreases) at higher humidity conditions. The electrical conductivity shows dramatic improvement in higher RH conditions, which is similar to S-PEEK. This behavior is consistent with the previous report that water molecules in Nafion act as plasticizers to enhance the ion transport by improving mobility. To explain the dissimilar behavior of S-PEEK and Nafion at higher humidity, we hypothesize that if there is thermo-diffusion phenomenon of the plasticizer molecules through the polymer electrolytes, the movement of water molecules fairly affects the Soret coefficient of ions. It has been well-studied that water molecules can diffuse easily through the percolated channels in the Nafion membrane. Also, it is interesting to note that the thermo-osmosis direction of water molecules in Nafion under a temperature gradient is from the cold side to the hot side, which is the opposite direction of the thermally-driven proton movement. Therefore, we believe that the slight decrease of thermopower at higher humidity might be due to the fact that osmotic pressure associated with the thermal diffusion counteracts the driving thermal force to protons, reducing the Soret coefficient. Since the water diffusivity of S-PEEK is one order lower than that of Nafion, the thermo-diffusion of protons is less affected by osmotic pressure.

Agar *et al.* developed a model based on the Born theory to calculate the ionic heat of transport (Q^*), which makes it possible to estimate α of ion species in diluted aqueous solution by using $\alpha = Q^*/2RT$, where R is the gas constant and T is the temperature [51]. According to this model, the Q^* of H^+ is 13.3 kJ/mol and the thermopower raised by a proton concentration gradient is estimated to be 0.23 mV/K,

which is over 20 times lower than our measurement value with S-PEEK. We believe that this large difference between the measured value of polymer electrolyte and calculated one of diluted liquid electrolyte might be due to the limitation of the Agar's model, which doesn't consider the interaction between solvent and ion species. In the model, the reduced Soret coefficient α embodies only the coupling of a single ion with the thermal field and is assumed to have the fixed value for specific ion. However, differing from ions in a dilute solution, mobile ions in a polymer electrolyte should consider the interaction with charged polymer backbones. Because the charged polymer backbone significantly contributes to the selective transport of mobile counter ions by creating stationary charged paths. It has been reported that a Soret coefficient of ions in the salt solutions is expected to show two orders of magnitude improvement by adding the polyelectrolyte. Therefore, we believe that the charged paths in polymer electrolyte greatly enhance the thermo-diffusion capability of mobile ions, resulting in higher thermopower than liquid electrolyte with same ion species.

5.3.3 Comparative study of polyelectrolyte and binary electrolyte

For this comparative study, we prepared two different polyvinyl alcohol (PVA)-based solid-state electrolytes, basic PVA-NaOH and acidic PVA-H_3PO_4. As shown in Figure 39(a), PVA is a polymer matrix to hold water molecules, which makes it possible to dissociate H_3PO_4 and NaOH into H^+/HPO_4^- and Na^+/OH^-, respectively. These gel-type electrolytes can be considered as a binary aqueous electrolyte where cations and anions can migrate simultaneously along the temperature gradient (Figure 39(b)). Figure 39(c)

shows the experimental results of the thermopower of PVA-NaOH and PVA-H_3PO_4. The thermopower of PVA-NaOH was measured to be -1 mV/K which is independent on the RH condition. Based on the negative thermopower, it can be assumed that the Soret coefficient of anion is higher than that of cation. Our measurement result of the negative thermopower is consistent with the thermoelectric field created in the aqueous NaOH solution. Furthermore, it is interesting to find that this behavior can be explained by the ionic heat transport from the Agar model. In the model, OH^- ion has much higher α than Na^+ so that overall thermopower is expected to have a negative value. Therefore, we believe the Agar model is valid to estimate the thermo-diffusion of ions in the PVA-based samples. PVA-H_3PO_4 showed the thermopower of 1.6 mV/K and it is almost maintained over different RH conditions. Our measurement values are very similar to the previously reported thermopower of the nitric acid solution (1.5 mV/K). In the report, the anion (NO_3^-) was expected to have very small α based on the Agar model. Therefore, it is reasonable to assume that $H_2PO_4^-$ also has a negligible Soret coefficient and the proton is the major contributor to the thermo-induced voltage in the PVA-H_3PO_4. In terms of the thermopower, it is shown that the proton-conducting polymer electrolytes have the advantages over the proton-dominant binary electrolytes, confirming the benefit of polymer chains creating the charged pathways which presumably enhance the Soret coefficient of mobile ions. Future work in this area will be focused on investigating the optimal polymer backbone structures which enable more facile thermally-driven movement of mobile ions, thereby providing higher thermopower and electrical conductivity simultaneously for more efficient thermal energy harvesting devices.

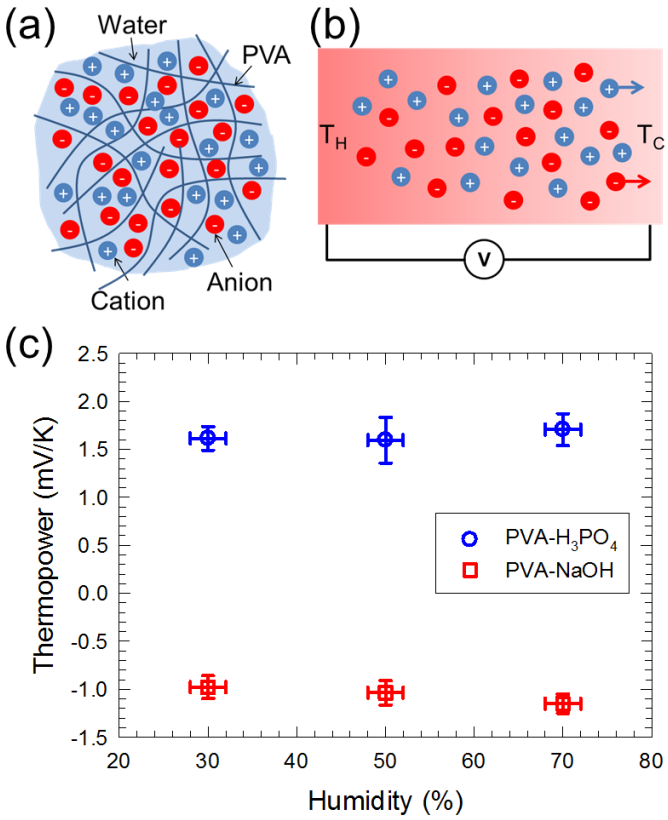

Figure 39. Schematic illustrations of (a) PVA-based gel electrolyte containing cations and anions in polymer matrix and (b) thermo-diffusion of ions under a temperature gradient. (c) Thermopower of PVA-NaOH and PVA-H_3PO_4 electrolytes as a function of RH condition.

Table 3 shows the summary of the thermoelectric properties of solid-state polyelectrolytes as well as solid-state salt electrolytes. As depicted in the table, polyelectrolyte samples showed around 5 to 8 times higher thermopower than salt electrolyte, confirming the benefit of polymer backbone immobilizing one of the ions and enhance the overall thermopower of samples.

Table 3. Thermoelectric properties of polyelectrolytes and salt electrolytes.

Sample		Thermopower (@ RH 70%)	Electrical conductivity (@ RH 70%)	Note
Polyelectrolyte	PSSH	8 mV/K	8 S/m	
	S-PEEK	6 mV/K	0.3 S/m	Humidity sensitive
Salt electrolyte	PVA/H_3PO_4	1.5 mV/K	3 S/m	
	PVA/NaOH	-1 mV/K	0.8 S/m	n-type

5.4 Conclusions

In conclusion, we have successfully demonstrated very large thermopower values (~5.5 mV/K) in solid-state polymer electrolyte films. The thermo-induced voltage in ionic conductors is generated by an ionic-charge gradient created by the thermo-diffusion of ions along the temperature gradient. We believe that the exceptionally high thermopower of the polymer electrolyte is mainly due to the charged path of polymer chains that might lead to dramatic improvement of the Soret coefficient of mobile ions. A positive effect of charged polymer chains has been experimentally confirmed by measuring the thermopower of proton-dominant binary electrolytes without charged pathways. Finally, it has been observed that the plasticizers such as water molecules in polymer electrolytes can enhance the thermopower and electrical conductivity at the same time by improving the ion mobility. Our new findings of very high thermopower in

solid-state films and further studies may result in practically viable thermal energy harvesting/storing devices for wearable and flexible electronics.

CHAPTER VI

SUMMARY

The ultimate goal of this dissertation was to develop highly efficient thermal energy harvesting system based on carbon-based organic materials including CNT and polymers. This dissertation utilized two different mechanisms, Seebeck effect and Soret effect, to efficiently convert heat energy into electricity. Especially, the Soret effect in solid-state ionic conductors, which has rarely been studied before, was utilized in this work to fabricate a new concept of energy device.

By utilizing the Seebeck effect in CNT, I developed both p- and n-type fabric-like flexible light-weight materials by functionalizing the large surfaces and junctions in CNT mats. The poor thermopower and only p-type characteristics of typical CNTs have been converted into both p- and n-type with high thermopower. The changes in the electronic band diagrams of the CNTs were experimentally investigated, elucidating the carrier type and relatively large thermopower values. With the optimized device design to maximally utilize temperature gradients, an electrochromic glucose sensor was successfully operated without batteries or external power supplies, demonstrating self-powering capability. While the fundamental study provides a method of tailoring electronic transport properties, our device-level integration shows the feasibility of harvesting electrical energy by attaching the device to even curved surfaces like human bodies.

Secondly, I have successfully demonstrated a new concept to harvest thermal energy and store electrical energy simultaneously as well as feasibility as a wearable power harvesting/storage device. TCSC consists of a PSSH electrolyte acting as a thermal energy harvester and P-G/CNT electrodes for storing electrochemical energy. Thermally-driven ion movement in PSSH was utilized to charge up a solid-state supercapacitor by enabling electrochemical reactions at the electrodes without external power sources. With ΔT of 5.3 K, a charged potential of 40 mV and an areal capacitance of 120 mF/cm^2 were achieved. We believe that our new concept for converting thermal energy into electrical energy suggests a new innovative direction in thermal energy harvesting, and further studies may result in a practically viable sustainable power generation method for wearable electronics operated by body heat.

Lastly, as a fundamental study to investigate the origin of the thermally induced voltage in polyelectrolytes, I have compared the thermoelectric properties of polyelectrolyte and salt-based binary electrolyte. As a result, I have successfully demonstrated very large thermopower values (~5.5 mV/K) in solid-state polymer electrolyte films. The thermo-induced voltage in ionic conductors is generated by an ionic-charge gradient created by the thermo-diffusion of ions along the temperature gradient. We believe that the exceptionally high thermopower of the polymer electrolyte is mainly due to the charged path of polymer chains that might lead to dramatic improvement of the Soret coefficient of mobile ions. A positive effect of charged polymer chains has been experimentally confirmed by measuring the thermopower of proton-dominant binary electrolytes without charged pathways. Finally, it has been

observed that the plasticizers such as water molecules in polymer electrolytes can enhance the thermopower and electrical conductivity at the same time by improving the ion mobility. The new findings of very high thermopower in solid-state films and further studies may result in practically viable thermal energy harvesting/storing devices for wearable and flexible electronics.

REFERENCES

1. Zhao, L.-D.; Tan, G.; Hao, S.; He, J.; Pei, Y., *et al.*, Ultrahigh power factor and thermoelectric performance in hole-doped single-crystal SnSe. *Science* **2016,** *351* (6269), 141-144.
2. Zhao, L.-D.; Lo, S.-H.; Zhang, Y.; Sun, H.; Tan, G., *et al.*, Ultralow thermal conductivity and high thermoelectric figure of merit in SnSe crystals. *Nature* **2014,** *508* (7496), 373-377.
3. Liu, W.; Zhou, J.; Jie, Q.; Li, Y.; Kim, H. S., *et al.*, New insight into the material parameter B to understand the enhanced thermoelectric performance of Mg 2 Sn 1− x− y Ge x Sb y. *Energ. Environ. Sci.* **2016,** *9* (2), 530-539.
4. Tang, Y.; Gibbs, Z. M.; Agapito, L. A.; Li, G.; Kim, H.-S., *et al.*, Convergence of multi-valley bands as the electronic origin of high thermoelectric performance in CoSb3 skutterudites. *Nature Mat.* **2015**.
5. Kim, S. I.; Lee, K. H.; Mun, H. A.; Kim, H. S.; Hwang, S. W., *et al.*, Dense dislocation arrays embedded in grain boundaries for high-performance bulk thermoelectrics. *Science* **2015,** *348* (6230), 109-114.
6. Heremans, J. P.; Jovovic, V.; Toberer, E. S.; Saramat, A.; Kurosaki, K., *et al.*, Enhancement of thermoelectric efficiency in PbTe by distortion of the electronic density of states. *Science* **2008,** *321* (5888), 554-557.
7. Heremans, J. P.; Wiendlocha, B.; Chamoire, A. M., Resonant levels in bulk thermoelectric semiconductors. *Energ. Environ. Sci.* **2012,** *5* (2), 5510-5530.

8. Pei, Y.; Shi, X.; LaLonde, A.; Wang, H.; Chen, L., *et al.*, Convergence of electronic bands for high performance bulk thermoelectrics. *Nature* **2011,** *473* (7345), 66-69.

9. Vineis, C. J.; Shakouri, A.; Majumdar, A.; Kanatzidis, M. G., Nanostructured thermoelectrics: big efficiency gains from small features. *Adv. Mater.* **2010,** *22* (36), 3970-3980.

10. Minnich, A.; Dresselhaus, M.; Ren, Z.; Chen, G., Bulk nanostructured thermoelectric materials: current research and future prospects. *Energ. Environ. Sci.* **2009,** *2* (5), 466-479.

11. Majumdar, A., Thermoelectricity in semiconductor nanostructures. *Science* **2004,** *303* (5659), 777-778.

12. Snyder, G. J.; Toberer, E. S., Complex thermoelectric materials. *Nature Mat.* **2008,** *7* (2), 105-114.

13. Bubnova, O.; Khan, Z. U.; Malti, A.; Braun, S.; Fahlman, M., *et al.*, Optimization of the thermoelectric figure of merit in the conducting polymer poly(3,4-ethylenedioxythiophene). *Nat. Mater.* **2011,** *10* (6), 429-433.

14. Yu, C.; Kim, Y.; Kim, D.; Grunlan, J. C., Thermoelectric behavior of segregated-network polymer nanocomposites. *Nano Lett.* **2008,** *8*, 4428-4432.

15. Yu, C.; Murali, A.; Choi, K.; Ryu, Y., Air-stable fabric thermoelectric modules made of N- and P-type carbon nanotubes. *Energ. Environ. Sci.* **2012,** *5* 9481-9486.

16. Yu, C.; Choi, K.; Yin, L.; Grunlan, J. C., Light-weight flexible carbon nanotube based organic composites with large thermoelectric power factors. *ACS Nano* **2011,** *5*, 7885-7892.

17. Kim, D.; Kim, Y.; Choi, K.; Grunlan, J. C.; Yu, C., Improved thermoelectric behavior of nanotube-filled polymer composites with poly(3,4-ethylenedioxythiophene) poly(styrenesulfonate). *ACS Nano* **2010,** *4*, 513-523.

18. Hu, R.; Cola, B. A.; Haram, N.; Barisci, J. N.; Lee, S., *et al.*, Harvesting waste thermal energy using a carbon-nanotube-based thermo-electrochemical cell. *Nano Lett.* **2010,** *10* (3), 838-846.

19. Kang, T. J.; Fang, S.; Kozlov, M. E.; Haines, C. S.; Li, N., *et al.*, Electrical power from nanotube and graphene electrochemical thermal energy harvesters. *Adv. Funct. Mater.* **2012,** *22* (3), 477-489.

20. Bonetti, M.; Nakamae, S.; Roger, M.; Guenoun, P., Huge Seebeck coefficients in nonaqueous electrolytes. *J. Chem. Phys.* **2011,** *134* (11), 114513.

21. Chang, W. B.; Evans, C. M.; Popere, B. C.; Russ, B. M.; Liu, J., *et al.*, Harvesting waste heat in unipolar ion conducting polymers. *ACS Macro Lett.* **2016,** *5* (1), 94-98.

22. Wang, H.; Ail, U.; Gabrielsson, R.; Berggren, M.; Crispin, X., Ionic seebeck effect in conducting polymers. *Adv. Energy Mater.* **2015,** *5* (11).

23. Zhao, D.; Wang, H.; Khan, Z. U.; Chen, J. C.; Gabrielsson, R., *et al.*, Ionic thermoelectric supercapacitors. *Energ. Environ. Sci.* **2016,** *9* (4), 1450-1457.

24. Cho, C.; Stevens, B.; Hsu, J. H.; Bureau, R.; Hagen, D. A., *et al.*, Completely organic multilayer thin film with thermoelectric power factor rivaling inorganic tellurides. *Adv. Mater.* **2015,** *27* (19), 2996-3001.

25. Russ, B.; Robb, M. J.; Brunetti, F. G.; Miller, P. L.; Perry, E. E., *et al.*, Power factor enhancement in solution-processed organic n-type thermoelectrics through molecular design. *Adv. Mater.* **2014,** *26* (21), 3473-3477.

26. Coates, N. E.; Yee, S. K.; McCulloch, B.; See, K. C.; Majumdar, A., *et al.*, Effect of interfacial properties on polymer–nanocrystal thermoelectric transport. *Adv. Mater.* **2013,** *25* (11), 1629-1633.

27. Yee, S. K.; Coates, N. E.; Majumdar, A.; Urban, J. J.; Segalman, R. A., Thermoelectric power factor optimization in PEDOT: PSS tellurium nanowire hybrid composites. *Phys. Chem. Chem. Phys.* **2013,** *15* (11), 4024-4032.

28. Venkatasubramanian, R.; Siivola, E.; Colpitts, T.; O'Quinn, B., Thin-film thermoelectric devices with high room-temperature figures of merit. *Nature* **2001,** *413* (6856), 597-602.

29. Hsu, K. F.; Loo, S.; Guo, F.; Chen, W.; Dyck, J. S., *et al.*, Cubic AgPbmSbTe2+m: Bulk thermoelectric materials with high figure of merit. *Science* **2004,** *303* (5659), 818-821.

30. Poudel, B.; Hao, Q.; Ma, Y.; Lan, Y.; Minnich, A., *et al.*, High-thermoelectric performance of nanostructured bismuth antimony telluride bulk alloys. *Science* **2008,** *320* (5876), 634-638.

31. Kunadian, I.; Andrews, R.; Menguc, M. P.; Qian, D., Thermoelectric power generation using doped MWCNTs. *Carbon* **2009,** *47* (3), 589-601.

32. Choi, K.; Yu, C., Highly doped carbon nanotubes with gold nanoparticles and their influence on electrical conductivity and thermopower of nanocomposites. *PLos One* **2012,** *7* (9), e44977.

33. Yu, C.; Ryu, Y.; Yin, L.; Yang, H., Modulating electronic transport properties of carbon nanotubes and improving the thermoelectric power factor via nanoparticle decoration. *ACS Nano* **2011,** *5*, 1297-1303.

34. Kaminishi, D.; Ozaki, H.; Ohno, Y.; Maehashi, K.; Inoue, K., *et al.*, Air-stable n-type carbon nanotube field-effect transistors with Si3N4 passivation films fabricated by catalytic chemical vapor deposition. *Appl. Phys. Lett.* **2005,** *86* (11).

35. Kim, S. M.; Jang, J. H.; Kim, K. K.; Park, H. K.; Bae, J. J., *et al.*, Reduction-controlled viologen in bisolvent as an environmentally stable n-type dopant for carbon nanotubes. *J. Am. Chem. Soc.* **2009,** *131* (13), 5010-5010.

36. Shim, M.; Javey, A.; Kam, N. W. S.; Dai, H. J., Polymer functionalization for air-stable n-type carbon nanotube field-effect transistors. *J. Am. Chem. Soc.* **2001,** *123* (46), 11512-11513.

37. Ryu, Y.; Freeman, D.; Yu, C., High electrical conductivity and n-type thermopower from double-/single-wall carbon nanotubes by manipulating charge interactions between nanotubes and organic/inorganic nanomaterials. *Carbon* **2011,** *49*, 4745-4751.

38. Freeman, D.; Choi, K.; Yu, C., N-type thermoelectric performance of functionalized carbon nanotube-filled polymer composites. *PLos One* **2012,** *7*, e47822.

39. Hewitt, C. A.; Kaiser, A. B.; Roth, S.; Craps, M.; Czerw, R., *et al.*, Multilayered carbon nanotube/polymer composite based thermoelectric fabrics. *Nano Lett.* **2012,** *12* (3), 1307-1310.

40. Chipman, J., The soret effect. *J. Am. Chem. Soc.* **1926,** *48* (10), 2577-2589.

41. Tanner, C. C., The soret effect. *Nature* **1952,** *170* (4314), 34-35.

42. Haase, R., *Thermodynamics of irreversible processes*. Dover Publications: Mineola, NY, 1968.

43. De Groot, S. R.; Mazur, P., *Non-equilibrium thermodynamics*. Dover Publications: Mineola, NY, 2013.

44. Platten, J. K., The Soret effect: A review of recent experimental results. *J. Appl. Mech.-Trans. ASME* **2006,** *73* (1), 5-15.

45. Wurger, A., Transport in charged colloids driven by thermoelectricity. *Phys. Rev. Lett.* **2008,** *101* (10).

46. Vigolo, D.; Buzzaccaro, S.; Piazza, R., Thermophoresis and thermoelectricity in surfactant solutions. *Langmuir* **2010,** *26* (11), 7792-7801.

47. Sehnem, A. L.; Neto, A. M. F.; Aquino, R.; Campos, A. F. C.; Tourinho, F. A., *et al.*, Temperature dependence of the Soret coefficient of ionic colloids. *Phys. Rev. E* **2015,** *92* (4).

48. Majee, A.; Wurger, A., Collective thermoelectrophoresis of charged colloids. *Phys. Rev. E* **2011,** *83* (6).

49. Majee, A.; Wurger, A., Charging of heated colloidal particles using the electrolyte seebeck effect. *Phys. Rev. Lett.* **2012,** *108* (11).

50. Guthrie, G.; Wilson, J. N.; Schomaker, V., Theory of the thermal diffusion of electrolytes in a clusius column. *J. Chem. Phys.* **1949,** *17* (3), 310-313.

51. Agar, J. N.; Mou, C. Y.; Lin, J. L., Single-ion heat of transport in electrolyte-solutions - a hydrodynamic theory. *J. Phys. Chem.* **1989,** *93* (5), 2079-2082.

52. Sokolov, V. N.; Safonova, L. P.; Pribochenko, A. A., The thermal diffusion of hydrogen chloride in water-monoatomic alcohol mixtures at 298 K. *J. Solut. Chem.* **2006,** *35* (12), 1621-1630.

53. Leaist, D. G.; Hao, L., Very large thermal separations for polyelectrolytes in salt-solutions. *J. Chem. Soc.-Faraday Trans.* **1994,** *90* (13), 1909-1911.

54. Ail, U.; Jafair, M. J.; Wang, H.; Ederth, T.; Berggren, M., *et al.*, Thermoelectric properties of polymeric mixed conductors. *Adv. Funct. Mater.* **2016,** *26*, 6288-6296.

55. Wang, H.; Yin, L.; Pu, X.; Yu, C., Facile charge carrier adjustment for improving thermopower of doped polyaniline. *Polymer* **2013,** *54* (3), 1136-1140.

56. Kim, Y. S.; Kim, D.; Martin, K. J.; Yu, C.; Grunlan, J. C., Influence of stabilizer concentration on transport behavior and thermopower of carbon nanotube filled latex-based composites. *Macromol. Mater. Eng.* **2010,** *295*, 431-436.

57. Yu, C.; Shi, L.; Yao, Z.; Li, D.; Majumdar, A., Thermal conductance and thermopower of an individual single-wall carbon nanotube. *Nano Lett.* **2005,** *5* (9), 1842-1846.

58. Collins, P. G.; Bradley, K.; Ishigami, M.; Zettl, A., Extreme oxygen sensitivity of electronic properties of carbon nanotubes. *Science* **2000,** *287* (5459), 1801-1804.

59. Ryu, Y.; Yin, L.; Yu, C., Dramatic electrical conductivity improvement of carbon nanotube networks by simultaneous de-bundling and hole-doping with chlorosulfonic acid. *J. Mater. Chem.* **2012,** *22* (14), 6959-6964.

60. Valentini, L.; Armentano, I.; Puglia, D.; Kenny, J. M., Dynamics of amine functionalized nanotubes/epoxy composites by dielectric relaxation spectroscopy. *Carbon* **2004,** *42* (2), 323-329.

61. Kim, S. L.; Choi, K.; Tazebay, A.; Yu, C., Flexible power fabrics made of carbon nanotubes for harvesting thermoelectricity. *ACS Nano* **2014,** *8*, 2377-2386.

62. Vukovic, G. D.; Marinkovic, A. D.; Skapin, S. D.; Ristic, M. D.; Aleksic, R., *et al.*, Removal of lead from water by amino modified multi-walled carbon nanotubes. *Chem. Eng. J.* **2011,** *173* (3), 855-865.

63. Huang, Y. P.; Lin, I. J.; Chen, C. C.; Hsu, Y. C.; Chang, C. C., *et al.*, Delivery of small interfering RNAs in human cervical cancer cells by polyethylenimine-functionalized carbon nanotubes. *Nanoscale Res. Lett.* **2013,** *8*.

64. Smith, B. C., *Infrared Spectral Interpretation: A Systematic Approach*. 1st ed.; CRC Press: Boca Raton, FL, 1998.

65. Basiuk, E. V.; Basiuk, V. A.; Banuelos, J. G.; Saniger-Blesa, J. M.; Pokrovskiy, V. A., *et al.*, Interaction of oxidized single-walled carbon nanotubes with vaporous aliphatic amines. *J. Phys. Chem. B* **2002,** *106* (7), 1588-1597.

66. Misra, A.; Tyagi, P. K.; Singh, M. K.; Misra, D. S., FTIR studies of nitrogen doped carbon nanotubes. *Diam. Relat. Mat.* **2006,** *15* (2-3), 385-388.

67. Gritzner, G.; Kuta, J., Recommendations on reporting electrode-potentials in nonaqueous solvents (recommendations 1983). *Pure Appl. Chem.* **1984,** *56* (4), 461-466.

68. Bredas, J. L.; Silbey, R.; Boudreaux, D. S.; Chance, R. R., Chain-length dependence of electronic and electrochemical properties of conjugated systems - polyacetylene, polyphenylene, polythiophene, and polypyrrole. *J. Am. Chem. Soc.* **1983,** *105* (22), 6555-6559.

69. Vukovic, G.; Marinkovic, A.; Obradovic, M.; Radmilovic, V.; Colic, M., *et al.*, Synthesis, characterization and cytotoxicity of surface amino-functionalized water-dispersible multi-walled carbon nanotubes. *Appl. Surf. Sci.* **2009,** *255* (18), 8067-8075.

70. Kataura, H.; Kumazawa, Y.; Maniwa, Y.; Umezu, I.; Suzuki, S., *et al.*, Optical properties of single-wall carbon nanotubes. *Synth. Met.* **1999,** *103* (1-3), 2555-2558.

71. Li, X. M.; Zhu, H. W.; Wei, J. Q.; Wang, K. L.; Xu, E. Y., *et al.*, Determination of band gaps of self-assembled carbon nanotube films using Tauc/Davis-Mott model. *Appl. Phys. A-Mater. Sci. Process.* **2009,** *97* (2), 341-344.

72. Gao, R. P.; Pan, Z. W.; Wang, Z. L., Work function at the tips of multiwalled carbon nanotubes. *Appl. Phys. Lett.* **2001,** *78* (12), 1757-1759.

73. Eastman, D. E., Photoelectric work functions of transition, rare-earth, and noble metals. *Phys. Rev. B* **1970,** *2* (1), 1-2.

74. Lee, S. H.; Lin, W. C.; Chang, C. J.; Huang, C. C.; Liu, C. P., *et al.*, Effect of the chemical composition on the work function of gold substrates modified by binary self-assembled monolayers. *Phys. Chem. Chem. Phys.* **2011,** *13* (10), 4335-4339.

75. Van der Pauw, L. J., A method of measuring the resistivity and hall coefficient on lamellae of arbitrary shape. *Philips Tech. Rev.* **1958,** *20*, 220-224.

76. Test Methods for Measuring Resistivity and Hall Coefficient and Determining Hall Mobility in Single-Crystal Semiconductors. *ASTM Designation F76, Annual Book of ASTM Standards* **2011,** *10.04*.

77. Durkop, T.; Getty, S. A.; Cobas, E.; Fuhrer, M. S., Extraordinary mobility in semiconducting carbon nanotubes. *Nano Lett.* **2004,** *4* (1), 35-39.

78. Teflon PTFE properties handbook. Dupont: 2012. https://www.chemours.com/.

79. Incropera, F. P.; Dewitt, D. P., *Fundamentals of heat and mass transfer*. 5th ed.; John Wiley & Sons: Hoboken, NJ, 2001.

80. Chee, Y. H.; Niknejad, A. M.; Rabaey, J. M., An ultra-low-power injection locked transmitter for wireless sensor networks. *IEEE J. Solid-State Circuit* **2006,** *41* (8), 1740-1748.

81. Liu, H.; Crooks, R. M., Paper-based electrochemical sensing platform with integral battery and electrochromic read-out. *Anal. Chem.* **2012,** *84* (5), 2528-2532.

82. Tyrrell, H. J. V.; Colledge, R., Thermal diffusion potentials and the soret effect. *Nature* **1954,** *173* (4397), 264-265.

83. Chang, W. B.; Fang, H. Y.; Liu, J.; Evans, C. M.; Russ, B., *et al.*, Electrochemical effects in thermoelectric polymers. *ACS Macro Lett.* **2016,** *5* (4), 455-459.

84. Xing, Z. Y.; Wang, B.; Gao, W. Y.; Pan, C. Q.; Halsted, J. K., *et al.*, Reducing CO_2 to dense nanoporous graphene by Mg/Zn for high power electrochemical capacitors. *Nano Energy* **2015,** *11*, 600-610.

85. Benson, J.; Kovalenko, I.; Boukhalfa, S.; Lashmore, D.; Sanghadasa, M., *et al.*, Multifunctional CNT-polymer composites for ultra-tough structural supercapacitors and desalination devices. *Adv. Mater.* **2013,** *25* (45), 6625-6632.

86. Kim, S. L.; Lin, H. T.; Yu, C., Thermally chargeable solid-state supercapacitor. *Adv. Energy Mater.* **2016,** *6* (18).

87. Forney, C. F.; Brandl, D. G., Control of humidity in small controlled-environment chambers using glycerol-water solutions. *HortTechnology* **1992,** *2* (1), 52-54.

88. Yu, H. W.; Kim, H. K.; Kim, T.; Bae, K. M.; Seo, S. M., *et al.*, Self-powered humidity sensor based on graphene oxide composite film intercalated by poly(sodium 4-styrenesulfonate). *ACS Appl. Mater. Interfaces* **2014,** *6* (11), 8320-8326.

89. Bard, A. J.; Faulkner, L. R., *Electrochemical Methods: Fundamentals and Applications*. 2nd ed.; John Wiley: Hoboken, NJ, 2001.

90. Shao, L.; Jeon, J. W.; Lutkenhaus, J. L., Porous polyaniline nanofiber/vanadium pentoxide layer-by-layer electrodes for energy storage. *J. Mater. Chem. A* **2013,** *1* (26), 7648-7656.

91. Smela, E.; Lu, W.; Mattes, B. R., Polyaniline actuators - Part 1. PANI(AMPS) in HCl. *Synth. Met.* **2005,** *151* (1), 25-42.

92. Ding, J. F.; Chuy, C.; Holdcroft, S., A self-organized network of nanochannels enhances ion conductivity through polymer films. *Chem. Mat.* **2001,** *13* (7), 2231-2233.

93. Ma, G. F.; Dong, M. M.; Sun, K. J.; Feng, E. K.; Peng, H., *et al.*, A redox mediator doped gel polymer as an electrolyte and separator for a high performance solid state supercapacitor. *J. Mater. Chem. A* **2015,** *3* (7), 4035-4041.

94. Gao, H.; Lian, K., Proton-conducting polymer electrolytes and their applications in solid supercapacitors: a review. *RSC Adv.* **2014,** *4* (62), 33091-33113.

95. Khandelwal, M.; Mench, M. M., Direct measurement of through-plane thermal conductivity and contact resistance in fuel cell materials. *J. Power Sources* **2006,** *161* (2), 1106-1115.

96. Burheim, O.; Vie, P. J. S.; Pharoah, J. G.; Kjelstrup, S., Ex situ measurements of through-plane thermal conductivities in a polymer electrolyte fuel cell. *J. Power Sources* **2010,** *195* (1), 249-256.

97. Yuan, L. Y.; Xiao, X.; Ding, T. P.; Zhong, J. W.; Zhang, X. H., *et al.*, Paper-based supercapacitors for self-powered nanosystems. *Angew. Chem.-Int. Edit.* **2012,** *51* (20), 4934-4938.

98. Anothumakkool, B.; Soni, R.; Bhange, S. N.; Kurungot, S., Novel scalable synthesis of highly conducting and robust PEDOT paper for a high performance flexible solid supercapacitor. *Energ. Environ. Sci.* **2015,** *8* (4), 1339-1347.

99. Yao, B.; Yuan, L. Y.; Xiao, X.; Zhang, J.; Qi, Y. Y., *et al.*, Paper-based solid-state supercapacitors with pencil-drawing graphite/polyaniline networks hybrid electrodes. *Nano Energy* **2013,** *2* (6), 1071-1078.

100. Wang, L.; Feng, X.; Ren, L. T.; Piao, Q. H.; Zhong, J. Q., *et al.*, Flexible solid-state supercapacitor based on a metal-organic framework interwoven by electrochemically-deposited PANI. *J. Am. Chem. Soc.* **2015,** *137* (15), 4920-4923.

101. Zhang, K.; Hu, H. B.; Yao, W. T.; Ye, C. H., Flexible and all-solid-state supercapacitors with long-time stability constructed on PET/Au/polyaniline hybrid electrodes. *J. Mater. Chem. A* **2015,** *3* (2), 617-623.

102. Hu, L. B.; Choi, J. W.; Yang, Y.; Jeong, S.; La Mantia, F., *et al.*, Highly conductive paper for energy-storage devices. *Proc. Natl. Acad. Sci. U. S. A.* **2009,** *106* (51), 21490-21494.

103. Simon, P.; Gogotsi, Y., Materials for electrochemical capacitors. *Nat. Mater.* **2008,** *7* (11), 845-854.

104. Khosrozadeh, A.; Xing, M.; Wang, Q., A high-capacitance solid-state supercapacitor based on free-standing film of polyaniline and carbon particles. *Appl. Energy* **2015,** *153*, 87-93.

105. Liu, Q.; Nayfeh, O.; Nayfeh, M. H.; Yau, S. T., Flexible supercapacitor sheets based on hybrid nanocomposite materials. *Nano Energy* **2013,** *2* (1), 133-137.

106. Kang, Y. J.; Chung, H.; Han, C. H.; Kim, W., All-solid-state flexible supercapacitors based on papers coated with carbon nanotubes and ionic-liquid-based gel electrolytes. *Nanotechnology* **2012,** *23* (6).

107. Liu, Y. Q.; Weng, B.; Razal, J. M.; Xu, Q.; Zhao, C., *et al.*, High-performance flexible all-solid-state supercapacitor from large free-standing graphene-PEDOT/PSS films. *Sci. Rep.* **2015,** *5*.

108. *ANSI/ASHRAE standard 55-2010 thermal environmental conditions for human occupancy*. ASHRAE: Atlanta, GA, 2010.

109. Cengel, Y. A.; Ghajar, A. J., *Heat and Mass Transfer: Fundamentals and Applications*. 5th ed.; McGraw-Hill Education: New York, NY, 2014; p 992.

110. Yang, Y.; Lee, S. W.; Ghasemi, H.; Loomis, J.; Li, X. B., *et al.*, Charging-free electrochemical system for harvesting low-grade thermal energy. *Proc. Natl. Acad. Sci. U. S. A.* **2014,** *111* (48), 17011-17016.

111. Yee, R. S. L.; Zhang, K.; Ladewig, B. P., The effects of sulfonated poly(ether ether ketone) ion exchange preparation conditions on membrane properties. *Membranes* **2013,** *3* (3), 182-95.

112. Li, Z. H.; Dai, W. J.; Yu, L. H.; Xi, J. Y.; Qiu, X. P., *et al.*, Sulfonated poly(ether ether ketone)/mesoporous silica hybrid membrane for high performance vanadium redox flow battery. *J. Power Sources* **2014,** *257*, 221-229.